

***High power laser development in the UV for accelerators
and light sources***

PhD dissertation

Author:

Márta Divall 'Csatári'

Supervisor:

Dr. Károly Osvay

Consultant:

Dr. Ian N. Ross



University of Szeged

Optics and Quantumelectronics Department

2012

Table of Contents

I.	Introduction	4
II.	Scientific background and aims	9
II.1	Photo-injectors	9
II.1.1	Photo-injector basics	10
II.1.2	Photo-cathodes	11
II.1.3	CERN Compact Linear Collider, Test Facility 2 and 3	14
II.2	Ultrashort laser pulses	21
II.2.1	Generation of ultrashort laser pulses	21
II.2.2	Amplification of ultrashort laser pulses	27
II.3	Photo-injector lasers	37
II.3.1	Existing laser systems	38
II.3.2	Available gain materials	39
II.3.3	Stability and reliability	44
II.4	Generation of UV and losses	49
II.4.1	Non-linear processes	49
II.4.2	Measurement techniques for two photon absorption	56
II.4.3	Available non-linear materials and their properties	56
II.5	Pulse structure, satellites and contrast	57
II.5.1	Single pulse measurement techniques	58
II.5.2	Pulse train measurement techniques	60
II.5.3	Optical elements affecting contrast	62
II.5.4	Contrast during amplification and conversion	64
III.	New scientific results	65
III.1	Amplifier development for CERN CLIC photo-injectors	65
III.1.1	Amplifier pump chamber design	66
III.1.2	The laser setup	68
III.1.3	The model	71
III.1.4	Experimental results and comparison with the model	75
III.1.5	Conclusion	83
III.2	Correlation measurements of the laser and electron beams	83
III.2.1	Electron beam diagnostics	83
III.2.2	Transport line and virtual cathode	84
III.2.3	Pointing stability measurements	85
III.2.4	Amplitude stability measurements	87
III.2.5	Conclusion	89
III.3	Two-photon absorption measurement of non-linear crystals	89
III.3.1	Experimental setup	90
III.3.2	Measurement results	90
III.3.3	Conclusion	93
III.4	Phase-coding development for photo-injector laser system	93
III.4.1	Design considerations and the final setup	93
III.4.2	Amplitude and timing accuracy	95
III.4.3	Integration into the laser system	97
III.4.4	Electron beam diagnostics	100
III.4.5	Phase coding measurements	100
III.4.6	Conclusion	105
III.5	Temporal contrast of high intensity UV pulses	105
III.5.1	Modelling results	106
III.5.2	Measurements	110
III.5.3	Conclusion	113
IV.	Summary	114

TABLE OF ABBREVIATIONS

ASE	Amplified Spontaneous Emission
BWL	Bandwidth Limited
CLIC	Compact Linear Collider
CPA	Chirped Pulse Amplification
CTF2	CLIC Test Facility 2
CTF3	CLIC Test Facility 3
FEL	Free Electron Laser
KML	Kerr-lens Mode-Locking
ML	Mode-locking
OPA	Optical Parametric Amplifier
OPCPA	Optical Parametric Chirped Pulse Amplification
PI	Photo-injector
PILOT	Photo-injector Long Train laser
PM	Phase-matching
RF	Radio Frequency
SESAM	Semiconductor Saturable Absorber Mode-locker

I. INTRODUCTION

General aim and historical background

Application driven laser development is aiming for coherence, directionality, brightness or monochromaticity, wavelength tuneability and stability depending on the specific requirements. In general high focal intensities with reproducible high beam quality, both temporally and spatially are required. There are jumps in intensity which take us to different levels of understanding of the world around us. If we take the Hydrogen-atom as an example and estimate how much energy is more than just a disturbance for an atomic system. The electrostatic (Coulomb) field of the atom is $\approx 3 \cdot 10^{16} \text{ W/cm}^2$. As long as the intensity of the incident light is smaller than that, we can use the perturbation-theory. Further borders are 10^{18} W/cm^2 when the oscillation energy of the electron is comparable with the steady state energy, and relativistic effects are coming into the calculations. The next is at 10^{29} W/cm^2 , the intensity-region for “vacuum-nonlinearity”.

To generate high intensities one could increase the energy, increase the focusability or shorten the pulse duration. The limits for those last two are the diffraction and the uncertainty relation. To get short pulses a broad bandwidth needs to be generated. Diffraction limit is pushing the frontiers to shorter wavelengths.

Together with the laser development aiming to reach these limits, free electron lasers (FEL), based on electrons in accelerators and undulators are making their way to shorter wavelengths and higher coherence. Currently for the 1keV photon energy range they are the only candidate to generate high power coherent radiation. However, this requires short electron bunches with extremely high quality to be produced, with ultralow emittance, where lasers take their place by providing the electron source together with a photo-cathode and an RF-gun^{1,1}. Photo-injector (PI) allows approximately two orders of magnitude higher brightness than a conventional injector and is also used for high-energy linear colliders, such as the Compact Linear Collider (CLIC).

Laser systems are now an essential part of an accelerator/ FEL facility not just by providing the primary electron source, but also seeding the FEL with higher harmonics of the laser for achieving better FEL lasing, delivering photons for pump-probe experiments and characterization of the electron bunches. The Linac Coherent Light Source (LCLS) at SLAC National Laboratory generates, as of 2010, the shortest wavelengths at 0.15nm in 80fs long X-ray pulses. European X-FEL at DESY Hamburg and SwissFEL at Paul Scherrer Institute in Switzerland are both aiming to reach 0.1nm wavelengths with up to $5 \cdot 10^{33}$ peak brilliance (meaning number of photons /s mm² mrad² 0.1% bandwidth).

During the history of laser development generation of short pulses was the first step to reach high intensities. Short pulses have been achieved since the mode-locking technique was invented in the mid-1960s^{1,2}. Together with Q-switching techniques^{1,3} high intensities could be reached, opening up the possibility for non-linear optics. The first femtosecond laser was based on dye, but the narrow tunable range and the unreliability of these type of lasers lead back to the development of new solid

state materials, such as alexandrite ($\text{Cr:BeAl}_2\text{O}_2$)^{1.4} and Ti:sapphire ($\text{Ti:Al}_2\text{O}_3$)^{1.4}. Later, using prisms to compensate for group velocity dispersion in the oscillator cavity allowed pulses as short as 27 fs to be created^{1.6}. In the past 40 years many other novel mode-locking techniques were introduced, such as acousto-optic modulation^{1.8}, additive pulse mode-locking, and other passive techniques self-mode-locking, such as Kerr-lens mode-locking (KLM)^{1.9,1.10} and more recently SESAM (Semiconductor Saturable Absorber Mode-locking), which is replacing the previously used organic dye saturable absorber and is applied to generate ultrashort pulses. KLM enabled the generation of 6.5 fs pulses^{1.11}. With nonlinear broad bandwidth generation and recompression 4.5 fs pulselengths can be reached.^{1.12,1.13}

The easiest way to scale up the energy of a laser is to build a chain of amplifiers. Two routes can be followed here, one is to generate high power at longer wavelengths, and convert to UV (multicolour lasers); the other is to generate low intensity UV pulses and amplify them directly. To amplify UV pulses in a conventional laser system one is limited by the fact, that we have to have a ν^3 time's bigger field for pumping (ν being the generated laser frequency) and we have to extract energy in $1/\nu^3$ times shorter time to provide the same ratio between spontaneous and stimulated emission. However, as for efficient extraction of the energy stored in the amplified media, we also need to be working close to the saturation fluence of the given gain material, which in the case of solid state materials is much higher. This leads to the need of strong focusing; which together with the short pulse leads to unwanted non-linear effects and eventually damage. Due to this, the generation of short pulses with high intensities was restricted to excimer and dye lasers until 1985, when Chirped Pulse Amplification (CPA)^{1.14-1.15} was developed and made it possible to generate ultrahigh power levels in solid-state laser materials. As the laser pulse is stretched (chirped) before the amplification utilizing dispersion in the material, the longer low intensity pulses can be safely amplified, still providing the necessary fluence for efficiency extraction. The pulses are then compressed back to their original transform limited duration. There are two main approaches in infrared laser pulse amplification using CPA technique. The first is power amplifier, where the active material is pumped directly by a light source, typically flashlamps, laser diodes or another laser source. The other approach is to amplify the IR pulses in a nonlinear optical material using a parametric process to transfer the pump light of a laser working at a shorter wavelength into the signal beam. This is the so-called Optical Parametric Amplifier (OPA). Here the advantage of longer chirped pulses is two-fold. One is to avoid damage and unwanted non-linear effects and the other is to efficiently match and overlap with the length of the pump pulse, as energy transfer is instantaneous in this case between the two. Optical parametric amplifiers can cover a wide range of wavelengths from 300nm-4 μm . Most of the commercially available tunable wavelength sources are based on parametric oscillators or amplifiers.

Laser systems based on this technology developed at several institutes are now available commercially and can generate 20 fs pulses with 1J of energy and provide a focused intensity around 10^{20} W/cm², well exceeding the barrier for relativistic optics at 10^{18} W/cm² and giving the onset of nonlinear effect and ionization. These pulses can be interacted with nonlinear or gaseous materials to extend their wavelength range from XUV to THz radiation. High Order Harmonics down to XUV regime

and with pulse durations inherently shorter than the drive pulse can be created, which opens up new application fields of the attosecond science^{1,16}. As the focussed intensity is so great, even the unwanted background radiation is intense enough to cause unwanted Coulomb-explosion, thus knowledge of the pulse-shape and the sources of pre-and post-pulses and pedestals are important for contrast improvement and for the success of experiments in this regime.

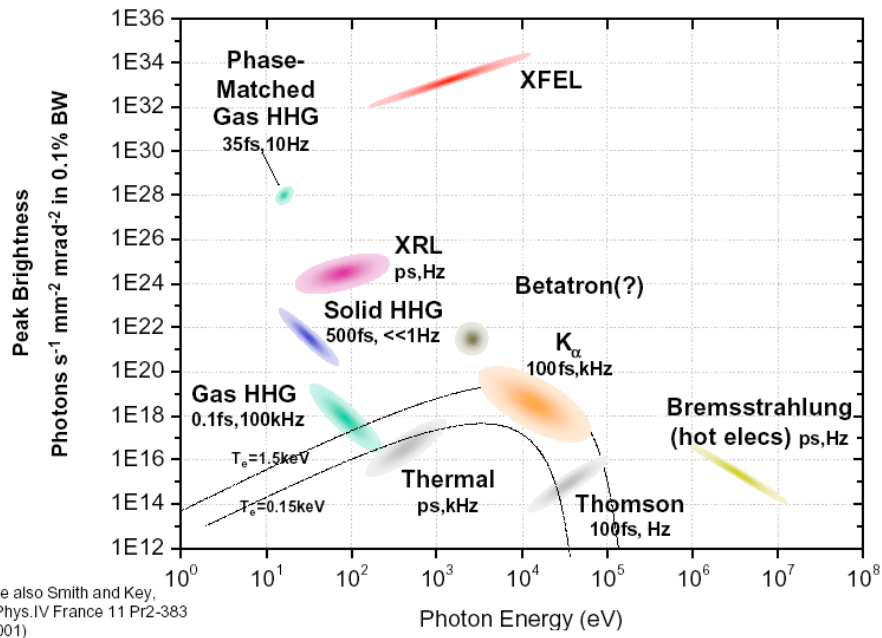


Fig. 1.1. Brightness from different sources as function of photon energy, showing the superiority of X-FEL's in the 1keV range and how lasers through High Harmonic Generation are still in the ring to deliver the brightest beams.

In the above mentioned multi-colour laser systems the IR amplified pulses are converted to UV through nonlinear conversion in crystals. At high intensities this process can be seriously limited by multi-photon absorption. In 1929, Maria Goeppert Mayer was the first to predict the possibility of two photons being absorbed in an atom in the same time^{1,16}. This was soon after Einstein's discovery of the photoelectric effect, and it suggested that states which are unreachable by one photon are allowed in the case of simultaneous absorption of two photons. However this effect only could be observed with a bright source, which only became available after the construction of the first laser. Because of the fairly low intensities available that time, scientists were more excited about the fact that this way they can make transitions between states, which are not connected by electric-dipole reactions, and can achieve coherent excitation to UV range, making visible radiation useful. In 1961 Kaiser and Garrett published the first paper experimentally showing generation of UV light from two photons of their 694 nm red maser light.^{1,18} With the development of high intensity lasers nonlinear absorption was found to limit the intensities passing through the window materials and optics.^{1,19, 1.20, 1.21}

Using nonlinear optical crystals the shortest possible wavelength achievable to date is 166 nm^{1.22} At these short wavelengths both linear and nonlinear absorption will have a major role in losses and temperature detuning of the phase-matching angle^{1.23} and optical damage. This is why the average power of these solid-state UV lasers still cannot compete with excimer lasers. However, when ultrashort pulses are required, then the bandwidth and gain-narrowing of the excimer laser puts a limit

on the shortest achievable pulse length of $\sim 150\text{fs}$ ^{1,24}. Dye lasers provide about the same bandwidth^{1,25}. Available solid-state laser materials at this wavelength are still exhibiting low gain. Optical parametric amplification provides a good tool for broadband amplification down to 300nm^{1,26}. Two-photon absorption induced losses also can limit the achievable gain from these systems, as both the parametric process and the absorption vary quadratically with the laser intensity. The pump wavelength during this amplification process is at the 266nm range.

The work reported in chapter III.1 is specifically directed towards the design and implementation of laser systems meeting the requirements of CERN Compact Linear Collider (CLIC) Test Facility 2 and 3 (CTF2 and CTF3) drive beam photo-injector. The laser is part of the high brightness electron source by illuminating a photo-cathode under high RF field. Design studies and prototype building of a mode-locked, high repetition rate, high gain, high power diode pumped pulse-train laser system operating in the UV carried out at Rutherford Appleton Laboratory are reported. Experiences gathered are used then for the design of a larger laser system to meet the requirements of CTF3. Long, stable pulse trains with up to 2J of total energy are generated after amplification.

Chapter III.2. shows correlation measurements carried out between the laser and produced electron beam at CERN. Amplitude stability is one of the main parameters yet to be met. Possible stabilization schemes are also discussed in this chapter.

One of the main challenges in the generation of long high repetition rate trains in the UV is the absorption losses in the conventionally used harmonic generation crystals. Two-photon absorption losses played a key role in the degradation of the pulse-train generated with CLIC requirements. Two-photon absorption measurements performed for the first time on CLBO and other crystals are reported in **chapter III.3**. Measurements were carried out the Szeged excimer laser facility using the 248nm of the KrF system.

A fast, clean phase-switching system was required for CTF3 laser, ensuring any leakage satellites were below the 1% level to maintain efficiency and reduce radiation loss control on the future CLIC machine. **In chapter III.4.** the detailed design of this system, based on telecommunication fiber optic modulators is presented. Measurements carried out both on the electron and the laser beam to demonstrate stable, accurate and satellite free switching will be detailed here.

In high intensity laser-matter interactions pulse shape is one of the most important parameters, which needs to be fully characterised. In single pulse laser systems, pre- and post-pulses, pedestals caused by system elements and the amplification process can degrade the temporal contrast to an unacceptable level. In conventional CPA systems, when ultra-broadband pulses are generated, optical elements will limit the spectral acceptance and hence cause change in the temporal shape of the pulses. Amplified spontaneous emission, saturation and gain narrowing in high gain amplifiers will also affect temporal shape. **In chapter III.5. of this work** I calculate the effect of the residual nonlinear phase-distortions due to misalignment and spectral distortions due to bandwidth limit of the optics in a conventional OPCPA system. I estimate the effect of these on the temporal contrast of the ultrashort, high intensity pulses. I also show that by measuring the spectra, the temporal contrast can be calculated in a significantly higher dynamical range. This is an important fact, when we try to measure temporal shape of a UV pulse, as commercial temporal shape measurement

devices, such as autocorrelators have limited usability. The work also includes modelling of temporal contrast measurements with conventional second- and third order correlators. The last part of this chapter will give some calculations for pre/post pulses, and their effect on spectra and phase. Modelling results are compared with measurements taken on the TITANIA laser system at Rutherford Appleton Laboratory.

II. SCIENTIFIC BACKGROUND AND AIMS

II.1 Photo-injectors

Photo-injectors have taken a new role as electron sources for accelerators when high brightness pulsed electrons are in demand for high energy linear accelerators. Thermionic guns can no longer provide the specifically 'tailored' electron bunches required from the injector. As laser pulses can be shaped in space and time, electron bunch parameters at the exit of the gun can be carefully tuned to achieve low emittance¹, energy spread² and short synchronized electron bunches³. Photo-injectors are now the first choice for electron source linear colliders, linear accelerators with energy recovery, fourth generation light sources, free electron lasers, injectors for laser-driven plasma wake field accelerators, or low-energy electron LINACs for applied research; all bringing their own requirements for the electron source (see Table II.1.1.).

Table II.1.1.: The required parameters from the electron source for different applications. H:High, M:Medium, L

Type of machine	High charge ⁴	Low emittance	Short bunch	Some specific requirements for the laser
Linear colliders	H	M	L	Good stability (phase, amplitude) Synchronizability to RF
FEL	L	H	L	High average power UV or tuneable near-IR
RF sources	H		M	'Beer can shape'
Wakefield accelerators	H		M	Polarized with helicity control
New accelerator schemes	L	M	L	High peak power
Coherent radiation sources		L	H	
Radiochemistry	H		M	

¹ A beam of particles can be characterized the density of the particles in the six-dimensional phase space, where size and momentum are defined along each Cartesian axes. Reference II.1 shows, that in the case of a system of non-interacting particles **emittance** is preserved over time in ideal conditions. Hence it's importance in beam characterization. In practice the six-dimensional description is usually split into three two-dimensional subspaces, (x; px), (y; py), and (z; pz). The emittance is defined in terms of the area occupied by the beam in these two-dimensional spaces. If the area occupied by the beam in the (x; px) plane is Γ_x , then the normalized or invariant emittance is defined as $\epsilon_x^n \equiv \frac{\Gamma_x}{\pi m_0 c}$, where m_0 is the electron rest mass and c is the speed of light. A low emittance particle beam is a beam where the particles are confined to a small distance and have nearly the same momentum. In a linear collider keeping the emittance small means that the likelihood of particle interactions will be increased resulting in higher brightness. To obtain high peak power from an FEL, the electron beam emittance has to be low to ensure that the interaction takes place over longer length and the produced radiation is more coherent.

² **Energy spread** determines the energy distribution of the particles within an electron bunch. It is like the bandwidth of a laser pulse, and the aim is to reach a very 'narrow band' source. Unlike other sources, such as conventional thermionic injectors or damping rings, the energy of electrons produced in a photo-injector is correlated in time and spread only in a very narrow energy band (<5keV).

³ **Bunch** is the equivalent of the pulse in laser terminology and **bunch length** gives the information about the temporal distribution of the electrons. Often in accelerator physics this is given in units of length, rather than time.

⁴ **Charge** is equal to the total number of electrons produced in a bunch times their charge ($1.602 \cdot 10^{-19}$ Coulomb) and through the quantum efficiency of the cathode is also proportional to the number of photons, which it is produced by.

Photo-injector lasers serve the primary role of providing the electrons at a front end of an accelerator together with a high gradient electron gun. This requires the laser to have the correct photon energy and hence the right wavelength for photo-emission from a specific cathode material. Wavelengths can vary from UV to IR depending on the application and the cathode used and whether polarized electrons are necessary. The pulse repetition rate is primarily set by the RF used for acceleration and requirements can vary from 10Hz single shot machines to long train of GHz repetition trains. As Free Electron Lasers emerged in the XUV regime together with the fast progress in accelerator technology, lasers now need to provide extremely high quality electron beams^{11,2}. Wavelength tuneability, shapability in space and in time are desirable for tuning the electron bunch parameters to achieve high brightness. In the following sections an introduction is given to the photo-injector architecture, the typical cathodes and the injector specific to the CERN Compact Linear Collider (CLIC). The requirements for the CERN CTF2 and CTF3 photo-injector lasers are described and the superiority in comparison to thermionic injector is discussed.

II.1.1 Photo-injector basics

The schematic of a photo-injector is shown on Fig.II.1.1. It consists of a master oscillator generating radio frequency (RF) signal, to which both the high gradient RF cavity and the laser's seed oscillator are synchronised. The injector also includes a photo emitting surface, the photocathode, which is illuminated with a train of pulses in the UV (although cathodes operating at other wavelengths also exist). The RF cavity is shaped to reduce the effect of the space charge forces between the produced electrons and gives the initial acceleration of the electrons to a few MeV.

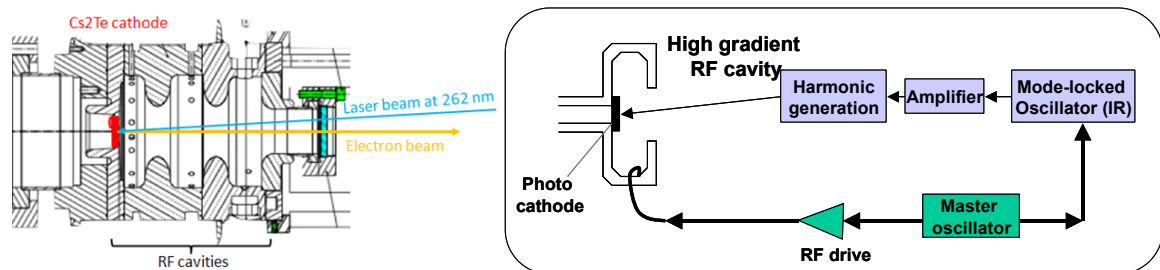


Fig.II.1.1: The components of a photo-injector are a laser, a photo cathode an RF source and an RF cavity (right)
Specific design for CTF3 PHIN injector (left)

The previously used thermionic guns required a very careful design of the gun in order to produce either good quality DC long pulses⁵, or short pulses, which need sub-harmonic bunchers to create short bunches by modulated fields. Pulsed systems are generally inefficient and result in satellites between the main bunches. Electrons produced through photo-emission however only have the 'imprint' of the laser pulse structure from which they are produced and hence allow for greater flexibility. Photo-injectors can deliver current densities at least four orders of magnitude greater than

⁵ In accelerators bunches are the short burst of electrons, while pulses are either produced in a gated fashion or are containing a train of bunches.

thermionic guns, up to 10^5 A/cm². By applying sufficient electric field to overcome space charge forces, brightnesses up to $5 \cdot 10^{15}$ Am⁻²rad⁻²/cm² have been demonstrated^{II.3.,II.4.,II.5.,II.6.,II.7.}.

The electron bandgap of the photo-cathode material will define the laser wavelength; the quantum efficiency of the cathode will determine the energy per pulse required from the laser; the vacuum conditions and sensitivity to the electric field will define the gun architecture, while the application will determine the average current and pulse structure, having a direct effect on the laser average power requirements and its architecture.

The main advantages of photo-injector versus thermionic gun are listed below:

- it replaces the thermionic gun and the bunching system by a single RF gun
- it produces high current densities and high brightness
- the pulse shaping is much easier, as it can be done directly on the laser
- can be adjusted in order to optimise the RF power generation
- small emittance is possible with laser pulse and beam shaping

However several issues related to using photo-emission process remain:

- UV power and pulse to pulse stability of the laser needs to be delivered
- Necessary average charge needs produced from the photo cathodes (in case of high average current injectors, such as the ones required for CLIC)
- Timing jitter to external reference RF, typically <0.5ps, but for FEL applications can be <0.1ps
- Pointing stability of the produced electron beam is directly dependent on the laser beam

II.1.2 Photo-cathodes

The photoemission process is well represented by the Three Steps model^{II.9.}. The photons are first absorbed by the cathode material, then the electrons are moved from the valence to the conduction band and finally the electron overcomes the surface barrier and exits the cathode.

Our ideal wish list for a photo-cathode would be high quantum efficiency, infrared or visible wavelength for injection, long lifetime even in moderate vacuum conditions. It also has to be easy to prepare and transport. However, meeting all these requirements in a single emitter is not possible. Metal cathodes provide low quantum efficiency and hence are used usually with high power single pulse laser systems, while alkaline semiconductor cathodes with higher quantum efficiency need less energy per pulse from the laser to produce the same charge and are suitable for pulse-train operation guns, such as the ones used at CERN or at DESY. GaAs cathodes are suitable to produce polarized electrons, but require careful helicity and wavelength tuneability of the laser around 800nm. These laser systems are based on Ti:Saph. A good summary of available cathodes and their uses can be found in ref. II.10.

Typical photo cathode parameters and possible limitations are listed below, in Table II.1.2. Sensitivity to the vacuum will have a big effect on lifetime of the cathode and in turn on the availability and reliability of the injector system. Other things to consider are:

- Time response to picosecond pulses will ultimately determine the pulse length required from the laser
- Bandgap of the cathode will determine the wavelength of the injection laser
- Quantum efficiency will set the energy/pulse requirement for the laser

Other limitations, which do not directly affect the laser requirements, also have to be taken into consideration:

- Dark current produced (when cathode is not illuminated), which affect beam quality
- Sensitivity to high field gradient
- Charge limit effect, maximum extractable charge/area
- Long operational lifetime, activation, reactivation, rejuvenation
- Ease and reproducibility of preparation

Table II.1.2. The most widely used photo cathodes and their advantages and disadvantages.

Photo cathode	Advantage	Disadvantage
Cs₃Sb, CsK₂Sb	<ul style="list-style-type: none"> ✓ High quantum efficiency ✓ 500 nm laser 	<ul style="list-style-type: none"> • Difficult to prepare • Short lifetime • Not sustain very high fields • Expensive preparation chamber • Expensive transport system • Need very good vacuum
Cs₂Te	<ul style="list-style-type: none"> ✓ High quantum efficiency ✓ Long lifetime ✓ Sustains high fields 	<ul style="list-style-type: none"> • Needs UV • Expensive preparation chamber • Expensive transport system • Questionable response to pulsetrain
Cu, Y, Mg	<ul style="list-style-type: none"> ✓ No preparation chamber needed ✓ Long lifetime (> 1 year) ✓ Fast response ✓ Sustain very high fields ✓ Sustain bad vacuum 	<ul style="list-style-type: none"> • Needs UV • Low quantum efficiency (Mg better 0.3%)
LaB₆, WcaOBaO	<ul style="list-style-type: none"> ✓ No preparation chamber needed ✓ Long lifetime 	<ul style="list-style-type: none"> • Needs UV • Low quantum efficiency • Need to be heated prior to operation

There is long history of high efficiency cathode development at CERN^{11,11}. Cs₂Te cathodes were chosen as the emitter for CLIC photo-injectors due to its capability to produce high charge, high working QE and relatively modest vacuum requirements. Cs₂Te cathodes fabricated at CERN with

coo-evaporation process can provide up to 20% starting efficiency and relatively long lifetime, when operated with wavelengths ~260nm. The full list of main parameters is listed below in Table II.1.3.

Table II.1.3. Basic parameters of Cs₆Te measured at CERN

Working wavelength	< 270 nm
Maximum QE	> 20 % @ 262 nm
Operating time with QE > 1.5 %	from weeks to months
Working pressure	< 10 ⁻⁹ mbar baked vacuum
Maximum electric field	> 127 MV/m
Relaxation time	< 2-3 ps
Dark current	quasi equivalent to copper
Peak current	>10 kA
Single pulse charge at least	100 nC in 10 ps
Mean current	> 1 mA (limited by laser)
Mean current density	21 mA/cm ²
Laser damage threshold	> 6W/cm ² @ 262 nm

The relationship between the produced charge and the laser parameters can be described by the following simple equation:

$$C[nC] = 8 \cdot \eta[\%] \cdot W[\mu J] \cdot \lambda[nm] \quad \text{II.1.)}$$

Where C is the produced charge in nC, η is the quantum efficiency⁶ of the cathode in %, W is the energy/micropulse in μJ and λ is the wavelength of the laser in nm (8 includes elementary charge, Plank constant and speed of light). This shows that if cathodes can be produced with similar quantum efficiencies to Cs₂Te, but working at the second harmonic wavelength of the laser, then potentially the laser parameters could be reduced by a factor of six. (a factor of three could be gained from conversion efficiency to UV, and a factor of two from the wavelength). This would also simplify detection and efficient propagation of the laser beam. Apart from reducing output power requirements on the laser, the stability of the system would be improved, by eliminating one nonlinear conversion stage from the laser. Cs₃Sb development is promising to move the operational wavelength to the visible. Vacuum sensitivity and hence lifetime of these cathodes are expected to be worse, than Cs₂Te, however limited testing time has not allowed further investigation of these cathodes to date.

Currently photoinjector cathodes and lasers are still falling behind the thermionic source in terms of stability and reliability.

⁶ **Quantum efficiency** equals to the number of electrons produced divided by the number of photons they are produced by.

II.1.3 CERN Compact Linear Collider, Test Facility 2 and 3

The Compact Linear Collider (CLIC)⁷ is a future lepton collider being designed to provide precision measurement of any new particles the Large Hadron Collider (LHC) may find, as well as opening up new energy frontiers, beyond the capabilities of existing particle accelerators^{II.12}

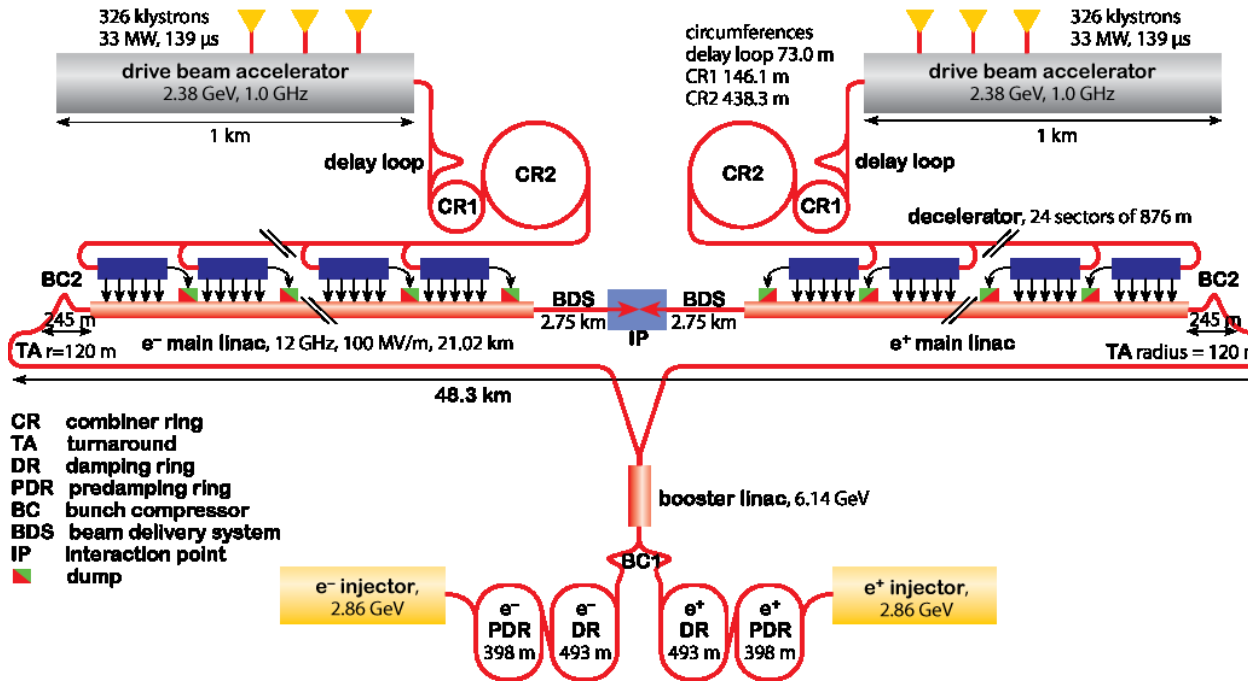


Fig.II.1.2. CLIC 3TeV design layout

The CLIC e-/e+ collider is based on the two-beam acceleration concept illustrated on Fig.II.1.2., where 24 sub-pulses of the 0.5GHz drive beam are interleaved through a delay loop and combiner ring to create high RF power, at 12GHz locally, by deceleration of the drive beam. This is used to power the accelerating structures for a second beam, the main beam.

Currently in CLIC Test Facility 3 (CTF3) the main beam, to be accelerated, is produced by a photo-injector. Since polarized electrons are a requirement they must be produced by a photo-injector and hence it was chosen as the base line option for the CLIC machine. Negative electron affinity GaAs cathodes, producing these electrons require a tuneable

Table II.1.4. CLIC drive beam injector parameters

Parameter	Nominal values	Unit
Beam energy	50	MeV
Pulse length	140.3/243.7	μs/ns
Beam current	4.2	A
Bunch charge	8.4	nC
Number of bunches	70128	
Total charge per bunch	590	mC
Bunch spacing	1.992	ns
Repetition rate	100	Hz
Emittance at 50MeV	100	mm mrad
Energy spread at 50MeV	1	%FWHM
Bunch length at 50MeV	4	mm (rms)
Charge variation shot to shot	0.1	%(rms)
Charge flatness flat top	0.1	%(rms)
Allowed satellite charge	<7	%
Allowed switching time	5	ns

⁷ Today, high energy physics experiments are focused on the tera electron volt (TeV) energy regions to explore the physics beyond the Standard Model such as supersymmetry, extra dimensions and new gauge bosons. LHC will extend this range up to 14 TeV. There are several collider concepts to provide complementary and precision measurement data to the LHC results. Compact Linear Collider (CLIC) at CERN is one of these besides the International Linear Collider (ILC) and Muon Collider (MC projects).

source ~800nm for high polarization purity. As these cathodes have long relaxation time (>10ns), with the repetition rate of the gun (4ns bunch separation) a mode-locked laser system would not provide any advantages. Therefore a Ti:Saph Q-switched system was developed at SLAC to deliver long bursts of laser light. More details can be found in CLIC Conceptual Design Report.^{II.13} Despite the fore mentioned disadvantages of the thermionic source, because of its demonstrated reliability it is the baseline option for the drive beam injector for CLIC. However the satellites produced by the sub-harmonic bunching system,- creating the short bunches out of the DC electron beam,- may yet prove to be a radiation issue for the future machine. As a result, the possibility of using a RF photo-injector as the drive-beam source was investigated. Injector parameters as of 2011 are shown in Table II.1.4.

As some of the parameters on the laser and cathode side require a feasibility study^{II.14,II.28}, development of the first laser system, PILOT, producing long trains of UV pulses for CTF2 was started in 2000.

II.1.3.1 Basic parameters and requirements for the drive beam injector laser

The laser system^{II.15} in 2001 at CERN was based on powerful flash-lamp pumped regenerative amplifiers and power amplifiers, a pulse multiplication technique to produce a train of up to 48 pulses and also included a stretcher and compressor. Scalability with this setup to longer trains was impractical. Since many thousands of pulses are required in the UV for the final CLIC machine all with identical parameters and a tight specification on mean power and average power it was necessary to build a more realistic system to test performance. The terminology is described below, with a typical scheme detailed in Fig. II.1.3.

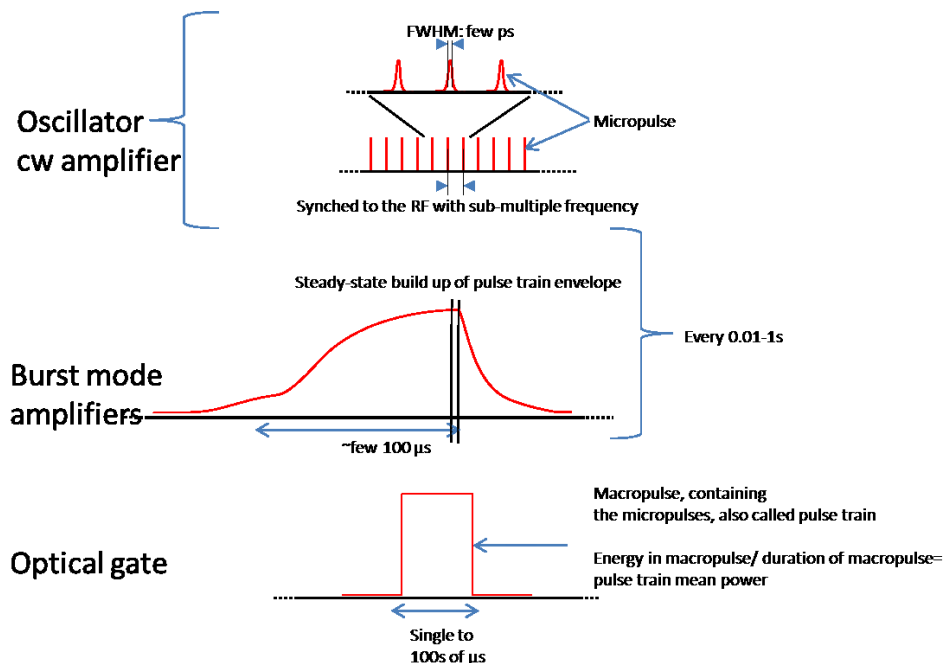


Fig.II.1.3. Typical pulse structure and definitions in a photo-injector laser system

- *Micropulses:* The individual ~10ps long pulses
- *Macropulse:* A flattop train of micropulses

- *Mean power*: Average power of the macropulse
- *Peak power*: Peak power of one micropulse
- *Duty cycle*: Length of macropulse / period macropulses
- *Average power*: Average power of the whole laser (mean power X duty cycle)

Specification and scaling towards the CLIC parameters are listed in Table II.1.5. Some terms unique to this type of laser systems had to be clarified and demonstrated in order to show the feasibility of a photo-injector for CLIC. Parameters which require attention for scalability or are particularly challenging, are marked in red. As one can see, the main challenges lies in the high repetition rate and hence high average power and the high gain, which needs to be constant to deliver long flat trains after conversion to UV.

Table II.1.5. CLIC drive beam laser requirements with a 2 step test phase included for demonstration and feasibility studies

	DRIVE beam			MAIN beam
	CTF2/PILOT	CTF3/PHIN	CLIC	CALIFES
charge/bunch (nC)	0.36	2.3	8.4	0.6
gate (ns)	1400	1200	140371	19.2
bunch spacing(ns)	4	0.666	1.992	0.666
bunch length (ps)	10	10	10	10
Rep. rate (GHz)	0.25	1.5	0.5	1.5
number of bunches	350	1802	70467	32
machine replate (Hz)	5	5	100	5
margin for the laser	N.A.	1.5	2.9	1.5
charge stability	<1%	<0.25%	<0.1%	<3%
QE(%)	4	3	2	0.3
laser wavelength (nm)	262	262	262	262
energy/micropulse on cathode (nJ)	60	363	1988	947
energy/micropulse laserroom (nJ)	120	544	5765	1420
energy/macrop. laserroom (uJ)	4.2E+01	9.8E+02	4.1E+05	4.1E+01
mean power (kW)	0.03	0.8	2.9	2.1
average power at cathode wavelength(W)	negligible	0.005	41	2.E-04
micro/macropulse stability	<1%	0.25%	<0.1%	<0.1%
conversion efficiency	5	0.1	0.1	0.15
energy/macropulse in IR (mJ)	0.8	9.8	4062.2	0.3
energy/micropulse in IR (uJ)	2.4	5.4	57.6	9.5
mean power in IR (kW)	0.6	8.2	28.9	14.2
average power on second harmonic (W)	0.04	0.49	406	1.E-03
average power in final amplifier (W)	1	9	608	15

The aim of the first PILOT laser was to show reliable production of a long pulse train. Stability was aimed at 1% pulse energy variation both for micro-and macropulse. Using the existing hardware, namely the available 250MHz oscillator seed it was possible to produce a 0.32nC/bunch, 1.4 μs pulse train of 350 pulses. The laser architecture had to be replaced by more reliable diode-pumped system.

The aim was also to understand the scalability of such Master Oscillator Power Amplifier (MOPA) systems to the higher power levels required for CTF3 and for the future CLIC machine. For the PILOT system the main aim was to efficiently pump and extract power from the amplifiers, to measure thermal properties of the chosen material, to compensate if necessary for thermal distortions in the beam and efficiently convert to the cathode wavelength. In addition to this the stability of the system had to be investigated so that the sources of noise could be understood and an active stabilization scheme planned for the future. Because of the special operating characteristics of the laser, the literature given isn't always fully applicable, so part of the work concentrated on to creating a code for the amplifier based on the conservation of energy, the basic rate equations and steady-state operation for pulse trains. The results of these calculations describe the performance well and can be used to optimise the system as well as for future designs for CTF3 and towards CLIC.

As high average power, long trains and very high gain were required with the final 1.5GHz seed repetition rate, the design, even for the less challenging PILOT system, had to include these requirements for future scalability. The **choice of the material and the laser architecture are described in II.4.2**, and the reliability and **stability issues in II.4.3**. The new scientific results of the work are detailed with the **construction and the test in III.1**.

1. **My aim was to build a diode-pumped MOPA (Master oscillator power amplifier) in multi-pass arrangement, test the steady-state properties of the system and generate 4th harmonic of the fundamental 1047 nm light provided by a mode-locked Nd:YLF oscillator. The laser system should satisfy the requirements for the CERN CTF2 injector and provide a 1.4 μs long train of <10 ps pulses with 5 Hz macropulse and 250 MHz micropulse repetition rate. In order to produce 0.15 nC of charge from the Cs₂Te photo cathode it must provide 30 nJ/micropulse energy at a wavelength below 270 nm. My aim was also to write a code/model to calculate the predicted behaviour of the multipass amplifier and then compare the data with the measurements.**
2. **My aim was to design a two stage amplifier system in multi-pass arrangement at 1047 nm, seeded by a mode-locked Nd:YLF oscillator, using the developed code. The laser system should satisfy the requirements for the CERN CTF3 experiment, to provide a 1.3 μs long train of <10 ps pulses with 50 Hz macropulse and 1.5 GHz micropulse repetition rate. In order to produce 2.3 nC of charge from the Cs₂Te photo cathode it must provide 370 nJ/micropulse energy at the 4th harmonic of the amplifier.**

II.1.3.2 Phase-coding

The long RF pulses with 12GHz repetition rate cannot be directly produced by any conventional RF source. Hence a high-current low energy beam is generated at the electron source and later the drive beam buckets are recombined in the so called CLIC drive beam recombination scheme. This being one of the most challenging tasks for CLIC test is carried out in CTF3 with multiplication factor of 8 and is detailed on Fig.II.1.4. Out of the 1.2 μs long train, 8 buckets or sub-

trains (140ns each) need to be repositioned longitudinally between each other shifted by 180 deg respect to the RF phase. The so called even buckets are kicked into the delay line, as they are in phase with the RF deflector, while the odd buckets go straight, as they are out of phase with the deflector. The delayline introduces a delay of half period. As a result, after the delay line there will be 1.2μs long train of bunches, but now with 3GHz repetition rate for 140ns and a gap for 140ns. These 4 of 3GHz sub-trains are now sent into the combiner ring, where they ‘wait for each other’ and with the correct delay applied recombine to 12GHz in a single 140ns long train. These bunches then all together are kicked out of the ring. The combiner rings increases the frequency further by a factor of 4 in case of CTF3 and an additional factor of 3 in case of CLIC.

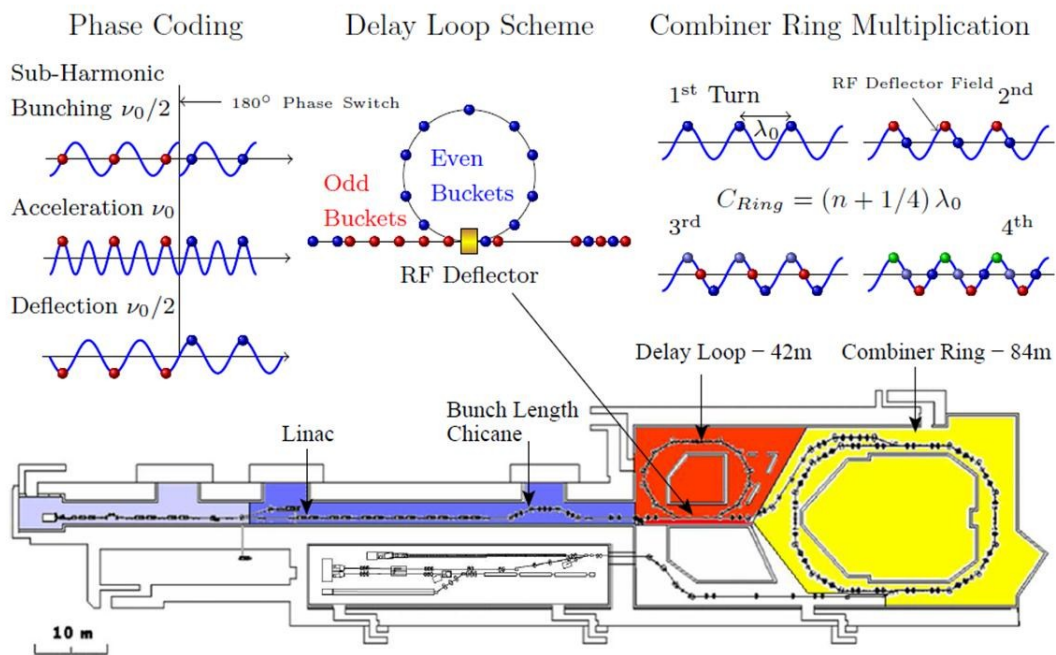


Fig.II.1.4. CTF3 Layout with the pulse multiplication scheme

For this to work the initial electron bunch train must be ‘phase coded’ i.e. some of the bunches must be delayed by half of an RF period with respect to the others. With the current thermionic gun this is achieved by sub-harmonic bunching, which is done over 8 consecutive pulses and causes considerable amount of unwanted satellites in the system^{11,16}. The transition performance of the 180° switch and the level of the satellites currently present in the system with the thermionic gun are shown in Fig II.1.5. These satellites at ~7% level could prove to be a serious radiation hazard for the future CLIC machine as they will propagate on a different path from main electron beam.

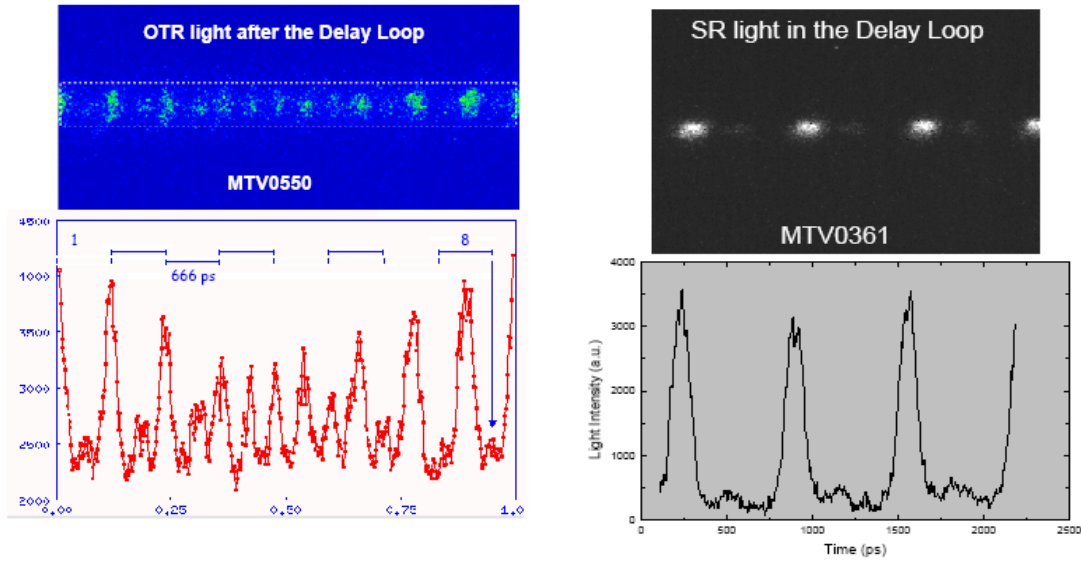


Fig.II.1.5.Switching performance in CTF3 with thermionic source and sub-harmonic bunchers measured during the switching period (left) and in one of the sub-trains (right)

However, with the laser based photo-injector the phase-coding can be done on the laser pulses before they are sent to the photocathode. The time structure produced by the laser directly correlates to the produced electron bunches. In CTF3 the source of the laser pulses is a 1.5 GHz mode-locked ps laser: The required coding system will delay (or not) so-called “even” and “odd” trains (laser) of bunches (electron), so called “sub pulses” (electron). The coding does not need to be continuous, it will be sufficient to apply the coding over periods of $>400 \mu\text{s}$ at up to 50 Hz repetition rate to match the amplification window of the amplifier chain. Each sub pulse will contain 212 laser pulses. The delay applied to the even sub pulses has to be 180 deg at 1.5 GHz i.e. 333 ps. The specifications for the phase-coding are summarized in Table. II.1.6. and the corresponding timing structure shown in Fig. II.1.6.

Table II.1.6. Input parameters for the phase-coding and the coding required below

Parameter	Value
Wavelength	1047 nm
Maximum average power	320 mW
Pulse length (Gaussian FWHM)	6 ps
Pulse repetition rate (cw mode-locked)	1.5 GHz
Time between pulses	~666 ps
Polarisation	Horizontal

Switching required for	>400 μs (at up to 50 Hz)
Length of sub-pulse	\sim 140.5 ns (212 pulses)
Switching frequency	\sim 7.1 MHz
Delay between generated sub-pulses	333 ps
Pulse timing stability	<0.2 ps
Amplitude stability	<0.1% rms
Total system loss	<9.6 dB
Number of subtrain to injector	8
Amplitude flatness rms	<0.1%
Time delay accuracy	<1ps

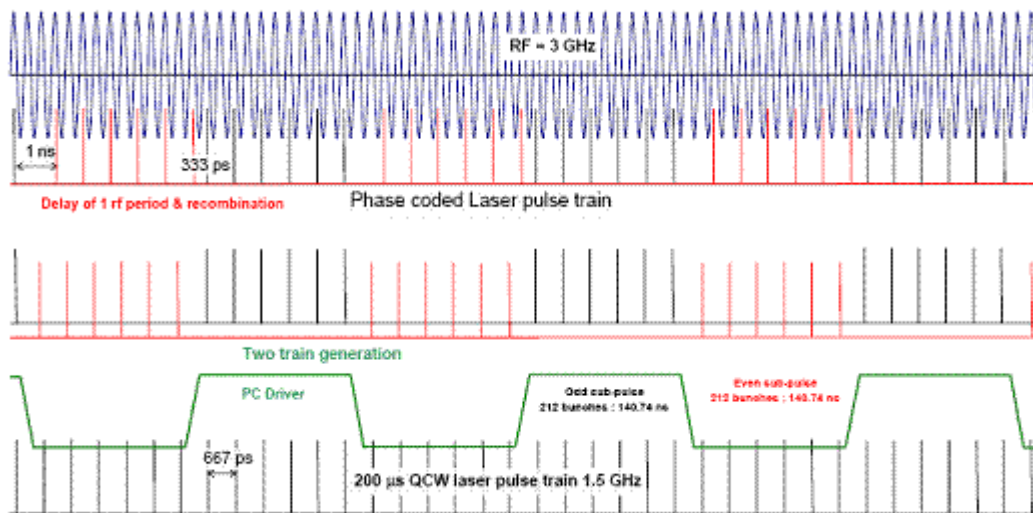


Fig.11.1.6. Phase-coding time structure requirement

The important performance parameters of the coding system include:

- **Switching time:** The system must allow complete switching from one sub-pulse to the next between two consecutive 1.5 GHz oscillator pulses i.e. within 666 ps. Together with the jitter of the switching electronics a rise time of <200 ps on the optical modulator or switch is required.
- **Stability:** There are very tight requirements on the pulse-to-pulse energy stability and the timing stability of the overall laser system. The coding system must not increase the timing jitter of the laser pulses by more than 0.2 ps rms. Any variations in the pulse energy must be minimized. They should be kept below 0.1% rms, although higher values than this may be acceptable as the laser system will include both passive and active amplitude stabilization.
- **Losses:** The coding system will be inserted between the existing oscillator and preamplifier. Any losses in the coding system will have to be made up in the preamplifier and subsequent power amplifiers. These losses should therefore be minimized.

- *Reliability*: The laser system, including the coding system needs to operate for long periods (days/weeks) with very high reliability.

3. **My aim was to design and implement phase-coding system, which provides switching rise-and fall-times below 200ps at 7.1 MHz with a phase-shift of 180deg at each switch respect to the 1.5 GHz, to integrate the phase-coding into CTF3 PHIN photo-injector laser system and to test the performance with electron beam.**

II.2 Ultrashort laser pulses

Short pulses in the few ps to fs range can be achieved by mode-locking. In solid-state lasers the pulse duration ranges from a few fs to 10's of ps and the repetition rate from 10MHz-100GHz. Oscillators are limited to <1μJ pulse energy due to the high intracavity power level and for most applications require further amplification. For the CLIC photo-injector application high mode-locked repetition rates are required. This limits the achievable single pulse energy (micropulse) to less than a Nano Joule. Since the energy per pulse in the UV needs to be delivered at the micro Joule level high gain amplification is necessary. In the following parts the basic description of the systems to generate and amplify laser pulses are described, it concentrates on those which are relevant to this work. A description of the laser pulses and pulse trains is also given.

I will not detail the rate equations and how population inversion is created in 3 and 4 level laser materials. References to these can be found in SPIE Field Guide to Lasers by R. Paschotta, or other more detailed books.^{II.17,II.18,II.19,II.20.}

II.2.1 Generation of ultrashort laser pulses

II.2.1.1 Mathematical description of laser pulses

In the time domain the simplest way to describe an optical pulse is by its power distribution $P(t)$, which is a function representing the duration of the pulse and diminishes in the rest of the time. Pulse length is given either as full width half maximum (FWHM) τ_p , where the power drops to half, or in sigma, meaning the rms of the distribution. Peak power of the pulse P_p is proportional to the energy of the pulse (E_p) and inversely proportional to the duration, including f_s form factor, which is characteristic to the pulse shape.

$$P_p = f_s \frac{E_p}{\tau_p} \quad \text{II.2)}$$

To understand where these measurable values come from we take the following detailed description based on Diels's book^{II.21.} on ultrashort laser phenomena. Using the fact, that in linear optics the real-valued electric field of the electro-magnetic wave can be described as a Fourier decomposition of monochromatic waves.

$$E(t) = \frac{1}{2\pi} \int_{-\infty}^{\infty} \tilde{E}(\omega) \cdot e^{i\omega t} d\omega \quad \text{II.3}$$

$$\tilde{E}(\omega) = \int_{-\infty}^{\infty} E(t) \cdot e^{-i\omega t} dt, \quad \text{II.4}$$

where $\tilde{E}(\omega)$ is the complex spectrum, the Fourier-transform of the time dependent electric field $E(t)$ not to be confused with E_p in eq.II.2., referring to energy of the pulse. $\Phi(\omega)$ is the spectral phase. Using complex description for $\tilde{E}(\omega)$ simplifies the analysis of $E(t)$.

Knowledge of the positive part of the spectrum is sufficient to describe the light field, as $E(t)$ is real and hence $\tilde{E}(\omega)$ is Hermetian.

$$\begin{aligned} \tilde{E}^+(\omega) &= 0 \text{ when } \omega < 0 \text{ and,} \\ \tilde{E}^+(\omega) &= \tilde{E}(\omega) \text{ when } \omega \geq 0 \end{aligned} \quad \text{II.5}$$

$$\begin{aligned} \tilde{E}^-(\omega) &= 0 \text{ when } \omega \geq 0 \text{ and,} \\ \tilde{E}^-(\omega) &= \tilde{E}(\omega) \text{ when } \omega < 0 \end{aligned} \quad \text{II.6}$$

As a result $\tilde{E}(\omega) = \tilde{E}^-(\omega) + \tilde{E}^+(\omega)$. Similarly $E(t)$ can also be split into two parts, $E^+(t)$ being the Fourier-decomposition of the positive part of the spectrum, while $E^-(t)$ of the negative part and both are complex-valued and can be expressed as a product of amplitude and phase:

$$E^+(t) = |E^+(t)| \exp(i\omega_0 t + i\varphi_a(t)) = \frac{1}{2} A(t) \exp(i\omega_0 t + i\varphi_a(t)) \quad \text{II.7}$$

Similarly for $\tilde{E}^+(\omega)$ with the absolute spectral intensity $I(\omega)$ and spectral phase $\Phi(\omega)$ can be introduced :

$$E^+(\omega) = |\tilde{E}^+(\omega)| \exp(-i\Phi(\omega)) = \sqrt{\frac{\pi}{\varepsilon_0 c n}} I(\omega) \exp(-i\Phi(\omega)) \quad \text{II.8}$$

For mathematical description both negative and positive parts are used, however in the laboratory only the positive and real parts are observed. Spectral intensity is related to the values measured by spectrometers and envelope function of $A(t)$ is related to pulse intensity. $\Phi(\omega)$ relates to how spectral components arrive in time, while $\varphi_a(t)$ tells us how frequency is changing in time.

The intensity function of the pulse can be given as:

$$I(t) = \frac{1}{2} \varepsilon_0 c n A(t)^2, \quad \text{II.9}$$

where ε_0 is vacuum permittivity, c is speed of light in vacuum and n is the refractive index of the material the pulse is travelling in.

There will be two typical pulse-shapes used for modelling in chapter III.5. One is Gaussian, which following the previous terminology can be described as:

$$E^+(t) = \frac{E_0}{2} e^{-2\ln 2 (t/\tau_0)^2}, \quad \text{II.10)}$$

$$\tilde{E}^+(\omega) = \frac{E_0 \cdot \tau_0}{2} \cdot \sqrt{\frac{\pi}{2\ln 2}} e^{-(\tau_0\omega)^2/8\ln 2}, \quad \text{II.11)}$$

where τ_0 is the FWHM of the corresponding intensity distribution. The other is Hyperbolic sechant (sech^2), and is described as:

$$E^+(t) = \frac{E_0}{2} \text{sech} \left[2\ln(1 + \sqrt{2}) t/\tau_0 \right], \quad \text{II.12)}$$

$$\tilde{E}^+(\omega) = \frac{E_0 \cdot \tau_0 \cdot \pi}{4\ln(1 + \sqrt{2})} \times \text{sech} \left(\frac{\omega \cdot \tau_0 \cdot \pi}{4\ln(1 + \sqrt{2})} \right), \quad \text{II.13)}$$

Distributions are shown in Fig.II.2.1 for 50fs FWHM long pulses.

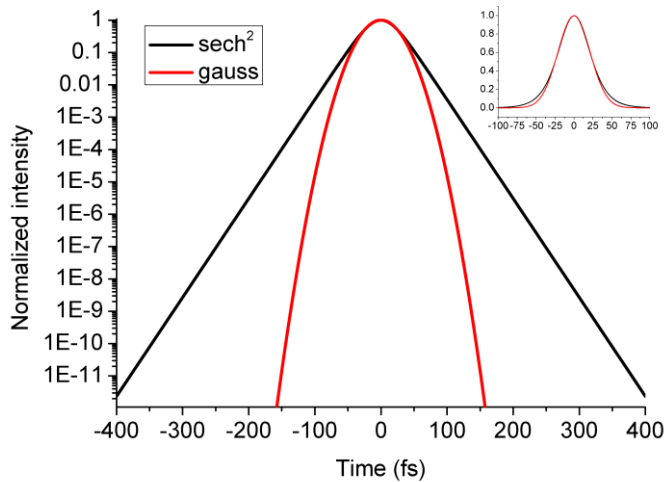


Fig II.2.1. : Temporal distribution of the Gaussian and Hyperbolic sechant pulses of 50fs FWHM

Usually changes are done on the spectrum or in time to control the pulse-shape of the laser. Chromatic dispersion⁸ due to propagation through an optical system, not taking into account non-linear effects can be described as a Taylor-expansion of the $\phi(\omega)$ spectral phase:

⁸ Dispersion is sometimes called **chromatic dispersion** to emphasize its wavelength-dependent nature. There are generally two sources of chromatic dispersion: material dispersion and waveguide dispersion. The term has become more used, since fiber technology has developed to distinguish from intermodal dispersion and polarization mode dispersion.

$$\phi(\omega) = \phi(\omega_0) + \phi'(\omega_0)(\omega - \omega_0) + \frac{1}{2}\phi''(\omega_0)(\omega - \omega_0)^2 + \frac{1}{6}\phi'''(\omega_0)(\omega - \omega_0)^3 + \dots \quad \text{II.14}$$

The zeroth order describes the absolute phase or carrier envelope phase (CEP) and has only significance in few cycle lasers and will be not discussed in detail in the frame of this thesis. The first order derivative, called group delay (GD) describes the delay of the envelope to the carrier.

The second order derivative, called group delay dispersion (GDD) gives the frequency dependence of the group delay and is introduced when pulse length change is desired without affecting the pulse shape itself.

The third derivative, called third-order dispersion (TOD) will cause complicated distortions to the pulse shape by redistributing the frequencies unequally respect to ω_0 . This in return also affects the contrast and is usually to be avoided in ultrahigh intensity laser systems. The level of aberrations together with the pulse bandwidth will determine the magnitude of the effect on the pulse. For narrow bandwidths and hence longer pulses, the lower order terms will be important. For pulse-durations below 1ps GDD starts to become significant and for pulses in the 10's of fs and below region TOD and even higher order dispersion will have significance on pulse shape and hence minimum pulse length and maximum focusable intensity. Pulses with no chromatic dispersion are called bandwidth limited (BWL) pulses, as their length can be directly retrieved from the spectrum of the laser. For each specific pulseshape the so called time-bandwidth product⁹ $K \leq \tau_p \cdot \Delta\nu$ will give information about the shortest possible pulses achievable. The values of K is $2 \cdot \ln 2 / \pi = 0.441$ for Gaussian and 0.315 for hyperbolic sechant pulses.

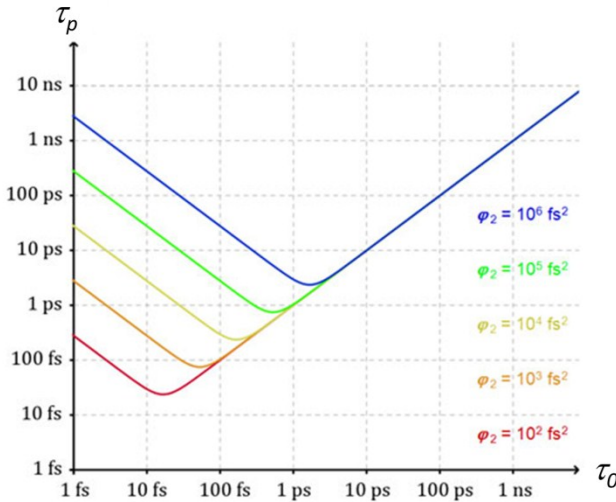


Fig. II.2.2. Effect of second order chromatic dispersion (GDD) on the pulse length

In the case of fs oscillators, the pulses after several roundtrips will gain bigger optical bandwidth as the number of modes increase and will start to suffer from chromatic dispersion due to propagation through the active media or reflection off mirrors, same as described in equation II.14. If GDD or the second order derivative has a magnitude of ϕ_2 , then the resulting pulse length will be for a Gaussian pulse with BWL pulse length of τ_0 :

$$\tau_p = \tau_0 \sqrt{1 + \left(4 \ln 2 \frac{\phi_2}{\tau_0^2} \right)} \quad \text{II.15}$$

⁹ **Time-bandwidth product** is usually defined in terms of frequency ν , rather than circular frequency ω . In both time and frequency FWHM values are taken.

From here one can easily see, that the chromatic dispersion has much larger effect on short pulses, scaling with the reciprocal square of the BWL pulse length (see Fig. II.2.2.). This is another reason, why chirped pulse amplification, described later, is widely used for these sub ps pulses.

Experimentally it is the variation of $\phi(\omega)$ spectral phase which affects the $E(t)$ electric field and hence the pulse duration, without, in an ideal case affecting the $I(\omega)$ spectral intensity itself, such as it is desired in stretchers and compressors. Higher order chromatic dispersion can be a by-product of a misaligned or not well compensated chirped pulse system. Also, in reality the spectrum sometimes extends beyond the physical size of the gratings, or the bandwidth acceptance of mirrors or the measurement system and effects both the spectral phase and the spectral intensity at the same time. On the other hand manipulation and compensation of the spectral intensity $I(\omega)$ for distortions experienced in the optical systems and during amplification can also help in improving pulse contrast. In this chapter I will give a general overview on how elements in traditional Chirped Pulse Amplifier systems (described in II.3.4.5.) affect chromatic dispersion and pulse cleanness, while **in chapter III.5.** I look into calculating the overall effect of these on the pulse shape and contrast.

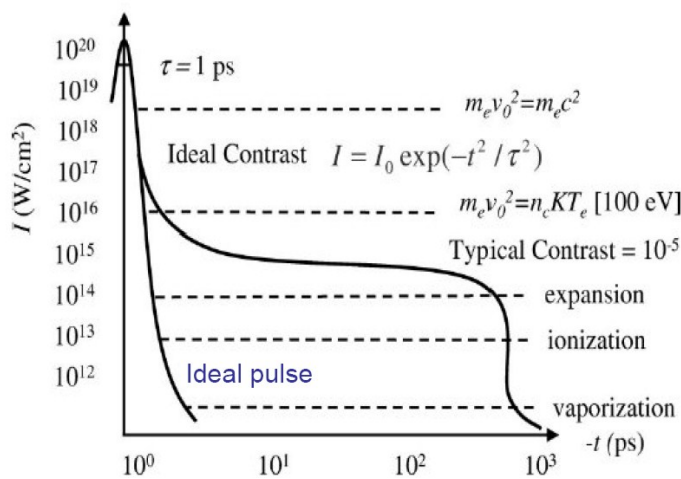


Fig II.2.3.: The role of the pulse shape in high intensity laser-matter interactions

post/prepulses can affect the interaction between the pulse and the material in the experiments (see Figure II.2.3.).

II.2.1.2 Mode-locked oscillators/description of laser pulse-trains

For short pulse generation below 1ns, which is where our interest lies, mode-locking is the most important technique. Most ultrahigh intensity laser systems will have a mode-locked oscillator as their front end. Detailed description of the different mode-locking techniques can be found in several references^{II.17II.18II.19II.20.} Here I will focus on those aspects, which have significance for high micropulse repetition rate photo-injectors.

Brightness has been mentioned before as the most important parameter, which is related to the focusability and the fluence of the ultrashort pulse. When calculating the brightness/intensity one always assumes a certain pulse shape, typically Gaussian or sech². In real systems the temporal shape can be different from these, in some cases pre-or post-pulses can develop. The temporal contrast is one of the most important parameters, as

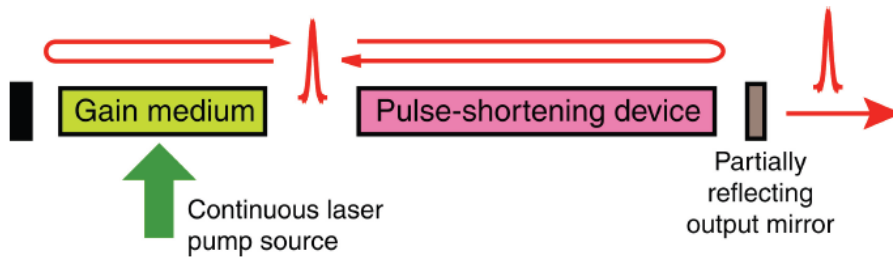


Fig.II.2.4: Basic architecture of an oscillator. Pulse shortening device or mode-locker can be saturable absorber, phase modulator, amplitude modulator, optical-Kerr media...

The oscillator consists of some basic elements: two end mirrors (one of which has a slight leakage, called the output coupler) and the active media, as shown on Fig.II.2.4. The active material is pumped directly by a light source, typically flashlamp or laser diode^{II.19-II.20}. The pumping is based on exciting atoms, ions or molecules through absorption of the pump light, so that energy is stored in the active media. This will radiate through spontaneous emission at a well-defined wavelength range. From this 'noise' or the applied modulation depending on the architecture different modes spatially and spectrally will be selected and amplified by the stimulated emission through many thousands of roundtrips. Inside the resonator, supporting many longitudinal modes, by the use of some mode-locking device the modes are forced to oscillate in precise phase with each other, generating a train of ultrashort pulses. Pulse shortening by the mode-locker and pulse broadening due to gain narrowing and dispersion will reach a steady-state, and an operational condition is reached.

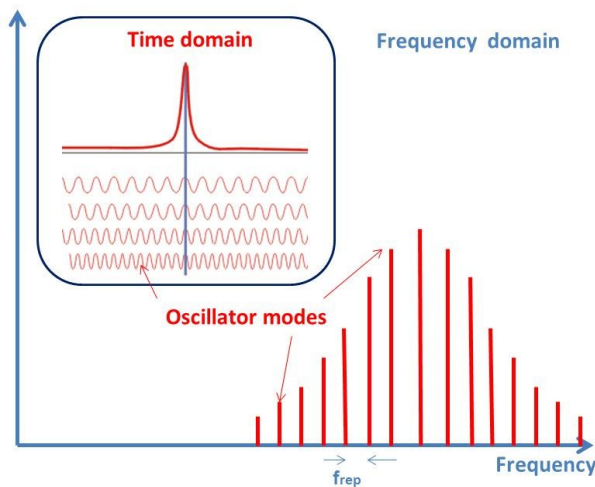


Fig. II.2.5. : Comb line spectrum of a Gaussian pulse train

Starting from a mathematical description by the Fourier-transform of such periodic train of pulses also gives us insight into the underlying physics. The amplitude spectrum of a pulse-train consisting of short Gaussian pulses is a comb line spectrum also with Gaussian profile, as shown in Fig. II.2.5. The comb lines are equally spaced in the spectrum at a distance equal to the nominal f_{rep} , repetition frequency, where:

$$f_{rep} = \frac{c}{2L} = \frac{1}{T_{RT}}, \quad \text{II.16)}$$

L being the length of the resonator, c is speed of light and T_{RT} the cavity round-trip time. The lines in the mathematically calculated spectrum therefore correspond to the modes, which are within the bandwidth of the material and the cavity itself. The Gaussian envelope of the spectrum will be directly related to the length of the pulses. Consequently the number of the lines will increase if the ratio for pulse period and pulse duration increases. These will be the spectral lines utilized in our **experiment described in III.4.** to set up the correct time-delay for the phase-coding needed for the CTF3 laser system (detailed in II.1.3.2.).

Semiconductor Saturable Absorber Mode-locking (SESAM), which is used in the PI laser systems described in later chapters, is based on the fact that a semiconductors' absorption decreases when irradiated by high intensity laser radiation, as the photons will excite electrons from the valence to the conduction band. SESAM mirrors also contain a Bragg reflector with the quantum well absorber in between the Bragg mirror and the surface. In this case the mode-locking is passive and the oscillator pulse-train builds up from noise. Higher peaks will experience less loss and will continue circulating around the cavity. Over some number of roundtrips these fluctuations become stronger. An imbalance between gain-saturation caused by the strong pulses and losses- seen by the weak ones- builds up. However this is a very sensitive imbalance, which can be disturbed by dust or damage to the SESAM, or weak reflection back from the rest of the laser system. Any random increase in the pulse energy will change the saturation level of the absorber further increasing the gain and the energy of the pulse. Noise exhibiting in these types of oscillators, which were also observed in the laboratory, will be **discussed in more detail in II.4.3.** The main advantage of this technique is that it is passive and so it allows turn-key operation of the oscillator.

Ultrashort pulse oscillators often use self mode-locking, which is based on the Kerr-effect in the active media, typically Ti:Sapphire, like the one at TeWaTi. When high intensities, such as when a high-energy ultra-short pulse is focused into a material, the nonlinear properties of the material are no longer negligible. The refractive index becomes a function of the intensity. This in turn causes a delay of the beam, which is intensity dependent and is hence the largest at the centre of the beam and smallest in the wings. The distorted wavefront then leads to focusing (Kerr-lensing). That is why this way of mode-locking is called KML (Kerr Lens Mode-Locking).

The temporal and spatial modes coupling makes the design complicated. When a hard aperture is used the Kerr-lens decreases the losses at each roundtrip through the aperture. In the case of a soft aperture KLM, the overlap between the pump and the oscillator mode leads to higher gain at the centre of the pulse. Unlike the SESAM ML technique here usually an initial disturbance that has to be introduced the to cavity to start the mode-locking.

II.2.2 Amplification of ultrashort laser pulses

As oscillators typically only generate an average power of few hundred milliwatts- see above- further amplification is required for our applications. At the required 1.5GHz repetition rates for the CTF3 injector laser the single pulse energy from the oscillator is below a nJ.

There are two main approaches in infrared laser pulse amplification. The first is power amplifier, where (as in the oscillator) the active media is pumped by an external source and the pump power is stored in the material on the scale of the materials fluorescence lifetime. Pulses can either propagate through the gain material in many passes and keep the mode-locked structure of the seed (Master Oscillator Power Amplifier) or can build up large energies in a single pulse in a resonator (Regenerative amplifier). Fiber based amplifiers are emerging, but due to non-linear effect they are still limited to fairly low peak pulse powers and are often used to boost the power of the high repetition rate oscillator up to ~10W, as will be done in our case for the CTF3 PI laser.

Optical amplification is possible by other means, which are based on optical nonlinearity of a material. The approach is to amplify the IR pulses in a nonlinear optical material, and by using parametric process transfer the pump light of a laser working at a shorter wavelength into the signal beam. Here there is no energy storage and energy transfer can only take place, when pump pulse is present. Optical parametric amplifiers can cover a wide range of wavelengths from 300nm-4µm. Most of the commercially available tuneable wavelength sources are based on parametric oscillators or amplifiers.

Depending on the repetition rate and the micro pulse structure (in the case of PI laser), and the maximum pulse length broadening as well as bandwidth preservation in these systems different architectures can be chosen. Pulse cleanness and contrast is also important at the end of the amplification process. Oscillators usually deliver clean TEM00 spatial modes, which are best to be preserved during amplification as much as possible.

Staging of the amplifier system can be helpful for thermal management and dispersion control, beam profile cleaning between stages, as well as for isolation or pulse temporal shape cleaning. In all cases to avoid non-linear effects and damage Chirped Pulse Amplification can provide the tool for reaching high pulse energies with moderate pulse intensities. These systems will be briefly described in the following.

II.2.2.1 Gain saturation, steady-state

Small signal gain, as the name suggests is the gain obtained, when a very weak signal is passing through the amplifier. In the case of the single pulse this is described by the ratio of the output and input pulse energy. As arbitrarily high output intensities would only be achievable with arbitrarily high pump power and stored energy. Hence under normal conditions the gain obtained is less than the small signal gain. This is called gain saturation. The intensity of the signal has to be well below the saturation intensity of the material to satisfy small signal condition. Saturation intensity of a material is defined by:

$$I_{sat} = \frac{h\nu}{\sigma_e \cdot \tau_{fl}} = \frac{F_{sat}}{\tau_{fl}}, \quad \text{II.17)}$$

where h is the Plank constant, σ_e is the emission cross-section of the material, τ_f is the fluorescence lifetime and F_{sat} is saturation fluence. Note, that F is still exchangeable to power density I (intensity) in the case of cw amplification or amplification of pulse trains in our case^{11,22}. This is valid, as in the case of single short pulse amplification the spontaneous emission and hence fluorescence lifetime does not have a significant effect on the timescale of the pulselength.

The saturated gain along the length of the amplifier for a pulse train can be described as:

$$g(z) = \frac{g_0}{1 + I(z)/I_{sat}}, \quad (11.18)$$

where g_0 is small signal gain coefficient, z is the propagation direction along the rod, $I(z)$ is the reached average pulsetrain intensity at this part of the amplifier. If we assume, that inversion does not change during the pulse transit time, then the signal density build up can be described as:

$$\frac{dI}{dz} = g(z)I(z) \quad (11.19)$$

For large signal levels, which will be the case for the final amplifier for CTF3 and CLIC, where $I(z) > I_{sat}$ the following approximation will be valid as a relation between input and output intensity^{11,20}:

$$I_{out} = I_{in} + I_{sat}g_0L, \quad (11.20)$$

where L is the length of the crystal. Inserting eq.11.18 into eq.11.20. and integrating along the length of the crystals gives the following expression:

$$\frac{I_{in}}{I_{sat}} = \frac{\ln(G_0 / G)}{G - 1}, \quad (11.21)$$

where G_0 is the actual small signal gain measured with extremely slow input seed levels and G is the saturated gain. G_0 is only dependent on the pump rate¹⁰, I_{sat} is the property of the material used and when pumping is fixed the actual gain will only be dependent on the input fluence or average pulse train intensity. For example, the gain is reduced by a factor of ~5 of the small-signal gain when the input fluence or intensity equals to the saturation fluence/intensity. As seen from Fig. 11.2.6. at seed levels well above saturation the gain is going to be limited, also limiting the maximum achievable output power. This will be the case for the final amplifier for CTF3. Here if the pump power is increased to achieve higher small signal gain it does not result in higher saturated gain. In this case increasing the beam size to achieve lower input fluence can give a bigger overall gain.

¹⁰ The fraction of the pump light, which contributes to the upper laser level population.

Gain saturation in steady-state

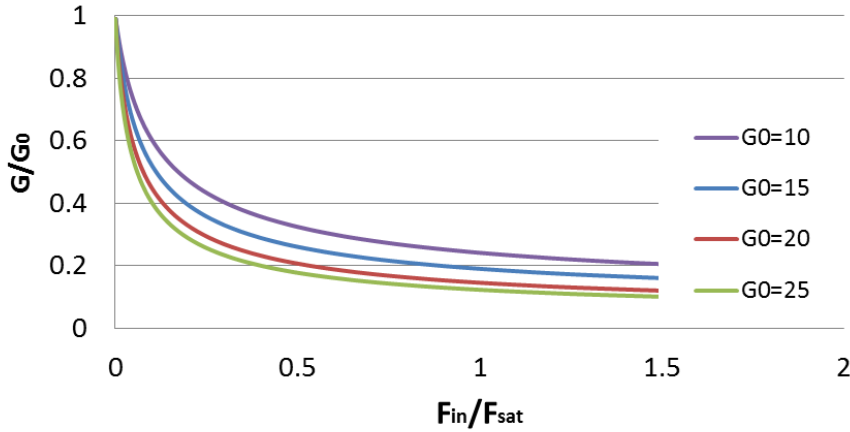


Fig. II.2.6. The gain reached at steady-state as a function of input fluence from equation II.17.

Calculations for large gain are more complex as optical intensity varies significantly within the amplifier. The approach taken is to divide a high-gain amplifier into a sequence of short, low-gain amplifiers, as it will be presented in III.1.3.

To see how steady-state builds up in a power amplifier, let us look the balance between input, output and losses. The calculation is applicable to cw input or pulse trains (average power), if each individual pulse does not change the upper laser level population considerably. The fluorescence losses and the extracted power will hold balance with the induced pump power, which can be described in the following equation, assuming homogeneous pump distribution:

$$P_{out} - P_{in} = P_{out} \left(1 - \frac{1}{G}\right) = \eta_l P_{pump} - A \cdot \frac{I_{sat}}{p} \cdot \ln G \cdot (1 + B_{ASE}), \quad \text{II.22}$$

where P_{out} is output power, P_{pump} is absorbed power, η_l is the portion of the pump power, which contributes to population inversion of the upper laser level¹¹ and p is the number of passes. B_{ASE} is the contribution to the losses by amplified spontaneous emission (ASE) which is often difficult to estimate in a design. More detailed description of ASE **will be given in II.2.2.7**. For example, inserting the values for Nd:YLF, setting $B_{ASE}=0$ and taking the output requirement for CLIC of $P_{out} = 29kW$ scaling from the CTF3 amplifier with a gain of 4 and an extracted area corresponding to 1cm diameter gives a value of 29.9kW for absorbed power. If we assume the 90% of the pump power is transferred to the rod and 80% of this is absorbed, then this gives a total pump power of 41.5kW. A comparison between single and multi-pass amplification can also be made using equation II.22. For amplifiers with the same gain the fluorescence loss term is inversely proportional to the number of passes and consequently will require reduced pump power to reach the same gain. For the example above the difference between single and double pass means 0.48kW reduction of the pump power for the same gain.

¹¹ This coefficient includes the pump transfer efficiency, the pump absorption efficiency, the quantum efficiency of the pumping process (the fraction of the absorbed pump photons which contributes to the population of the upper laser level), and the quantum defect (the ratio between the lasing photon energy and the pumping photon energy).

It is possible to achieve up to few μJ pulse in a single pump unit by directly amplifying the oscillator pulses. When pumping times are comparable to, or longer than the fluorescence lifetime of the active media, then steady-state is reached. Amplifiers often running in burst mode, when high mean power levels in steady-state at the kW level are needed (as the example on Fig.II.1.3 shows). Once the required length of pulse-train is reached in the steady-state pumping is turned off, until the next burst is needed. This way thermal effects are minimized, but they still take advantage of the stable operation in the steady-state saturated regime.

It is worth to mention here, as stability is important for our applications, that although amplifiers offer the ability to correct for the long term amplitude drift of the seed laser, when run in saturated steady-state, at the same time they exhibit very high small signal gain in this case and are very sensitive to back reflections, causing parasitic lasing. Isolation of the different stages of the system therefore is crucial.

Design choices made specifically for the photo-injector laser at CERN **are detailed in chapter II.3.**, while the full design of the pump chamber and the performance of the amplifier **are reported in III.1.** together with the detailed description of the specific model for the used multipass side pumped rod geometry.

II.2.2.2 Master Oscillator Power Amplifiers

The term *master oscillator power amplifier* (MOPA) refers to a setup, where a master or seed laser generates the required pulses and an optical amplifier boosts the output power. The seed (master oscillator) is passing through a bulk amplifier, where the material is pumped by an external source, such as a flash lamp or laser diode (Fig.II.2.7.). MOPA configuration offers to keep spatial and temporal properties of the master oscillator, while scaling to higher power. As performance, such as

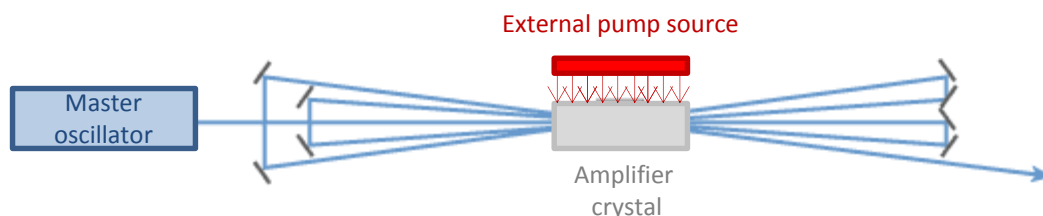


Fig. II.2.7. Example of a multipass scheme with angular multiplexing, where beams passing through the amplifier at different angles.

pulse length, line width, wavelength tuning range are dependent on the high beam quality laser oscillator source, they can be decoupled from the effects associated to the generation of the high power, by having an external boost of laser power. When feedback or modulation is required to deliver a specific pulse train envelope it is easier to modulate the low-power seed laser, or to use an optical modulator between seed laser and power amplifier, rather than directly modulate a high-power device. We will take advantage of this when phase-coding is implemented in the CTF3 laser system (III.4.3.) Slower power changes to compensate for drifts may be done by adjusting the amplifier's pump power, without changing the quality of the beam. Scalability of these systems is easier; hence additional amplifiers can be put to the end of the system. The optical intensities are lower in an amplifier,

compared with the intracavity intensities in a laser and hence nonlinear effects are less significant. All of these advantages are utilized for the development of amplifier stages for the CERN PI.

To reach steady-state fast and to get high gain the seed has to pass through the material many times, especially during the early amplification stages. However, as multi-passing a rod amplifier geometry is done by angular multiplexing, as shown on Fig.II.2.7., losses between passes often result in no increase of net gain after a few passes. Multipass configuration still offers a high gain and high extraction efficiency solution.

II.2.2.3 Pumping geometries / diode pumping

Many different pump geometries are available depending on the gain coefficient, the overall gain required, the thermal properties of the optical media and the average power to be reached, as well as the pump source brightness. More detail can be found in^{II.20.}. A side pumped rod geometry is shown in Fig. II.2.8.

Before the 1980's the extremely high cost of laser diodes prevented their everyday application in high power systems. However the compactness, efficiency, maintenance and lifetime made it attractive for some applications and so the market started to grow and the higher volume production eventually decreased the cost/Watt in the last decade. The lifetime of these diodes has increased to 2×10^9 shots, and by developing the micro-channel cooling system, stacked arrays providing extremely high compactness 2 kW/cm^2 directly radiated peak intensities are available^{II.44}. The emission of the diode is a light cone (usually 40° in one direction and 10° in the orthogonal) with small emitting area. Micro lensed and fibre coupled options are available for mode-matching with high brightness, although for pumping large rods the natural divergence can be utilized.

When side pumped rod geometries are used in conjunction with laser diode pumping scalability becomes easy by adding more arrays along the length of the rod. Diode pumping with array sizes (typically $\sim 1\text{cm}$) often close to the transverse size of the optical media and with stacks offering high pump power, matching also the length of the crystal make efficient pumping possible^{II.23.}. As uniform pumping can easily be achieved in a large volume, thermal load and stress can be reduced, when compared to end pumped configurations. Single pass gains of ~ 10 are typical for commercially available, so called pump modules. These pump modules also offer easy scalability of the power and with careful design of the gain profile in a side pumped rod configuration, beam quality of the oscillator can be preserved to a large extent. Although the power of laser diodes still won't compete with that for flashlamps, there are several other advantages of using diode lasers, see Table II.2.11.

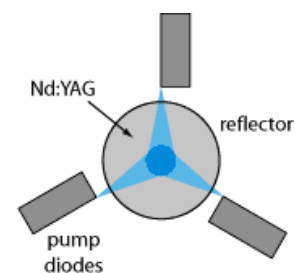


Fig. II.2.8. Side pumped rod geometry with diodes.
(<http://accessengineeringlibrary.com>; RP photonics)

Table II.2.1. Comparison of diode and flashlamp pumping

Property	Laser diodes	Flashlamp
Electrical to optical efficiency	25-85%	45%
Emission bandwidth	Exact match with Nd doped materials	Broad, causing heat, thermal aberrations, and material degradation (UV)
Lifetime	2*10 ⁹ shots pulsed 10 ⁴ hours cw	<10 ⁸ shots pulsed 500 hours cw
Repetition rate	Up to few kHz ¹²	Low repetition rate

The exact match between the absorption spectra of the Nd doped materials (808 nm) and the emission spectra of the diodes – which is tuneable by the cooling temperature- requires much smaller cooling devices and helps to suppress the thermal aberration in the system, which implies better beam quality. This in the same time also increases optical to optical efficiency, as shown in Fig. II.2.9.

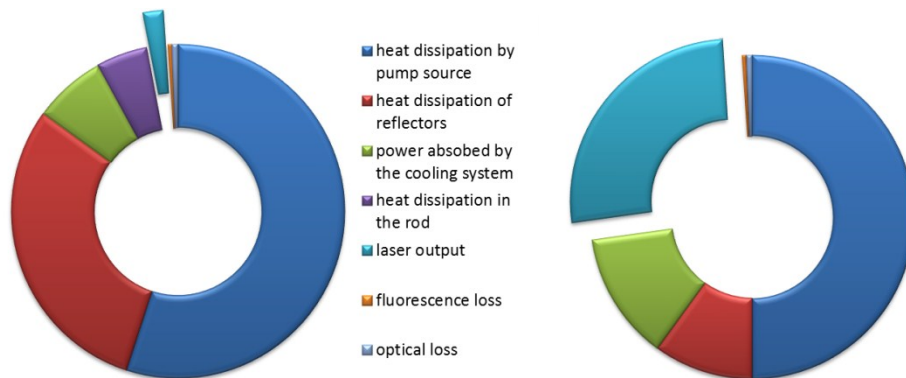


Fig. II.2.9. Typical distribution of the electrical power in a flashlamp pumped (left) and a diode pumped (right) system, showing that much larger fraction of the power is utilized at the optical output and much lower goes into heat in the case of diode pumping.

For some applications narrow band absorption is desirable, but for large rods a few nm bandwidth can help to increase homogeneity along the length of the absorption and to make the amplifier less sensitive to temperature variations.

Although the initial cost of the diode is higher than a flashlamp for the same power, lifetimes are typically much higher and can be even further extended by cooling below room temperature and running at 90% of the maximum operating current. However the static sensitivity of the device calls for environmental control and careful design of the drive electronics.

II.2.2.4 Regenerative amplifiers

Architecture of these lasers can be very similar to those described in the previous section, but this time the active medium with a population inversion created by pumping is placed inside a resonator. The cavity for this reason contains one or two optical switches to switch in the seed pulse provided by a mode-locked oscillator and to switch out the pulses after amplification when the stored

¹² Here we are talking about high power diode arrays, where ~100W of power is generated by a single array. Higher repetition rates are possible in single emitters.

energy has been removed by the seed after several round trips. A combination of a fast electro-optical switch (Pockels-cell) and a thin film polarizer is generally used for switching. The intracavity pulse energy can be monitored to achieve the ideal timing for switching out the pulses. Gains up to 10^6 and pulse energies in the mJ range can be achieved with this technique. However the maximum repetition rate is limited by the speed of the available electro-optical switches and is limited to the few MHz range.

It is worth to mention here, that in both high gain multipass amplifiers and regenerative amplifiers the spectrum of the seed pulse can be affected by gain narrowing and can result in lengthening of the pulse. A spectral filter inserted in the amplifier, which makes the net gain spectrum wider and flatter can compensate for this.

II.2.2.5 Chirped pulse amplification

When a single pulse is amplified in storage material the extraction efficiency, defined by extracted energy/ stored energy, will be optimum, when input fluence of the laser pulse is a few times the saturation fluence of the material^{11,24}. Solid materials compared to dyes and excimers can store 1000 times more energy in a unit volume. However as saturation fluences in solid materials are high due to their small stimulated emission cross-section, high focused intensities ($>1\text{GW}/\text{cm}^2$) are required for direct, efficient amplification of ultrashort laser pulses. In this case the nonlinear properties of the material are no longer negligible. The refractive index becomes a function of the intensity, similarly to the effect utilized for Kerr Lens Mode Locking.

$$n = n_0 + n_2 I, \quad \text{II.23)}$$

where n_0 is the refractive index and n_2 is the non-linear refractive index of the material. The total on-axis nonlinear phase shift experienced by the pulse when propagating through a material of L length is described by the B-integral (not to be confused by the B introduced for ASE).

$$B_{NL} = \frac{2\pi}{\lambda} \int_0^L n_2 I dz \quad \text{II.24)}$$

When B_{NL} is greater than 1 it can lead to beam-distortion, break-up, filamentation of the beam and damage to the system components through the hotspots, which are generated. If $1\text{J}/\text{cm}^2$ needs to be extracted from e.g. Nd:Glass amplifier then the intensity levels for efficient extraction at $1\text{TW}/\text{cm}^2$ would correspond to B_{NL} of ~ 1000 .

To overcome this problem CPA (Chirped Pulse Amplification) has been developed^{11,25}. The oscillator generates a train of pulses with pulse energy around nJ, and $\sim 100\text{MHz}$ repetition rate, these pulses are then stretched temporally with a pair of gratings or prisms to reduce the peak intensity, by introducing a delay between the different frequency components of the beam, using the second order dispersion (GDD) described in eq. II.14. These stretched pulses are then amplified in a regenerative amplifier or in a parametric amplifier. The gain can be up to 10^{12} . After the amplification process an opposite group delay dispersion is applied on the pulse in order to compress the pulse close to its diffraction-limited length as shown on Fig.II.2.10.

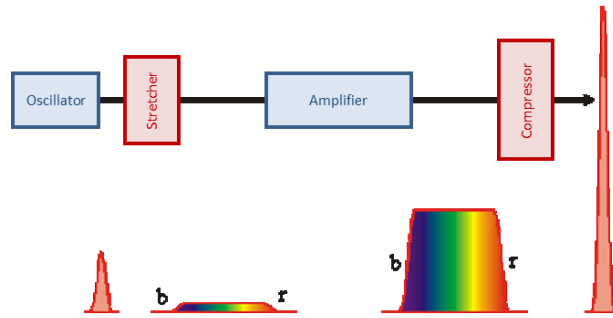


Fig.II.2.10. The CPA. O: Oscillator S: Stretcher A: Amplifier C: Compressor.
The intensity is reduced during amplification and then compressed.

The system components have to be well matched and the effect of amplification (dispersion, non-linear effects, gain saturation and gain narrowing) have to be taken into account. Referring back to Fig.II.2.2. we can see, why this technique is mainly used for sub-ps laser pulses, where the GDD to be introduced needs to be relatively small to achieve long pulses for amplification. This means a shorter length for stretchers and compressors and hence more compact systems. However, the stretcher and the compressor have to accommodate the broad bandwidth associated with these short pulses and the following optics have to withstand the high intensity. Operation in vacuum is sometimes necessary to avoid air breakdown. To achieve diffraction limited pulses any spectral distortions, such as clipping, gain-narrowing must be avoided. Sometimes spectral filtering between stages of amplification can pre-compensate for such effects. The CPA technique is also used widely for high intensity parametric amplifiers described in the following section. Here, apart from reducing unwanted nonlinear effects, matching the pulse length of available high single pulse energy pump-lasers will make the process more efficient.

II.2.2.6 Optical parametric amplification

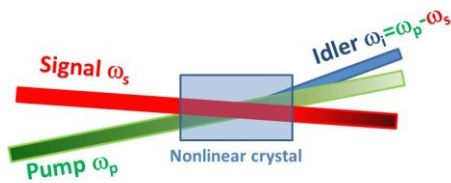


Fig.II.2.11.: An example for Optical Parametric Amplifier

The gain medium of the parametric amplifier is a nonlinear crystal with non-zero second order susceptibility. As this is a non-linear effect I will describe physics behind the process in detail in II.4.1, when non-linear susceptibilities are introduced. A typical arrangement of

three-wave interaction during OPCPA is shown on Fig.II.2.11.

The signal pulse, is usually produced by a short pulse laser. The pump is provided by a second laser, which operates at a shorter, more energetic, wavelength. For high pump energies Q-switched lasers are a popular choice. There is a by-product pulse produced during this process, called the idler, which is generated at the difference frequency of the pump and the signal. The amplification is only possible, when the two pulses (pump and signal) overlap temporally and spatially in the crystal. There is no stored energy in the material.

The complexity and cost of these systems makes them attractive only once they are used in conjunction with the CPA technique described above and ultrahigh intensities are required. In this case the broadband seed can be stretched to the right length to match the pump pulse length and therefore efficient use of the pump energy can be achieved^{II.26-II.27}. The gain achieved in these amplifiers will be proportional to the square of the crystal length when no saturation occurs and will be proportional to the intensity of the pump pulse. With certain phase-matching configurations ultra-broadband amplification up to 300nm is possible, which is not possible in conventional solid-state amplifiers. Since there is no stored energy in the crystal thermal management is not an issue for these types of lasers. **Contrast of the pulse will be further discussed in II.4.4.** Here it is worth to mention, that if the pump pulse duration is relatively short and matched to the duration of the stretched seed (signal), then improvement in the pedestals is possible, while achieving high gains at $\sim 10^6$. Indeed diode pumped laser amplifiers described in the previous section are becoming an attractive choice compared to Q-switched lasers as a pump, when generation of few cycle laser pulses are desired.

II.2.2.7 Amplified spontaneous emission

The pumping level and the population inversion in a material will hold balance with the extracted power and the fluorescence losses, as described in Eq. II.18. Moreover fluorescence losses, which are emitted in every direction, can still be guided down the active material, especially in long laser crystals with high single pass gain and depending on the geometrical arrangement reflected back in many passes for further amplification. This so called amplified spontaneous emission (ASE) can put serious limitations to the achievable gain, cause instabilities or be present at a relatively low level during the pumping and cause long pedestals around the pulse. These are unwanted both for high stability to be achieved for the photo-injector lasers and the high contrast required for ultrashort high intensity laser based material science. Isolation of the different passes and amplifiers stages is therefore important in high gain systems and rough surface rods, antireflection coatings for the lasing wavelength as well as wedged rods will all help to fight parasitic oscillations, which can build up from ASE when strong coupling is present.

The effect of the ASE in amplifiers is to increase the rate of depopulation of the upper laser state and hence limit the achievable steady-state gain. It has been studied in detail to estimate the level of ASE in the case of the CLIC photo-injector's amplifiers by I.N.Ross^{II.28}. This increased depopulation will also appear as a reduction of the upper laser level lifetime. The effective lifetime can be written as:

$$\tau_{eff} = \frac{\tau_{fl}}{1 + B_{ASE}}, \quad \text{II.25)}$$

where τ_{fl} is the fluorescence lifetime measured in the case of spontaneous emission and τ_{eff} is the effective lifetime due to ASE.

The fluorescence power from a volume element dV at a distance r from a point P in the rod and crossing an area element dA at P is given by:

$$f \frac{N}{\tau_{fl}} h\nu \cdot e^{g_0 r} \frac{dVdA}{4\pi r^2}, \quad (11.26)$$

where f is the fraction of the population inversion N , which fluoresces at the laser wavelength. The corresponding fluorescence intensity dI_{fl} is then given by:

$$dI_{fl} = f \cdot g_0 \cdot I_{sat} \cdot e^{g_0 r} \frac{dVdA}{4\pi r^2}. \quad (11.27)$$

This leads to a rate of change of excited state population at P of $(N/\tau)(dI_{fl}/I_{sat})$ and a consequent value of B_{ASE} given by:

$$B_{ASE} = f \cdot g_0 \int_{rod} \frac{\exp(g_0 r)}{4\pi r^2} dV. \quad (11.28)$$

As the geometry of the multipass amplifiers also allows multiple passes for the ASE and coupling factors are difficult to define, this parameter was left free for gain calculations and was determined by obtaining best fit to the measured values.

Indeed, parasitic lasing, caused by optical feedback of the ASE signal from imperfect antireflection coatings was observed at the early stages of the laser development, causing instabilities and occasionally damage to optics. Later with good isolation both spatially and with magneto-optic (Faraday) isolators ASE feedback was reduced to a negligible level.

11.2.2.8 Gain narrowing

Transform limited pulses entering an amplifier have a certain bandwidth, which could be modified by the gain spectrum of the medium. Generally this leads to higher amplification for the central part of the spectrum and hence narrowing of the spectrum. This is called spectral gain narrowing, which will translate to the lengthening and changing shape of the pulse. Estimation of the gain narrowing in our case for the photo-injector laser is not critical, but is interesting and will be briefly discussed in later chapters. It is also worth to mention here, that the effect also depends on the gain and on saturation level (which can have the opposite effect) and so for regenerative amplifiers the severity of gain narrowing, especially for ultrashort pulses will call for the application of spectral filters (active or passive) to pre-compensate for this.

11.3 Photo-injector lasers

Typically all PI laser systems start with a mode-locked oscillator running at a harmonic of the RF frequency, oscillators are now commercially available with active cavity length control for synchronization. They can provide down to ~200 fs timing jitter performance. Architectures exist from MOPA, regenerative amplifiers, CPA to fibre amplifiers with required pulse structure, energy/ pulse and pulse shape to reach the charge and electron beam quality specification.

The CERN application requires a non-conventional type of laser system since we want to generate long pulse trains at GHz repetition rate, which cannot be regarded as cw. High gain is required but the pulse structure doesn't allow for a regenerative amplification scheme.

II.3.1 Existing laser systems

Table II.3.1 shows some electron sources around the world based on laser driven photo-injector, including the one, which is subject of this thesis. The often unique pulse-structure requirement to match the RF used in the accelerator complex calls for an unusual architecture, where many thousands of pulses have to be amplified to the same energy often with unusually high mode-locked repetition rates. As a relatively high macropulse energy needs to be achieved, these systems are usually running in burst mode to avoid thermal effects and damage. The repetition rate of this macropulse is often what determines the pumping source itself. As stability is becoming increasingly important with the development of XUV FEL's, diode pumping has become the choice because of better stability and controllability of the absorption and hence the population inversion and gain in the active material. The repetition rate required from the oscillator is usually within the range, which is commercially available with synchronization to external source built into the laser. Some previously developed diode-pumping cavities can be used and there have been a number of novel approaches^{II.29,II.30,II.31,II.32} with high efficiency. Systems with high gain and high efficiency have also been developed, but often using the more complex regenerative amplifier^{II.33II.34II.35}. The need for laser systems in accelerator development, particularly for photo-injectors, has led to development of pulse train systems^{II.36II.37II.38}. However the need for extreme short and long term stability of photo-injectors has not, so far, reached the required level. So the aim of this work was to create both an efficient and high gain system, with high stability.

Table II.3.1. PI lasers and their basic parameters (Ref.II.38,II.39,II.40,II.41,II.42)

	ELSA (FEL)	FLASH (FEL)	TESLA (FEL)	APSPDL	ELETTRA (FEL)	CTF3/ PHIN
Material	Nd:YAG	Nd:YLF	Nd:YLF Nd:Glass	Nd:Glass	Ti:Saph	Nd:YLF
Pulse length on cathode	30ps	4.4ps	20ps square	2-10ps	6-15ps	6ps
Pumping	Flashlamp	Diode and flashlamp	Flashlamp	Flashlamp	Diode	Diode
Harmonic	2 nd	2 nd 4 th	3 rd and mixing with glass laser	2 nd and 4 th	3 rd	2 nd 4 th
Wavelength on cathode	532nm	262 nm	263nm	532nm 263nm	261nm	262nm
Cathode	K2CSSb	Cs2Te	Cs2Te	Cs2Te	Copper	Cs2Te
Macropulse reprate	1Hz	Up to 10Hz	10 Hz	6Hz	Up to50Hz	1-5 Hz

Micropulse replate	14.44MHz	27 MHz	1 MHz	Single pulse		1.5 GHz
Pulse train length	150μs	1 pulse-800 μs	800 μs			1.3 μs
Energy/pulse IR	10 μJ	300 μJ	200 μJ	6000 μJ	15000 μJ	5 μJ
Macrop. Stability	3%	?	3% (<10%)	1.7%	0.8%	1.5-3% (<0.5% in IR)
Microp. Stability	?	1-2%	? (<5%)			?
Stabilizer	Pockels-cell	-	PC and flashlamp	-	None	None yet
Transmission	67%	-	?	-	-	-
Macrop. stab.	1%	-	0.7%	-	-	-
Microp. stab.	0.8%	-	0.9%	-	-	-

II.3.2 Available gain materials

The choice of material is determined by many different parameters:

- the available pump sources for the given absorption band will determine the efficiency of the pumping
- the pulse shape and length and rise time are important for low emittance machines for FEL, thus broadband laser materials are needed for spectral manipulation or stacking of several short pulses
- the fluorescence lifetime of the material will set the limit of the longest extractable macropulse, although pre-pumping techniques could slightly extend beyond this timescale
- stimulated emission cross-section and small signal gain for given a pump will determine the number of stages required for the laser amplifier chain
- the thermal properties of the crystal will determine the scalability of the system to high average powers and ultimately the complexity of the final system as well as the quality of the beam
- the available oscillators with high repetition rate and their power level will also have a net effect on the complexity of the system.
- saturation fluence together with available crystal sizes and their thermal fracture limit will determine the maximum fluence which can be extracted efficiently from a single amplification stage
- the difference between the pump and the emission band determines the proportion of the power converted into thermal losses and will limit the average power or complicate the cooling required

Table II.3.2. lists the main parameters for those materials, which could be considered for operation at 262nm range using Cs₂Te cathodes.

Solid-state gain media based on ion-doped crystals or glasses typically have small laser cross sections due to the weakly allowed transitions. The large saturation fluences and intensities and long fluorescence lifetime makes energy storage and extraction efficient. However for passive mode locking, they tend to exhibit Q-switching instabilities.

For generating short pulses for the above mentioned pulse and shaping to flat top, the material has to support the bandwidth. In this case Nd:YLF and Nd:YAG don't meet the requirements. Nd:Glass is able to support sub-ps pulses and permits high energy storage efficiency. It is a good choice for single pulse amplification; however for steady-state operation with long trains and relatively high average powers crystal based materials can deliver higher gain and exhibit better thermal properties. Ti:Sapphire has a gain peak around 790 nm, so the 3rd harmonic would be suitable for the Cs₂Te photo-cathodes. The bandwidth supports fs pulses, but large external pump-lasers are required for the pumping in the amplifier(s). Because of the short upper laser level lifetime the pump has to be on a few microsecond timescale. (Q-switched, flashlamp pumped, ns frequency doubled Nd:YAG or Nd:YLF lasers are commercially available). Cr:LiSAF is one of the new materials, which has got a slightly higher emission wavelength (850 nm), than Ti:Sa, its 3rd harmonic is still applicable for the photo-cathode, and the lifetime (67 μs) of the upper laser level makes it compatible with diode pumping. This option would give the most compact system, if diodes were available in the absorption band.

Table II.3.2. Important parameters of materials considered for PI application^{11,20}

PARAMETER	Nd:YAG	Nd:YLF	Nd:Glass	Nd:YVO ₄	Yb:YAG	Ti:Sa	Cr:LiSAF
Lasing wavelength[nm]	1064	1053, 1047	1054	1064.3	1030	670–1070	780–920
Harmonic required	4 th	4 th	4 th	4 th	4 th	3 rd	3 rd
Pump bands [nm]	750, 810	750, 810	750, 810	808.5, 880	940	440–580	440, 560–690
Fluorescent lifetime [μs]	230	480	290	100	1000	3.2	67
Emiss. cross-section ×10 ⁻¹⁹ cm ²	6	1.2, 1.8	0.42	15.6	0.18	3	0.48
Saturation Fluence [J/cm ²]	0.32	1.58, 1.05	4.5	0.123	10.6	0.8	4.9
Pump int. for X2 gain [kW/cm ²]		10	45		81		
Therm. cond. [W/mK]	13	6	1.19	0.05		42	3.09
BWL pulse duration [ps]	18	8	0.15		0.5	<0.1	0.075

For the CERN photo-injector laser <10ps Gaussian pulses were required and hence complicated pump techniques could be eliminated. This also cuts Nd:YAG out from the choices because of its limited bandwidth just supporting 18ps pulses. Nd:YVO₄ and Nd:YLF are both naturally birefringent and so for high power operation the thermally induced depolarization losses are best avoided. Nd:YVO₄ is an attractive material for diode pumping with relatively large absorption bandwidth it is less sensitive to the temperature induced wavelength drift of the diodes. Absorption is very high allowing pump absorption even in short crystals. However the short fluorescence lifetime would not be compatible with the 140μs operation of CLIC and the thermal conductivity is poor, which would also limit further scaling to the system to high average powers.

Thus the choice for Nd:YLF was made for several reasons. The long fluorescence lifetime allows for steady-state operation in burst mode for the required train length and stimulated emission cross section allows for efficient energy storage. Nd:YLF has relatively high gain, and is available in large sizes which makes scalability easier even with the relatively limited fracture limit (22W/cm) for this material. The thermal power in the case of YLF is 32% of the output power. Even for the CLIC requirement with an average power of 600W it will be possible to find suitable crystal length and cooling technique to avoid fracture. Moreover it has been demonstrated for other materials that etching the rod barrel surface to eliminate micro-cracks can increase the fracture limit by an order of magnitude, so it is expected that by using this surface finish fracture will not be an issue for the amplifiers needed for CLIC/CTF3/CTF2. Available crystal sizes allow for rod geometries, where pump power can be evenly distributed along the length of the rod (rod lengths up to 101.6 mm and diameters up to 9.5mm are currently available). Thermal properties of Nd:YLF are listed in Table II.3.3.

Table II.3.3. Thermal properties of Nd:YLF

Parameter	Value
Young's modulus	$E = 8.5 \cdot 10^{10}$ Pa
Poisson ratio	$m = 0.33$
Pump wavelength	$\lambda_p = 806$ nm
Laser wavelength	$\lambda_l = 1047$ nm
Doping concentration of Nd³⁺	1.0%
Refractive indices	$n_a = 1.448, n_c = 1.470$ (@1047 nm)
Thermal optical coefficient	$dn_a/dT = -2.0 \cdot 10^{-6}/K$ $dn_c/dT = -4.3 \cdot 10^{-6}/K$
Thermal expansion coefficient	$c = 8.3 \cdot 10^{-6}/K$ $a = 13.3 \cdot 10^{-6}/K$
Thermal conductivity	$k = 6.0$ W/(m K)
Absorption coefficient	$a = 2.4$ cm ⁻¹ @806 nm
Cooling temperature	$T_0 = 293$ K

II.3.2.1 Thermal effects

Now, that we have selected Nd:YLF as the preferred material and a side pumped rod geometry as the ideal amplifier architecture let's look in detail at the associated thermal effects in this case. There are two aspects to take into account apart from the fore mentioned for fracture limit. One is the cooling of the rod, the second is the beam distortion caused by the birefringent nature of Nd:YLF and the average power. The cooling rates for rods in water are in the range 1-10W/cm² K at flow rates

of 4-40 l/min. With relatively low flow rate of 5l/min and with thermal deposition rate of 140W into a 1cm dia. x 10cm rod, the water would heat by ~5°C.

Although beam distortion in the case of Nd:YLF is relatively low, the distortion will be different in the direction of the optical axis and perpendicular to it due to its birefringence. At 1047nm^{II.45} the thermally induced focal lengths for o and e rays are:

$$f_o = 2.2 D^2 / P_{th} \quad \text{II.29)}$$

$$f_e = -0.62 D^2 / P_{th}, \quad \text{II.30)}$$

for D rod diameter in mm and P_{th} thermal deposition in W. For example, for $D = 10\text{mm}$ and $P_{th} = 200\text{W}$: $f_o = 1\text{ m}$; $f_e = -0.38\text{ m}$. Thermal lensing measurements performed on the CTF2 laser will be **detailed in III.1.3.6.** in comparison with this model.

II.3.2.2 Electro-optical switches

There are two types of switches used in this work, both based on electro-optical, or so called Pockels-effect. A Pockels cell consists of a crystal, which is transparent to the used wavelength, with some electrodes attached to it. When a voltage is applied to the crystal it causes a change of refractive index between the slow and fast axes and hence can be regarded as a voltage-controlled waveplate. The electric field can be applied in the direction of the light beam, which passes through holes in the electrodes. Large apertures are possible, but switching speed is often limited. Transverse devices have the electric field perpendicular to the propagation of the light. The material is usually a non-linear crystal, such as KTP, BBO, KD*P, LiNbO₃ Pockels-cells are usually characterized by their half-wave voltage V/π , which is the voltage required for inducing a phase change of π , equivalent of a $\lambda/2$ waveplate. This is the voltage applied in regenerative amplifiers or in the gating cell to cut the steady-state part of the train in our case. The half-wave voltage of a Pockels cell depends on the crystal material, the electrode separation, and hence crystal size, and the length of the region where the electric field is applied. A balance has to be found between speed of the device and the aperture size required to avoid damage. Matching of driver to the cell is advantageous as each cell has slightly different impedance and is also prone to elasto-optic effects. Depending on the switching function required, cells together with the drivers have to be carefully tuned to avoid piezo-ringing.

The demand for high bandwidth switches for telecommunication has promoted the advance of fast fiber-optic modulators with reliable long-term stable operation^{II.46}. Polarization switches based on gallium arsenide (GaAs), used in the same way as Pockels cells, are now available on the market with 40GHz bandwidth, but are limited to the telecommunications wavelength of 1.5 μm ^{II.47}. Lithium niobate (LiNbO₃) fiber-optic modulators have been developed at 1 μm wavelength for amplitude modulation, and offer a high extinction ratio of 40dB^{II.48}. The waveguide-based Mach-Zehnder interferometer consists of a Y split, where the polarized optical input signal is split into two equal components. One arm contains the electro-optic crystal (LiNbO₃), where a phase-shift can be introduced by applying a voltage across the crystal. The two arms are then recombined and, depending on the relative phase between the 2 arms either interfere constructively or destructively, giving an output signal which is

\sin^2 -dependent on the applied voltage^{11.49}. Another approach is to use an electro-optic phase shifter in one arm of a Mach–Zehnder interferometer and use constructive or destructive interference for amplitude modulation or switching. The modulator usually requires a bias voltage to set its operational point and an RF signal, which provides the transfer function for the modulator. When the bias is set for operation at the QUAD working point (see Fig.II.3.1.), in the case of no RF input the modulator transmits 50% of the signal (not including losses on the connectors). When RF input at \pm the half wave voltage is applied, a high extinction ratio signal is provided with the imprint of the RF pulses.

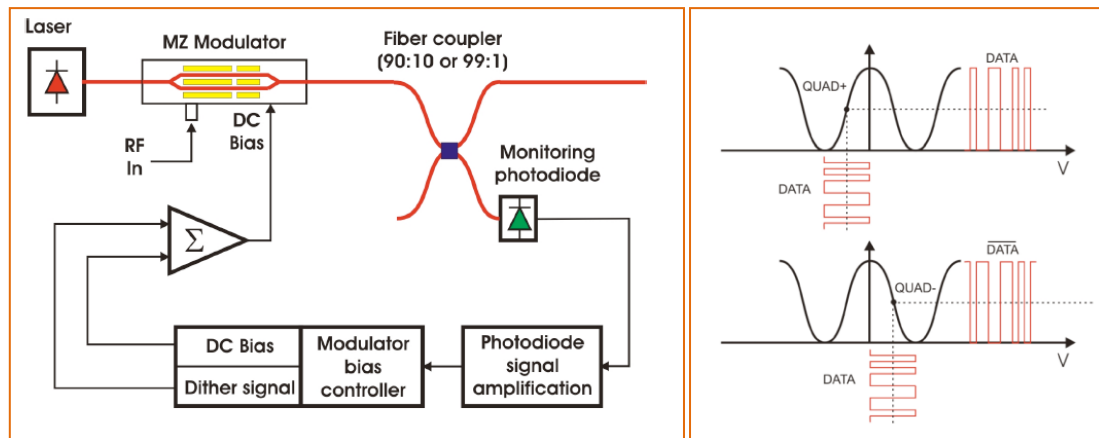


Fig.II.3.1. A typical arrangement for pulse structuring using a Mach-Zehnder modulator based EO switch. Operation at the QUAD working point is shown on the right. (Photline Ltd.)

While crystal based Pockels-cells typically require a few kV drive voltage, depending on the geometry and the wavelength, the systems mentioned above and based on fibres, due to their small cross-section only require a half wave voltage of $\sim 5V$. In our case these devices were either used to select a train of pulses at the required length or used as part of a feedback loop to keep the output energy of the laser constant. Due to the use of the fibre the average and peak power are limited. **Chapter III.4.** Of this work is directed towards selecting the right device for the phase-coding setup and building a suitable system.

II.3.3 Stability and reliability

The stability of a photo-injector is mainly dependent upon the stability of the drive laser. Other factors, like degradation of the photo-cathode and vacuum conditions can be controlled to some extent and are not within the scope of this thesis. There are many parameters affecting stability, not all of which could be investigated during this work. A summary of possible noise sources is given in Table II.3.4. Often the three types of noise are interconnected, causing a net effect on the electron beam stability.

Table II.3.4. Possible noise sources of the system

Amplitude	Pointing	Timing
<ul style="list-style-type: none"> • Electrical noise/power supplier noise • Pumping diodes • Seed source (osc+preamp) • Phase coding • Pointing (amplification + harmonic stages) • Thermal drifts • Mechanical vibration 	<ul style="list-style-type: none"> • Water cooling system • Air conditioning (temperature variation+ airflow) • Vibration • Airflow in beam transport • Lack of relay imaging 	<ul style="list-style-type: none"> • Thermal drifts • Pointing

The main parameter tolerances are listed below in Table II.3.5.

Table II.3.5. Parameter tolerances for the PI laser system

Parameter	Required typically
Pulse rise time (10-90%)	1 ps
Laser to RF phase stability	<0.5 ps rms
Homogeneity on the cathode	10% ptp
Pulse-to pulse optical energy jitter (macropulse)	<0.5% rms
Spot diameter jitter on the cathode	1% ptp
Pointing stability	<1% ptp

The environmental conditions, such as temperature and humidity changes, electrical noise, and vibration will all have an effect on the laser stability and hence the work has to start with passive stabilization. Moreover all parameters are interlinked, where pointing and beam size instabilities can lead to amplitude instabilities. Timing jitter leads to further increase of amplitude instabilities for the delivered electrons. Stabilization has to be done with all parameters in mind.

Why stability is important and what can affect it is discussed in the following sections. Apart from delivering the parameters, long, reliable operation and automatization of the system is also necessary. Laser protection with interlocks linked to diagnostics on the system are also part of this, by making sure errors in one sub-system do not cause damage to other parts of the laser and failures can

be identified quickly. These diagnostics also provide an online monitoring of the system for noise characterization and for identification of noise and drift sources.

II.3.3.1 Timing stability and synchronization

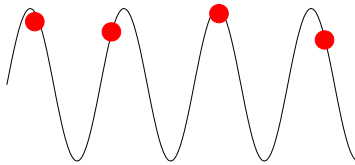


Fig. II.3.2. Laser to RF phase stability

The master oscillator repetition frequency has to be a sub-harmonic of the RF signal. Because the acceleration is by a high gradient RF field any phase change at the gun affects the energy slew through the bunch (Fig.II.3.2.). This then affects the compression and the arrival time to the next LINAC

in cases of FEL's. The bunch length and the produced current are inversely proportional, which means that the net effect can lead to serious degradation of the performance. Therefore, for these machines the tolerances are much tighter, reaching to below the 30fs regime. For the CTF3 machine this effect starts to be significant at 1 ps rms jitter. Most of this jitter comes from the seed oscillator, so active feedback is needed to control the cavity length by comparing the oscillator's output phase with the RF phase. Standard phase-locked loops are available with the laser oscillators. Apart from the mechanical stabilities of the laser the electronics driving the feedback can also affect the performance and the best values commercially achieved are ~150fs rms jitter 1-100MHz. A summary of the performance between different pump sources and repetition rates can be found in ref. II.50. However, the demand for improving timing distribution of the RF signal parallel with high performance fibre telecommunication links has triggered the use of fibre oscillator based RF reference links^{II.51}. This has opened the possibility to optically synchronize the laser to the reference by optical cross-correlation techniques. Due to the lack of available fibre reference source this technique has not been used at CERN yet.

Specification for pulse duration change is the same as it is for the timing jitter. Depending on the optical elements used in the laser system this effect can be negligible. During the amplification due to gain narrowing the pulse gets stretched. This effect depends on the properties of the material and the level of the gain. If the amplifier is stable, then the change will be small. There can be other elements having influence on the pulse shape, such as harmonic generation crystals and phase masks for homogenisation of the beam profile. It is preferable to use the harmonic generation crystals in the saturated region for better beam quality and stability. The pulse length changes with the level of the saturation, so instability of the input will cause pulse length changes. However this effect is only significant with fs pulses.

II.3.3.2 Amplitude stability

The requirements for the optical energy stability are very tight. Less than 0.1% rms stability should be provided on the photo-cathode for CLIC. This is difficult task, as 0.1% rms means ~0.025% rms in the fundamental, if forth harmonic is required on the photo-cathode. Table II.3.6. summarizes the effect of 1% energy jitter on the parameters of the electron beam.

Several aspects of the system affect the pulse the pulse stability:

Table II.3.6. Parameter variation of the electron beam with laser amplitude jitter

Variation of parameters with $\pm 1\%$ laser energy jitter	
Charge variation	$\pm 1\%$
Transverse Normalized Emittance	$\pm 0.6\%$
Longitudinal Normalized Emittance	$\pm 0.8\%$
Energy Spread	$\pm 0.9\%$
Bunch Length	$\pm 0.3\%$

- The stability of the laser diode power supply directly determines the stability of the output.
- Depending on the level of saturation in the amplifier(s) variations of the seed laser can have a large or small effect on the output.
- High voltage switches, driving Pockels-cells in the system can introduce noise, piezo-ringing over the train length.
- Thermal effects in the harmonics crystals can cause variation even on the timescale of the pulse trains.
- Other electrical noise from the high voltage supplies can affect detection system used for feedback stabilization.
- The oscillator itself can exhibit noise related to relaxation oscillations or the type of mode-locking used.

The advantages of the steady-state operation and at high saturation will be **discussed later in III.1.3.5**. The Fourier analysis of the noise can often give good indication of the sources of the noise^{II.52}.

Long term amplitude variation with $>1s$ period are generally due to thermal effects, which eventually cause misalignment in multipass amplifier systems as well as change in pumping profile. This will lead to the variation of the gain and will affect the output power. These slow drifts can be easily compensated with a feedback stabilization system monitoring shot-to-shot variations (techniques **listed in II.3.3.4**). Discrete spectral lines in the noise spectrum at 50Hz or at the 10-100 kHz region can be associated with switching power supplies (diodes, Pockels-cell etc.). In the region below 1 kHz noise originates from mechanical vibrations. Sources of faster noise can be caused by relaxation oscillations from the laser oscillator and are typically around 50-600 kHz and appear as a broad continuous peak in frequency domain measurements. Any vibration induced noise around the spectral line of the relaxation oscillation will cause large oscillations of the output power and so the system has to be designed for good mechanical stability. As the system is passively mode-locked with a Semiconductor Saturable Absorber (SESAM) higher frequency noise can appear in the 100MHz regions due to Q-switching instabilities. These can be avoided by good design of the system but can appear due to damage, degradation or misalignment of the optics in a well-designed system too.

As the amplifiers are running in saturated-steady state mode, noise can be damped depending on the saturation level of the amplifier system. As the fluorescence lifetime is $480\mu s$ for the Nd:YLF

- Temperature of the pumping diodes effects the wavelength of them, which then changes the absorption into the crystal and so the maximum energy that can be extracted.

- The temperature of the crystal and airflow and change the optical path, which can have a significant effect in a case of a multiple-pass amplifier system.

amplifiers used in the particular case, significant attenuation of noise due to gain saturation will only happen <1 kHz region. The harmonics stages both work at slight saturation, but as the wavelength conversion is a non-linear process with a quadratic dependence, it will be the major contribution to the increase of the noise from IR to UV output.

II.3.3.3 Pointing stability/ beam transport

The emittance will change by 0.3%, when optimized beam size is changing by 1%. Although specifications were not given for either beam size or beam position on the cathode, these parameters should be monitored and controlled with high accuracy.

A good design of the optical system can already help with the pointing stability and as a result with amplitude stability. Relay imaging the oscillator cavity to the amplifier crystals and to following subsystems will ensure, that the thermal drift induced changes will have the least effect on the output performance. Beam transport systems for photo-injectors can be over 10's of meters long due to the radiation level and the accelerator associated hardware. Good isolation of the beam from airflow is important and vacuum transport is considered, when the UV beam is used. Active stabilization is possible via a beam position measurement usually performed with a quadrant photodiode and correction by a pair of piezo-controlled mirrors. Flexibility is required for beam size adjustment, especially for FEL injectors, where emittance tuning is necessary, imaging a hard aperture with different sizes nearer to the cathode is a good solution. However this requires ample margin in the available energy, so losses can be compensated for. As laser room was planned to be near the cathode and Gaussian beams were requested in the CTF3 case, a simple image relay system with one moveable lens for beam size adjustment was implemented. Part of the beam transported in the machine is in vacuum tubes to avoid losses.

II.3.3.4 Active amplitude stabilization techniques

Most amplitude stabilization techniques are based on a detector, which measures the amplitude (i.e. a photodiode producing a measurable photo-current) an instrument on which the feedback can act, affecting the output and a feedback circuit, as seen on Fig.II.3.3. The nature and the source of the noise determine the resolution and speed required from the sub-systems. In the PI laser some solutions were implemented based on either control of the pump current of the diodes or flashlamps, or by stabilizing the output independently from the amplification stages, using EO switches (Pockels-cells)^{II.36II.37,II.40}.

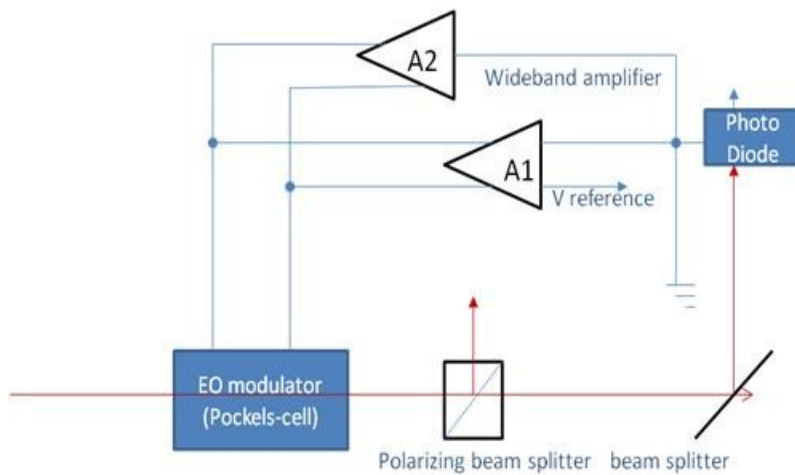


Fig. II.3.3.: Pockels-cell based feedback stabilization scheme

For slower drift compensation with a simple waveplate polarizer attenuator - limited by the speed the waveplate can be moved at - is sufficient. Typically 1% rms stability on the cathode was achieved using one or a combination of these systems. In the case of the CTF3 laser the situation is further complicated by the fact, that

although laser works in steady-state and provides flat-top train in the IR, due to the high 1.5GHz repetition rate, absorption losses in the 4th harmonic crystal can cause changes along the train length, by earlier pulses having an effect on the following ones. This often causes not just amplitude, but also transverse laser beam profile variations. Further constraints to the stabilization during the pulse train in the case of the CTF3 laser are listed below:

- Pockels cells are in UV are usually based on non-linear crystals, here the two-photon absorption would be considerable given the small aperture size needed for the required switching speed. Thus control in the UV therefore is not advisable.
- The laser is operating in burst mode at all stages after the preamplifier with very short burst lengths after the Pockels-cell and at the harmonics stages. This requires a fast response time from the feedback system, as some of the noise from the frontend (oscillator and preamplifier), will appear as a level shift between macropulses.
- A stabilization system could be installed at the preamplifier stage to regulate low frequency modulation (LFM) level shift; however any changes and noise due to the amplification process in AMP1 and AMP2 and in the harmonics stages will not be compensated for. Moreover during the conversion process the amplitude variations increase due to the non-linear conversion process and so even tighter specifications are required for the feedback system at the preamplifier stage.
- If the feedback system is installed before the second harmonic generation stage, then it must be able to regulate both low frequency modulations from the oscillator and preamplifier as well as level shift from the AMP1 and AMP2 stages. However at this stage of the system the laser is already in burst mode and so compensation has to be very fast. The system would also need to be able to handle the high power loads.
- Fast noise observed from oscillator and preamplifier cannot be compensated with a conventional feedback system. The option of the feed forward system is very challenging, as the optical delay will have to be set accurately to match the speed of the electronics.

II.4 Generation of UV and losses

Working with short wavelengths limits the number of materials can be used, because the absorption band of many materials falls into this region. At high intensities not just the linear absorption will cause losses, but the nonlinear, two-photon absorption, as well. As mentioned earlier the most efficiently pumped sources are working in the IR region, so generation of the desired UV wavelengths only can be done by parametric processes. By using nonlinear optical crystals the shortest possible wavelength achievable to date is 166 nm^{1,22}. At these short wavelengths both linear and nonlinear absorption will have a main role in losses and temperature detuning of the phase-matching angle^{1,23} and in optical damage. Two-photon absorption induced losses also can limit the achievable gain from these systems, especially if the pump wavelength is in the UV, as both the parametric process and the absorption will depend quadratically from the laser intensity. The basic description of the non-linear interactions and those processes relevant to the thesis, second harmonic generation, parametric amplification, two-photon absorption and its measurement techniques are described in the following sections.

II.4.1 Non-linear processes

When the electric field of the light is applied to a dielectric medium the negative charge (valence electron) together with the positively charged parent will create an oscillating dipole, which follows the frequency of the external field in the case of linear optics, creating an overall polarization response. At low intensities this response is linear and is related to the external field through the linear susceptibility of the material. In terms of wave equations it can be described as¹³:

$$\nabla \times \nabla \times \mathbf{E} - \frac{1}{c^2} \frac{\partial^2 \mathbf{E}}{\partial t^2} = \frac{-1}{\epsilon_0 c^2} \frac{\partial^2 \mathbf{P}_l}{\partial t^2}, \quad \text{II.31}$$

where \mathbf{P}_l is the polarization vector:

$$\mathbf{P}_l(\omega) = \epsilon_0 \overline{\chi}^{(1)}(\omega) \mathbf{E}(\omega), \quad \text{II.32}$$

where ϵ_0 , is the electric permittivity of free space. χ is the Fourier-transform of the dielectric response tensor of the material, called susceptibility tensor. It has nine components in the Cartesian coordinate system and in an isotropic medium only contains one non-zero component. The shape of this component with respect to frequency characterizes the dispersion properties of the material.

This analogy can be followed from linear optics into the non-linear regime. When the field becomes sufficiently high the dipoles can no longer follow the oscillations of the external field and new frequencies will appear which can be described as an additional non-linear polarization vector. This way in eq. II.31. the \mathbf{P}_l can be exchanged with the sum of linear and non-linear polarizations:

$$\mathbf{P} = \mathbf{P}_l + \mathbf{P}_{nl}. \quad \text{II.33}$$

¹³ No magnetic dipoles, no electric conductivity or static charge is taken into account. For homogeneous media $\nabla \times \nabla \times \mathbf{E} \approx -\nabla^2 \mathbf{E}$.

\mathbf{P}_{nl} in the case of higher fields can be represented by its Taylor-expansion, where new waves are generated:

$$\mathbf{P}_{nl} = \varepsilon_0 \left(\chi^{(2)} \mathbf{E}\mathbf{E} + \chi^{(3)} \mathbf{E}\mathbf{E}\mathbf{E} + \dots \right). \quad \text{II.34}$$

This way using the macroscopic Maxwell-equations non-linear optics can be treated under the electro-magnetic phenomenon^{11.55}. This time nonlinear polarization introduces inhomogeneous differential equations. Propagation and related nonlinear coefficients can be defined through field-independent and local-field-induced nonlinear optical susceptibilities. As intense laser pulses induce such non-linear effects in most cases the electric field in II.34. is described as the sum of discrete frequency waves (see II.2.1.). Eq. II.34. can contain a combination of different frequencies and hence the non-linear polarization will also consist of different terms representing oscillation frequencies as a result of the sum of two or more frequencies that contained by the external light field. Negative frequencies will be taken into account as the complex conjugate of the field of the corresponding positive frequency.

When propagating through an anisotropic dielectric media the electric vector will not longer be necessarily perpendicular to the direction of the propagation. A displacement vector is then defined as: which is perpendicular to the propagation vector \mathbf{k} . In second order optics the susceptibility is often marked with the effective non-linearity, where tensor d is:

$$d_{ijk} = \chi^{(2)}_{ijk} / 2, \quad \text{II.35}$$

with the convention to replace letters by numbers i.e. $d_{xyz} = d_{xzy} = d_{14}$ and so the tensor will be a form of a 3X6 matrix. If there are no resonances at the given frequencies, then all susceptibilities will be real values.

II.4.1.1 Frequency conversion

Second order non-linear processes allow for the conversion of the frequency of the high intensity light incident upon materials with large non-linear susceptibilities and generate coherent

$$\mathbf{D}(\omega) = \varepsilon_0 \mathbf{E}(\omega) + \mathbf{P}(\omega) = \varepsilon_0 \boldsymbol{\varepsilon}_r \mathbf{E}(\omega), \quad \text{II.36}$$

radiation at wavelengths, which are otherwise difficult to produce or amplify. The three basic processes applied to convert the frequency for a given laser are Second Harmonic Generation (SHG), Sum Frequency Generation (SFG) and Difference Frequency Generation (DFG). In the first case one single pump wave generates its own second harmonic wave, while in the case of SFG and DFG two pump waves generate a new frequency.

All these processes are phase sensitive. To calculate the overall contribution and phase-relationship along the crystal, the wave vector \mathbf{k}^{14} of all the beams are taken. Different portions of the

¹⁴ The magnitude of the wave vector is the wavenumber, which is inversely proportional to the wavelength. The direction of the vector is normal to the surfaces of constant phase. In the case of isotropic media they coincide with the propagation of the wave and the energy (Poynting-vector).

material contribute to the overall amplitude of the produced signal at the exit. As the pump and the produced waves are usually not propagating with the proper phase-velocity relation the energy transfer changes direction many times during the propagation through the crystal, as the phase relation changes. This means, that the interaction length is reduced and only very weak signal is produced at the new frequency. When phase matching (PM) is achieved the contributions along the crystal add up constructively. In the case of SHG this would imply, that the fundamental and two second harmonic waves would be perfectly phase matched $k_{2\omega} = 2 \cdot k_{\omega}$ while for SFG $k_{\omega_3} = k_{\omega_1} + k_{\omega_2}$.

In an anisotropic media the dielectric tensor (containing the relative dielectric constants) is symmetric and hence can be described in an orthogonal coordinate system, where the tensor is diagonal. The axes of this coordinate system will be the principal axes of the material and the medium is called biaxial. In the special case, when two of the principal axes align the media is called uniaxial. In both case the crystal has birefringence or sometimes called double refraction properties. Most of the crystals used for frequency conversion are anisotropic uniaxial crystals of this kind. There will be two refractive indices assigned to the two polarizations, one which is parallel to the optical axis (symmetry axis of the crystal) and is called ordinary wave and one, which is perpendicular to it and called extraordinary. This property can be used to achieve PM conditions as chromatic dispersion will be different along the principal axes. There could be many conditions when PM is satisfied. Type I phase-matching is considered when relative to the crystals optical axis only one polarization is pumping to achieve new frequency wave, while in Type II PM both ordinary and extraordinary components contribute the generation of the new signal. In biaxial crystals the phase-matching conditions are less obvious and propagation in a particular direction in respect to the optical axes has to be found, which is described by two angles. Type I and II definitions are still standing in this case.

In the case of critical phase-matching the crystals is cut and tuned in angle to obtain high efficiency. The crystal can also be temperature tuned (non-critical PM), where all polarizations are along the crystal axis. PM conditions can be maintained for longer interaction lengths by having a series of short slices of crystals (periodically poled) with subsequent opposite orientation of the axes (quasi PM).

High efficiencies up to 80% can be achieved with high intensities inside resonant cavities. In our case second harmonic generation in two stages from IR to visible and then visible to UV is of the main interest. However, when Ti:Saph lasers are used for photo-injector applications to take advantage of the broad bandwidth and hence the temporal shapability of the beam the shorter fundamental wavelength means that SHG and SFG are often used together to generate the 3rd harmonic.

In the case of SHG the non-linear polarization for both wavelengths present will be:

$$P_{2\omega}^{(2)} = 2\varepsilon_0 d_{eff} A_{\omega}^2 \exp(i\Delta kz) \quad \text{II.37}$$

$$P_{\omega}^{(2)} = 4\varepsilon_0 d_{eff} A_{2\omega} A_{\omega}^* \exp(-i\Delta kz). \quad \text{II.38}$$

And so the coupled wave-equations will take the form of:

$$\frac{dA_{2\omega}}{dz} = i \frac{2\omega}{n_{2\omega}c} d_{\text{eff}} A_{\omega}^2 \exp(i\Delta kz) \quad \text{II.39)}$$

$$\frac{dA_{\omega}}{dz} = i \frac{2\omega}{n_{\omega}c} d_{\text{eff}} A_{2\omega} A_{\omega}^* \exp(-i\Delta kz), \quad \text{II.40)}$$

where A is the slowly varying complex field amplitude, d_{eff} is derived from eq. II. 36. with the corresponding tensor components and Δk represents the phase velocity difference between the two waves. The intensity is proportional to the square of the real part of A . Let's take an infinite plane wave approximation, which is valid for our case. The solution of the wave-equations which can be found in reference II.55 (chapter 2) will give the following parameter for efficiency η :

$$\eta_{2\omega} = \tanh^2(L / L_{nl}) \quad \text{II.41)}$$

$$L_{nl} = \frac{1}{4\pi d_{\text{eff}}} \sqrt{\frac{2\varepsilon_0 n_{\omega}^2 n_{2\omega} c \lambda_{\omega}^2}{I_{\omega}(0)}} = \frac{1}{\gamma \sqrt{I_{\omega}(0)}}, \quad \text{II.42)}$$

where n is refractive index of the material at the given index frequency and is directly related to the real part of the linear susceptibility of the material. For infinite plane wave approximation with no pump depletion the maximum efficiency will be given by $\gamma^2 I_{\omega}(0) L^2$, where L is the length of the crystal. In the case of perfectly phase-matched SHG with the depletion of the pump becoming significant, L_{nl} would produce a conversion efficiency of ~60%.

There are some important parameters to consider during SHG as the laser will have a finite bandwidth and specific properties in space and time. Gaussian beams have natural divergence and small beams are often required to create higher intensities to increase efficiency, which will further enhance divergence. When the divergence of the beam is comparable to the angular bandwidth of the crystal this effect becomes significant. Since perfect phase-matching can only be satisfied for a certain frequency it is useful to define the phase-matching BW^{II.56} of the crystal, where efficiency is reduced to half:

$$\Delta k_{BW} \approx 2.784 / L. \quad \text{II.43)}$$

The propagation of the extraordinary wave and the energy (Poynting vector) is not in the same direction in most cases. Hence the ordinary and extraordinary waves, as they have a finite size in space will 'walk off' each other along the crystal at some crystal length become separated (aperture length L_a). The angle inside the crystal between the two orthogonal polarization beams can be calculated from the cut of the crystal and the corresponding refractive indices. At the same time the size of the beam can change considerably as it propagates over the length of the crystal. The spectral bandwidth of the crystal combined with the given geometry will determine the shortest pulses achievable after conversion and could be very significant for sub-ps conversion. Moreover, when short pulses are used the group velocity mismatch will cause the pulses become separated in the propagation direction after some length of the crystal. L_{nl} defined earlier has to be modified by a factor between the pulse length and the critical interaction time. This effect is even more severe in the case

of UV generation, as we are approaching the absorption band of the materials and dispersion becomes more significant. Furthermore linear and non-linear absorption could cause considerable losses, especially at UV wavelengths where it would also heat in the crystal, which in turn creates temperature gradients and changes the phase-matching conditions. Gradients are usually difficult to compensate for in large crystals used for relatively low intensity input beams. Temperature acceptance of the crystal is hence important for UV generation. **In II.4.3.** I will take a look of the available non-linear crystals for UV conversion and compare their performance keeping in mind the requirements for CTF3 drive beam injector.

II.4.1.2 Parametric amplification in the UV

In the case of DFG the lower input frequency wave cannot just be depleted but also amplified. The photons of the higher frequency wave (pump) contribute to the amplification of the so called signal a lower frequency, while creating a second lower frequency signal called idler. In this case coupled wave equations, similar to those described in eq. II.39-40. are applied, but this time for the three corresponding waves and I being the pump intensity. When no initial signal is present the process is called parametric fluorescence and is essentially created from quantum noise at the frequencies which satisfy conservation of energy and phase-matching at the same time. An important parameter of the parametric amplifier is its gain bandwidth, which in high gain regime depends on the gain itself. Materials with low dispersion can provide large bandwidths. Gain will be proportional to the square of the γ parameter defined in eq. II.42. $G \sim \gamma^2 L^2$.

There are two main points to mention here. Regarding the contrast parametric amplifiers will offer a great way to enhance contrast as gain will only be present, when the pump is present and earlier or later rouge pulses/pedestal will not be amplified. For this purpose CPA used in conjunction with parametric amplification, when the signal pulse length is matched to the pump could provide high contrast and avoid nonlinear effects and damage. Moreover the phase of the signal pulse is preserved through amplification and thus it is possible to amplify few cycle pulses with this technique with the CEP (zeroth order term in eq. II.14.) kept stable.

II.4.1.3 Two-photon absorption

During TPA two photons from the incident radiation field are absorbed simultaneously and there is an electron transition from the ground state up to the excited state (see Fig. II.4.1.). In our case (a) the two photons are provided by the same optical field, which is also called single-beam TPA. At higher intensities there are more photons and the probability of absorption of two photons in the same time increases. In the scope of this work TPA is an undesired effect, however there are several applications based upon it. In 1967 materials have been found, which became transparent in the case of high fluence incident pulses. In 1968 the opposite behaviour was observed in a Q-switching material, the absorbance was increased with the intensity^{II.57}.

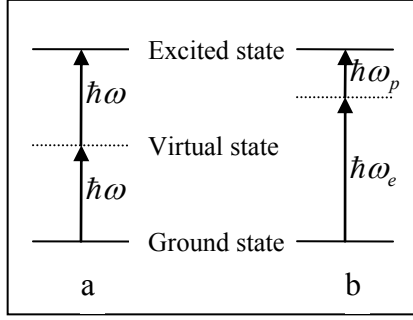


Fig.II.4.1.: Transition schematic of (a) self-TPA, (b) pump-probe TPA

These types of materials can be used as passive limiters in high power laser systems. If one is prepared to sacrifice the output power for higher stability, than TPA is shown to be a good passive tool. Cao and Warren demonstrated 76% noise reduction with 40% overall efficiency.^{II.58-II.59} Another recently developed application for TPA uses the fact that IR radiation penetrates deep into the material and TPA will only have effect in the vicinity of the focus, so polymerisation can be achieved in small scale and in three dimensions.

The intensity variation along the propagation direction due to absorption is described in the following differential equation^{II.55,ch9.}:

$$\frac{dI}{dz} = -\alpha \cdot I - \beta \cdot I^2 \quad \text{II.44)}$$

Where α : linear absorption coefficient, β : nonlinear absorption coefficient, I : instantaneous intensity and z : direction of propagation. β is related to the third order susceptibility, the imaginary part of which will determine the strength of the nonlinear absorption as described below.

Referring to eq.II.35. the propagation equation for a monochromatic field at frequency ω_p in a medium with third order susceptibility $\chi^{(3)}(\omega; \omega, -\omega, \omega)$ is:

$$\frac{dE_p}{dz} = i \frac{\omega_p}{4n_p c} \chi^{(3)}(\omega; \omega, -\omega, \omega) |E_p|^2 E_p. \quad \text{II.45)}$$

By separating the real and imaginary parts:

$$\chi^{(3)}(\omega; \omega, -\omega, \omega) = \chi_r^{(3)} + i\chi_i^{(3)}, \quad \text{II.46)}$$

we have:

$$\frac{dE_p}{dz} = i \frac{\omega_p}{4n_p c} (\chi_r^{(3)} + i\chi_i^{(3)}) |E_p|^2 E_p. \quad \text{II.47)}$$

If the phase is included:

$$E_p(z) = |E_p(z)| e^{i\phi(z)}, \quad \text{II.48)}$$

so the propagation equation becomes:

$$\frac{d|E_p|}{dz} + i|E_p| \frac{d\phi}{dz} = \frac{\omega_p}{4n_p c} (i\chi_r^{(3)} |E_p|^3 - \chi_i^{(3)} |E_p|^3). \quad \text{II.49)}$$

This propagation equation can be separated into two parts, one for amplitude and one for phase:

$$\frac{d|E_p|}{dz} = -\frac{\omega_p}{4n_p c} \chi_i^{(3)} |E_p|^3 \quad \text{II.50)}$$

$$\frac{d\phi}{dz} = \frac{\omega_p}{4n_p c} \chi_r^{(3)} |E_p|^2 \quad \text{II.51)}$$

This, $\chi_r^{(3)}$ leads to nonlinear refraction, while $\chi_i^{(3)}$ leads to nonlinear absorption. Multiplying the equation for nonlinear absorption by $|E_p|$:

$$|E_p| \frac{d|E_p|}{dz} = -\frac{\omega_p}{4n_p c} \chi_i^{(3)} |E_p|^4 = 2 \frac{d|E_p|^2}{dz}. \quad \text{II.52)}$$

Since

$$I_p = \frac{n_p \epsilon_0 c}{2} |E_p|^2 \quad \text{II.53)}$$

we can write:

$$\begin{aligned} \frac{dI_p}{dz} &= -\frac{\omega_p}{2n_p^2 c^2 \epsilon_0} \chi_i^{(3)} I_p^2 \\ \Rightarrow \frac{dI_p}{dz} &= -\beta I_p^2. \end{aligned} \quad \text{II.54)}$$

This leads us back to eq. II.44. with the physical parameters determining β .

By substituting eq II.52. in the wave equations and solving them numerically one can accurately calculate the TPA effect on harmonic generation and optical parametric amplification. The method of determining the effective intensity is by “slicing” up the crystal into small elements, and calculating the product of gain and conversion for each element, with the intensity attenuated by the TPA from one slice to the next. Calculations, not detailed here show; that the reduction of the amplification bandwidth is less critical with increasing crystal length, however reducing the peak intensity of the pump seems play a key role.

Although the phenomenon of nonlinear absorption is a well-known, the two-photon absorption coefficients for nonlinear crystals at the above-mentioned UV wavelengths are not yet available in the literature or they are not consistent. Recently the level of TPA has been found to be polarization dependent and to be function of the crystal cut, too.

Experiments carried out on the ASTRA laser system in the UK^{1,26} have shown that the TPA at the pump wavelength of 267 nm reduces the achievable gain for the 400 nm sub-50 fs signal pulses. We have shown this in theory and compared several nonlinear crystals and their performance as parametric amplifiers in this wavelength range. The most promising crystals for NOPA technique using pump pulses at 248 nm and 212 nm are β -BaB₂O₄ (BBO), CsLiB₆O₁₀ (CLBO) and Li₂B₄O₇ (LTB).

Since the TPA and the nonlinear conversion processes show different dependence on the crystal length and intensity, in order to find the optimum parameters, it is essential to know the values of the TPA coefficients. So far, measurements have been carried out for nonlinear crystals at the

wavelengths of 267-264 nm, and 216 - 211 nm and only for BBO and KH_2PO_4 (KDP) crystals^{II.60II.61II.62II.63II.64II.65} For CLBO, only estimation has been mentioned in the literature.^{II.55}

Since the available focused power of table-top solid-state laser systems rapidly increases and approaches 10^{20} W/cm², more information is required about the TPA coefficients of these nonlinear crystals. In **chapter III.4**, I report measurements, which were carried out on different nonlinear frequency converter crystals to determine their nonlinear absorption coefficient (TPA) in order to predict the losses in multicolour laser-systems.

4. My aim was to measure the nonlinear absorption of different nonlinear crystals by making transmission measurements with a KrF laser at 248 nm. First measured two photon absorption coefficients at this spectral region for CLBO and LTB.

II.4.2 Measurement techniques for two photon absorption

The value, which is interesting in the measurement, is the transmittance of the material under different conditions. As TPA is intensity dependent process and large variations of the transmission makes the measurement more reliable, the choice can be made to either vary the beam size or the laser energy. Thin samples can offer a high sensitivity and are suitable for Z-scan measurement methods; however there is a danger of surface damage and self-focusing. We also should be careful with the pulse length, as longer pulses reach the peak intensity at higher energies. In the Z-scan method the laser is focused down with a short focal length optic and the beam size is characterized along the waist, where the short sample is then placed. However, if long (several mm) materials are available and the laser beam is energetic enough to be kept collimated within the long crystal providing high intensity at the input, the direct measurement of transmission as a function of the input intensity seems a more straightforward method. With thick samples, measurements must be taken to insure, that the laser beam is reasonably collimated along the crystal, and measurements of the incident and transmitted energy are taken on the same shot. In this measurement system the incident energy should be variable and the beam parameters such as pulse length and shape, beam size should be correctly measured or kept constant as much as possible.

II.4.3 Available non-linear materials and their properties

When high average power, harmonic generation or amplification is considered in the UV regime the following contributions from different parameters have to be taken into account:

- Temperature gradients created by absorption induced heat mainly depend on the generated UV profile (SHG).
- With Gaussian profiles the center part of the beam containing higher relative intensity will result in higher absorption and hence more heat. Flat top beams are desirable, if short crystals are used.
- This heat causes thermally induced phase-mismatch, which should not be mistaken with real saturation. Analysis of the input and output beam profile can give a good indication of the severity and presence of absorption. For example a hole in the middle of the beam can be observed when high intensities are used in crystals with low temperature acceptance or in the NCPM case.

- For full characterization of the thermal gradients thermal conductivity and surface heat transfer coefficient^{II.66} has to be known for the crystal. These values are not always available for full model.
- TPA will create gradients twice of that of linear absorption and the longer the crystal the higher the gradient during SHG as UV intensity increases.
- When shorter crystals are used one has to compromise on the conversion efficiency.
- Multiple crystals with the same total length can give better performance^{II.67}.
- PID control (proportional-integral-derivative), which introduces a negative spatial profile to pre-compensate for gradients^{II.68} can also help e.g. by cooling with gas jet on the front surface, but turbulence can affect stability and the nozzle has to be designed to match the beam size.

Table II.4.1. The most used crystals for 4th harmonic generation of 1047nm and selected parameters for comparison

Crystal/parameter	KDP	BBO	CLBO	LTB (LB4)	ADP
Type	I	I	I	I	I
θ/cut phase-matching angle (deg)	481/45	48.8	63.4/45	66.9	Non-critical at 293.5K
d_{eff} (pm/V) Effective nonlinearity	0.473	1.73	8.06	0.145	0.685
γ efficiency (1/sqrt W)	8.35E-5	2.62E-4	1.44E-4	1.13E-5	?
IL² for max. effic. (GW)	0.143	0.02	0.048	7.83	
$\Delta\theta$ mrad.cm angular tolerance	1.76	0.18	0.55	0.19	215.39
Acceptance angle (deg)	3.52	0.37	1.11	0.38	430.78
Walk-off (mrad)	9.83	85.32	31.58	53.09	- 0.08
Length in cm, where the beam separate due to walk-off for 1mm beamradius	10.173	1.169	3.166	1.882	
ΔT temperature acceptance Kcm	2.41	5.79	6.41		0.5
Damage threshold (J/cm²)	15	13	25		0.0699

Table II.4.1. shows the important parameters of crystals used. Considering UV generation in BBO, both single wavelength TPA of the second harmonic and fundamental plus harmonic have significant absorption. CLBO has lower TPA than BBO and could provide a better solution. KD*P has the same TPA as BBO, but KD*P temperature acceptance is only half of the BBO's, which results in a higher gradient. KTP has 3 times the efficiency of LBO and exhibits high temperature bandwidth. However LBO has smaller absorption and better thermal conductivity, which could make it a more suitable material for high power conversion.

Numerical modeling of thermal effects in nonlinear crystals for high average power second harmonic generation is not in the scope of this thesis. Some very useful publications on modeling thermal effects can be found in ref.II.69-II.70.

II.5 Pulse structure, satellites and contrast

Fig.II.5.1. shows the unwanted pedestals and pulses around the main pulse. Depending on the fluorescence lifetime of the active materials used for amplification and the pump duration, ASE pedestals will appear at the longest timescales ~ns or longer depending on the pump duration and the

used material. As regenerative amplifiers are often used for achieving high intensities at the front-end of the system and are based on electro-optical switches with limited extinction ratio a certain level of leakage is then propagated through the system and may be further amplified. As chirped pulse amplification is necessary to achieve ultrahigh intensities, pulse compression, as the last stage of the system with its ability to compensate for higher order dispersion will also affect the resulting contrast. Limited spectral bandwidth of the optics in the system will also ultimately cause temporal distortions. The knowledge of the temporal contrast down to the dynamic range of 10^8 in the UV is a difficult task, especially because of the lack of the suitable materials for measurement. In the following sections I will discuss the different measurement techniques available for temporal characterization and contrast measurement of pulses. The different techniques for pulse cleaning are not covered in this thesis. A good summary with ample references can be found in ref. II.71 .

Contrast also plays a role in photo-injector lasers. As mentioned in II.1.4. satellites in between the mode-locked pulses will produce low charge electron bunches, which will be lost during electron beam propagation and can cause excessive radiation losses for the future CLIC accelerator. I will also have a short review in this section regarding the measurement techniques both for the laser and the electron beam to measure the level of satellites.

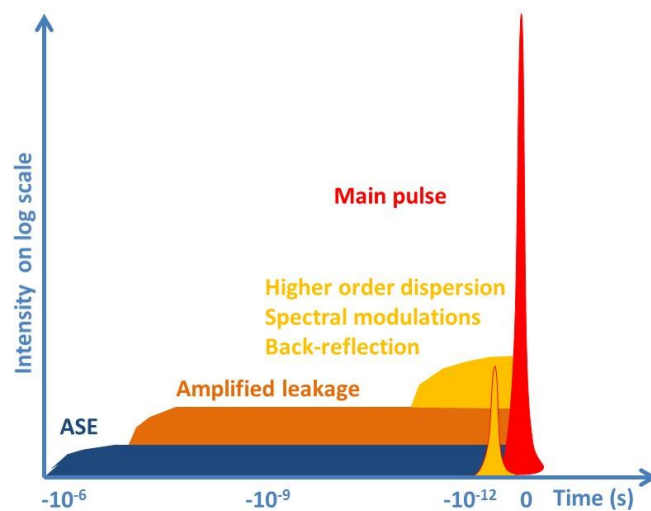


Fig II.5.1.: Typical temporal shape of an ultrashort amplified high intensity laser pulse

II.5.1 Single pulse measurement techniques

Fast photo detectors with 10s of ps resolution are now available together with high resolution digital signal analysers for pulse characterization in the ns range. However, once the pulse length reaches the ps range or below these techniques can no longer resolve the pulse shape.

Optical spectrum can be easily measured, especially for fs range pulses, as the bandwidth is sufficiently broad to be resolved by all commercial spectrum analysers. As detailed in section II.2.1.1, in the case of known phase characteristics, this spectral measurement can provide a good estimation of the pulse duration. However, when the phase is unknown spectrum on its own will not provide all the information necessary to retrieve pulse duration and distortions to the pulse shape caused by higher order dispersion. In this case direct optical measurement techniques are required. Often the whole electric profile of the pulse needs to be characterized. Apart from full characterization of the

shape of the main pulse, the ability to resolve pre-and post-pulses at low levels the dynamic range of the measurement system is also an important specification.

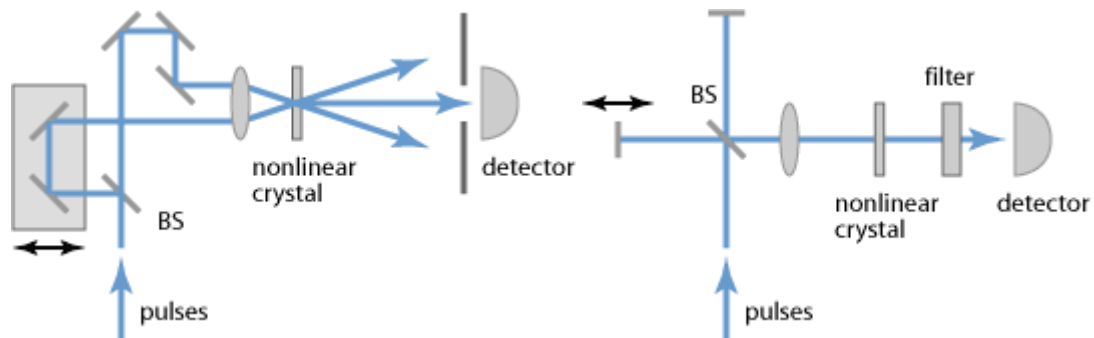


Fig II.5.2.: Intensity (left) and interferometric (right) correlator
(pictures taken from www.rp-photonics.com)

A correlator is a device comparing two signals (cross-correlator) or a signal and its replica (autocorrelator) to characterize its temporal properties. They usually consist of two arms. The correlation between the two arms is achieved by variable delay (scanning correlator) or shearing (pulse front tilt). This way timescale of the pulse can be visualized on an extended time scale or in space. The non-linear process, providing an instantaneous response to the overlapping beams will ensure the resolution. Auto-correlators split the incoming light into two parts and after delaying one arm recombine them in a non-linear crystal, two-photon fluorescence material or TPA detector¹⁵ (non-linear effects **described in section II.3.1.**) to create a time dependent signal as a function of the overlap. Cross-correlators will use a different wavelength or pulse length, which allows for enhanced resolution in the detection of the pulse-shape ((E.g. shorter pulse scanning across the measured pulse). There are many categories which by correlators can be sorted. Two examples are shown in Fig.II.5.2. If the correlation signal is only present when both arms are present the correlation is called background free^{11,72}. Depending on the duration and pulse-shape complexity different techniques are better suited. In general intensity autocorrelators¹⁶ are suitable for few ps pulses and have been employed in some measurements during the characterization of the photo-injector laser, which is subject of this thesis (Femtochrome Reas. Inc. FR-103HS). However autocorrelators carry the ambiguity that the same correlation function can belong to many different intensity distributions^{11,73} and they do not give any information about the asymmetry as the signal measured is $A_2(t) = \int_{-\infty}^{\infty} I(t)I(t - \tau)$ is symmetric around $\tau=0$ ¹⁷. They usually only have 3-4 orders of magnitude dynamic range and so their suitability for contrast measurement is also limited. For asymmetric shapes 3rd order correlators are better for distinguishing pre-and post-pulses. In some devices 3rd wavelength is generated only in the presence of both arms and hence dynamic range can be improved compared to 2nd order autocorrelators^{11,74}. This technique is the most widely used in ultrashort pulse laser systems due to its simplicity. Balanced

¹⁵ The incident pulses directly generate a **nonlinear TPA photocurrent** in the semiconductor, such as GaAs.

¹⁶ Here autocorrelators are considered to be always 2nd order devices, strictly mixing a signal with its replica. So called 3rd order autocorrelators sold on the market are coming under a category of cross-correlators in strict mathematical context. Here a second harmonic signal is mixed with the original pulse and indeed asymmetry of the pulse can be detected this way.

¹⁷ The ambiguity of different autocorrelation techniques is related to the mathematical one dimensional phase retrieval problem which is unsolvable and means that many pulseshapes can correspond to the same spectrum or autocorrelation function.

detection and lock-in amplifiers can improve the dynamic range further, subject to available repetition rate.^{II.75}

Interferometric autocorrelation produces a signal with a fast oscillation at a period of half the optical wavelength. The signal is the highest, when the two arms overlap in time and constructively interfere. The peak signal in the second order case is eight times higher than the background, giving a good indication of the alignment of the system. For shorter pulses with chirp interferometric measurement will provide better indication of higher order dispersion. A home-made interferometric autocorrelator was used in our measurements performed on the TeWaTi laser system. As higher order dispersion compensation was in our interest in order to produce the shortest possible pulses the full analysis of the correlation traces was needed. Since the work included in this thesis was done there are online Fast Fourier-transform (FFT) techniques, which are combined with interferometric measurements for exactly this purpose MOSAIC^{II.76}.

Other methods of pulse characterization, like FROG^{II.77} or SPIDER^{II.78} are more precise in the few 10's of fs regime, however the setup and the data retrieval is more complicated in these cases. Optical parametric amplifier correlators provide the highest dynamic range demonstrated up to date, with a theoretical limit of 10^{15} contrast measurement^{II.80}.

II.5.2 Pulse train measurement techniques

The single pulse energy of a macropulse is usually retrieved from the measurement of the power divided by the repetition rate. However, when satellites are present between pulses, which could be outside of the scanning range of the auto-correlator this leads to a false estimation. Conversion efficiencies usually give a good indication when such background is present in the system. As high resolution in time together with long scanning range is often required to fully characterize pulse trains, including their frequency, background or satellites pulse contents, the techniques below will give a good extension to the single pulse measurement techniques, described in the previous section.

II.5.2.1 Fast photodiodes/oscilloscopes

Fast photodiodes used together with fast oscilloscopes can provide a good measurement of the laser repetition rate. However with only 8bit resolution the ability to detect satellites between the pulses down to the specified 4% level in the case of CLIC laser is difficult; due to the PD response, which is usually followed by some oscillations. Fiber coupled photodiodes with up to 60GHz bandwidth are available for the visible and near infrared range and free space small area photodiodes with 100ps pulse response time for the UV are still useful for characterization. The best oscilloscope available in the PHIN laser laboratory at CERN was the LeCroy Serial Data Analyser SDA18000 with a bandwidth of 18 GHz. A New Focus 1024 fiber coupled diode was used, which has an impulse response of 12ps FWHM. The measurement is shown in Fig.II.5.3. The measurement resolution causes the 5.5ps pulse appearing as a roughly 35ps wide pulse (FWHM), with some post-oscillations. With the 60 Gsamples/s rate at a point is taken every 16.7 ps. This means that 4-5 points are recorded during one pulse. The

interval accuracy is 3.3ps. (The trigger jitter is specified to be 2.5ps RMS.) As mentioned earlier the jitter of the laser is about 0.5 ps RMS to the reference of 1.5GHz. This means, that the delay cannot be directly measured accurately between two consecutive pulses. This can be solved by saving a trace and post processing.

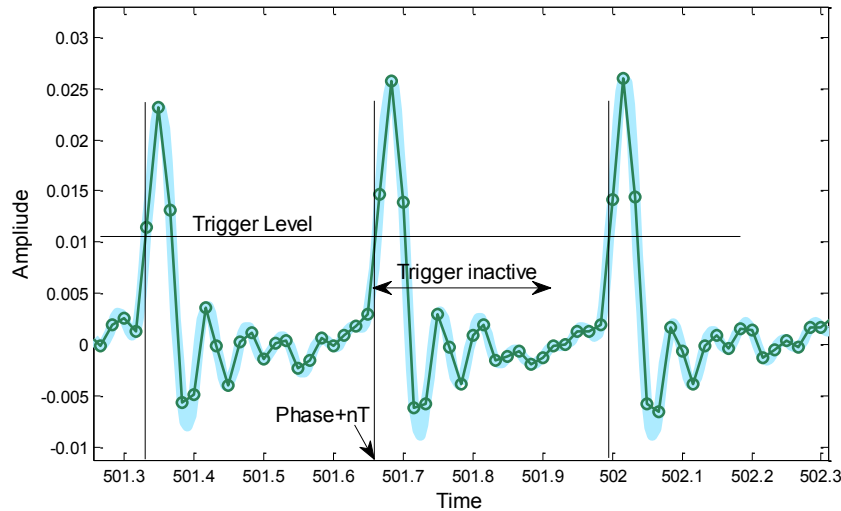


Fig.II.5.3. An oscilloscope trace and four times $\sin(x)/x$ interpolation

The combination of these devices proved to be a good indicator of e.g. bias error in our phase-coding system. Moreover slower detectors are very useful for average output power and gain monitoring of the system.

II.5.2.2 Streak camera

Streak cameras serve a very similar purpose as the oscilloscope based measurements, but with much higher temporal resolution (Hamamatsu now offers models with down to 200fs resolution). They are also able to detect single photon events and hence can often be found in accelerator instrumentation for detecting secondary light produced by particle beams. It can also reach down to very high 100keV photon energy range.

In an optoelectric streak camera the pulses are focused through a slit into a photo-cathode and in very much the same way as in photo-injectors electrons are produced. These electrons are accelerated and deviated by a synchronized linear sweep voltage and hit a phosphor screen, where the 'streak' across the screen is proportional to the time of arrival at the slit. The screen is then imaged onto a CCD. When ps range pulses are measured and pulse separation needs to be known these devices are the best and the easiest to operate, if they are available.

II.5.2.3 Frequency domain measurements

The main instrument used for frequency-domain analysis of mode-locked lasers is the RF spectrum analyser. It is used to measure the amplitude and phase-noise modulation spectra of the photo-diode signal also used for the oscilloscope measurements. The minimum detectable signal is

set by the input noise floor of the instrument itself (noise equivalent power). RF spectrum analysers typically have a useful frequency range of 100 Hz–1GHz, and can be extended with a lower frequency FFT analyser, if full noise characterization of the system is necessary. In our case for laser noise characterization the system also has to be able to perform gated measurements as the signal after amplification is no longer cw. As laser repetition rate is low, these measurements are rather challenging. For frequency domain measurements two spectrum analysers were used in our case: Agilent Technologies EMC Analyser E7405A, and Agilent Technologies MXA N9020A Signal Analyser. The former has been employed for measurements at the phase-coding, oscillator and preamplifier stage, where the signal is still qcw. The latter for measurements at AMP 1 and AMP 2 stages, as MXA N9020A Signal Analyser is capable of gated FFT measurements.

Noise measurements performed on the laser will be **detailed in III.2.2**. For the theoretical background of the measurements themselves one can consult references^{II.52,II.81}. For the phase-coding (described in II.2.1.4.) a frequency-domain measurement was developed to characterize the exact delay between the odd and even pulse trains, as any error here will be seen as a phase-error by the injector leading to charge fluctuations of the injector (II.2.3.1)

II.5.3 Optical elements affecting contrast

II.5.3.1 Stretcher/compressor

In II.2.2.5. the concept of chirped pulse amplification (CPA) was introduced. To obtain the shortest possible pulse duration after during this amplification process- only limited by the bandwidth - is only possible with careful phase control of the pulse during stretching and decompression. There are many different stretcher and compressor configurations existing. Both grating and prism based schemes are used in double pass in order to remove spatial dispersion of the beam. Two basic examples are shown in Fig. II.5.4. For high power CPA lasers, where stretching to several 100's of ps is required grating, with higher dispersion provides a better solution. In a negative dispersion configuration, light with shorter wavelengths takes less time to travel through the device, as it is less diffracted than light with longer wavelengths. In the case of positive dispersion, this is reversed. In a CPA system the total dispersions of the stretcher and compressor should cancel out.

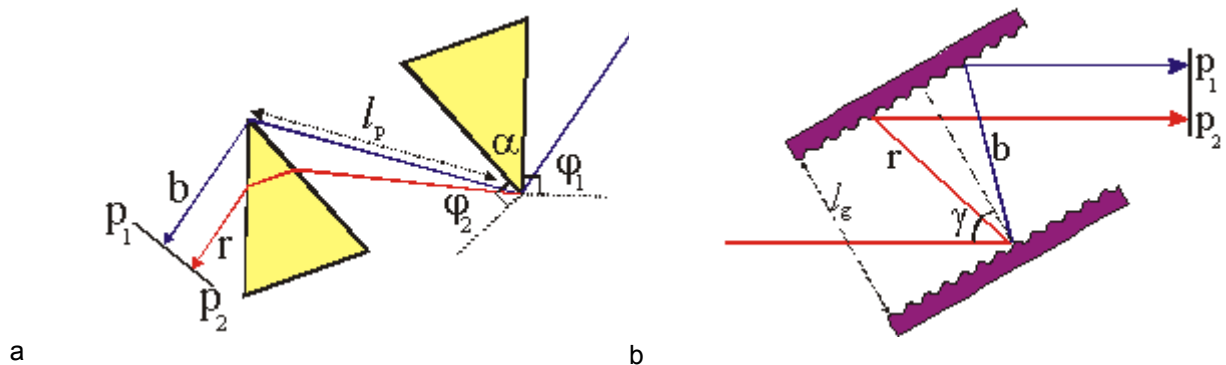


Fig. II.5.4. A typical setup of prism and grating pair for introducing and removing chirp. b and r indicates the bluest and the reddest part of the spectra. On (a) ϕ_1 is the Brewster angle.

However as additional chirp can be introduced by the amplifiers and other optics, simple matching of the stretcher and the compressor is not always sufficient. To achieve considerably shorter pulses, then 100 fs higher order dispersion control and compensation of the whole chain is necessary.

The negative group velocity dispersion introduced by a pair of prisms or gratings allows us to fully compensate for the second order phase variation across the bandwidth, but in both cases the 3rd order phase may remain non-zero after compression. This is negative in the case of a pair of prisms, and positive in the case of grating pairs.

Furthermore non-parallelism of the grating planes will leave residual angular dispersion¹⁸, which will limit the maximum focusable intensity. This manifests as temporal chirp and pulse front tilt and has been thoroughly investigated by the TeWaTi laser group in Szeged^{11.83,11.84,11.85,11.86}. The TOD component of this effect will cause contrast degradation at the ps levels. The problem is further complicated in this case, as angular dispersion induced chirp effect is evolving during the propagation of the pulse and so compensation is only possible for a certain target position in the case of plane waves.

Ultra-short lasers at fs range will have very wide spectrum. This will put a finite limit to the spectrum due to the size of available gratings. This in turn results in cutting the spectrum at a certain intensity level, which will be also discussed in the contrast calculations.

II.5.3.2 Broadband mirrors

A dielectric mirror designed for reflecting broad range of wavelength will consist of many thin layers of different dielectric materials.

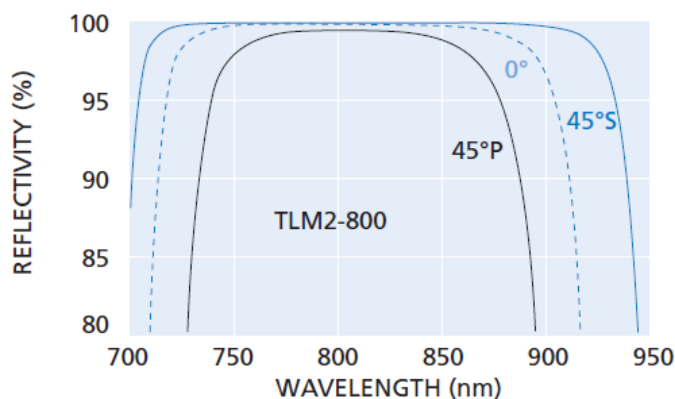


Fig. II.5.5. An example for spectral reflectivity of a broadband dielectric mirror from CVI Melles Griot

The reflectivity as a function of the wavelength will consist of a flat part, where the mirror is optimized and can be approximated by a half-Gaussian profile on either side of the spectrum (see Fig. II.5.5. for a typical spectral reflectivity). This approximation for dielectric mirrors was applied first by our group and this spectral soft cutting will be used later in our models to estimate their effect on the contrast.

¹⁸ **Angular dispersion** is defined by the angle between spectral phasefronts of the beam. Angular dispersion causes pulse front tilt and chirp. In the case of plane waves this can be compensated for a given plane, but residual pulse front tilt will still limit the maximum focusable intensity.

II.5.4 Contrast during amplification and conversion

Regenerative amplifiers introduced in II.1.3.2. are often used for ultrahigh intensity laser systems. They provide good pointing stability due to their cavity arrangement and gain over 6 orders of magnitude is achievable in one amplification stage. However they include electro-optical switches (PC) used to select pulses from the mode-locked seed oscillator. These devices (PC) usually have limited extinction ratio, which means, that corresponding to the cycle period of the master oscillator (seed laser) there could be pre- and post-pulses present and also amplified in these types of amplifiers. Multiple switches at the cost of additional losses can be installed before further amplification stages to eliminate these pre-pulses. Another limitation of these amplifiers is that when they are used for ultrashort and hence broad bandwidth pulses, they can suffer from severe gain narrowing. As the magnitude of the gain-narrowing effect depends not only on the gain bandwidth of the amplifier medium, but also on the level of the gain it is especially pronounced in regenerative amplifiers. By pre-shaping of the spectrum prior to amplification using acousto-optic devices or employing them inside the cavity, it is possible to fight the gain narrowing effect. To make the system amplifier more stable it is usually run in saturated mode, which will enhance amplified spontaneous emission. Delay of the pump at the trade in of gain could be a solution for reducing pre-pulses and pedestals at the ns level. Usually a balance can be found between gain and contrast of the amplified pulses, depending on the requirements on target^{II.87}.

- 5. My aim was to calculate the effect of real optical elements on the spectra and the phase and through these the effect on the temporal contrast. My aim was also to calculate the effect of temporal contrast degradation on commercial temporal shape measuring devices, such as 2nd 3rd order auto-correlators and cross-correlators.**
- 6. My aim was to show, that by measuring the spectra and the spectral phase the temporal contrast can be estimated with 2 orders of magnitude higher level spectral intensity.**

III. NEW SCIENTIFIC RESULTS

Given the specification discussed in II.2.1.3. and the critical requirement for high stability, the basis of the laser system has been chosen to be a diode-pumped Master Oscillator-Power Amplifier (MOPA) running in a steady state saturated mode. The active material Nd:YLF was chosen for its superior gain and thermal properties and the bandwidth, which supports <10ps pulse length, although its low fracture stress would ultimately restrict the maximum average operating power achievable from a single amplification stage. Side pumped rod geometry, offering good transverse beam shape and homogeneous pumping along the rod, using custom built diode stacks offers an efficient pumping configuration. The amplifiers are followed by a pair of non-linear crystals for conversion to the fourth harmonic at a UV wavelength suitable for the photo-cathode. For the seed, a commercial cw mode-locked oscillator is used, offering synchronizability to the external RF source, stability and efficiency. Additional components in the laser system will include feedback stabilisation, optics for beam relaying, spatial profile control, compensation for thermal distortion, and a Pockels' cell gate to define the ends of the pulse train. The main parts of this laser system requiring development are the design and operation of the amplifiers and the thermal management in the non-linear crystals. The amplifier must be efficient to minimise the cost of the pump diode arrays, have high gain to minimise the number of amplifiers and must show a very high degree of output stability under steady-state amplification. The harmonic stages then have to preserve the stability achieved in the previous stages. The work was completed in two stages. Firstly the PILOT laser system was provided the proof of principle for the amplifier design, with high single pass gain, but modest output powers to allow the first long train experiments on the CTF2 photo-injector at CERN. After the success and the learning on this system a larger scale, two stage amplifier system was developed for the CTF3 PI test stand, where apart from delivering the required energy/ pulse in the UV, stability, timing flexibility and long term reliability became the key requirements to meet.

III.1 Amplifier development for CERN CLIC photo-injectors

Table III.1.1. Parameters for PILOT and CTF3 amplifiers

Parameter	unit	PILOT	PHIN AMP1	PHIN AMP2
Length of rod	cm	5	8	12
Diameter of rod	mm	5	7	10
Effective pumping length	cm	4.5	7	11
Total peak pumping power	kW	5	18	25
Max. Duty cycle	%	2.5	2.5	2
Repetition rate	Hz	10 (100)	5/50	5/50
Max. average power	W	125	450	500
Cooling requirement	l/min	5	45	66
Number of passes		3-5	3	3
Gain		5000	300	5

In the following sections the detailed architecture and development of the laser amplifiers will be shown for both systems. The measurements with the detailed model will be discussed for amplification and thermal effects and the mechanical design to ensure easy alignment will be

presented. In total 3 pump chambers were built for CERN. One for the CTF2 PILOT laser amplifier and two for the CTF3 PHIN laser with the parameters are shown in Table III.1.1.

III.1.1 Amplifier pump chamber design

III.1.1.1 Mechanical design

The amplifier head for the PILOT laser system was constructed to the design shown in Fig.III.1.1. A 5mm diameter, 50mm long Nd:YLF rod with a wedge to avoid back reflections was orientated with the c-axis horizontal and normal to the rod axis. Five diode stacks were distributed around the rod.

The larger, 40° divergence angle of the diodes was along the length of the rod and was weakly focused by a spherical lens right in front of the diode stack ensuring, that at least 95% of the uncollimated diode output was intercepted by the rod. As the diode stacks have the typical 1cm array length across the rod, the spherical lens also has helped to focus the beam into the 5mm diameter rod in the radial direction. Residual unabsorbed pump radiation emerging from the back side of the rod is reflected back into the rod using thin layer aluminium coatings on the outside of the flow tube in regions not occupied by diode arrays. This ensures high absorption efficiency and helps to symmetrise the pump distribution over the rod cross-section. The rod is immersed in water both for cooling and to minimise reflection loss at the surfaces of rod (0.25%) and flow tube (0.2%). In this design the input and output flow tubes were placed at the bottom of the cylinder causing turbulence and allowing air-bubbles to sit at the top of the chamber.

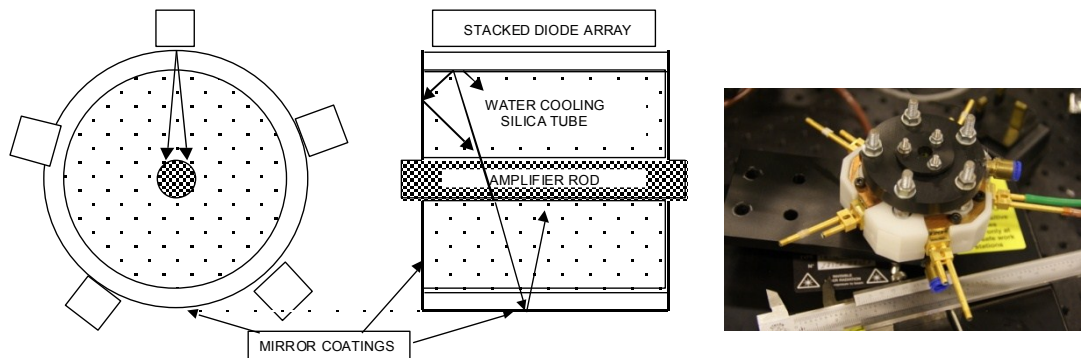


Fig. III.1.1. The PILOT amplifier head design and assembly

Moreover as Nd:YLF is birefringent and long rods are used one must take care of aligning the rod with its c-axis parallel to the laser table. Once the crystal was in place changing this alignment became increasingly difficult. A more stable mechanical design for holding the diodes also had to be implemented to make sure the emission angle was normal to the rod. The new assembly used for the PHIN laser is shown in Fig.III.1.2.

Since longer rods were needed for CTF3, custom diode stacks were purchased from DILAS and with larger rod diameters of 7 and 10mm required only very weak focusing with cylindrical lenses to match the rod cross-section. A key, designed to turn the rod while in situ was developed and there is

also a possibility to turn the entire head assembly around the length of the rod to align rod axis^{III.1}. Water connections were placed on the top for the inflow and the bottom for the outflow to ensure, that the cylinders were fully filled with water. Opaque pipes were chosen to avoid organic growth in the water.

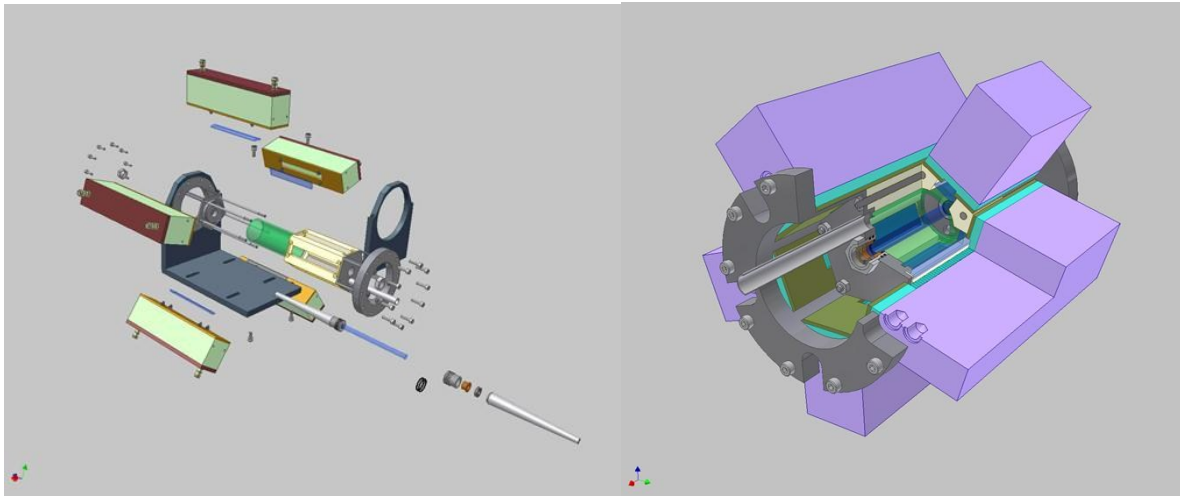


Fig. III.1.2. The PHIN amplifier head design and assembly

III.1.1.2 Absorption of the pump

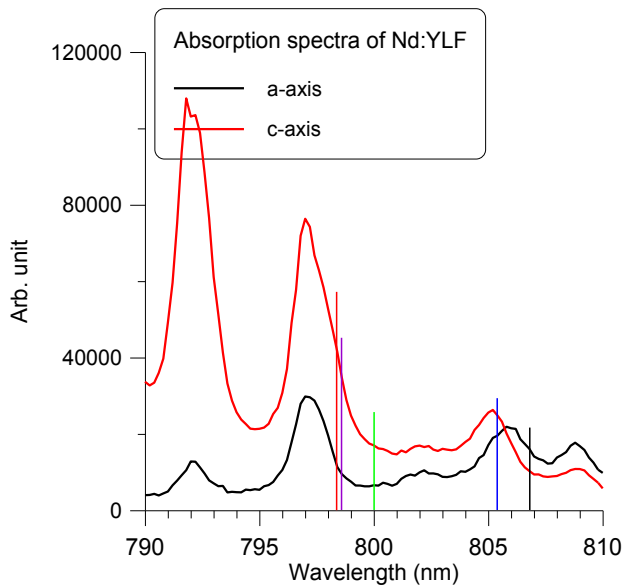


Fig.III.1.3. Absorption band of Nd:YLF along the two axes with diode emission lines marked for the 5 stacks in the PILOT system

For the PILOT system the diodes were purchased from Thomson CSF (now bought by Quantel) and main parameters are listed in table III.1.2. Wavelengths were in the range 798 to 807 nm to provide good absorption efficiency. The repetition rate was normally 5Hz, with pump duration in the range 400 - 800 μ s, but operation up to 100Hz was possible with reduced pump length whilst not to exceeding the 2.5% recommended duty cycle. As the diode emission is also polarized and the C-axis is placed horizontal in our arrangement, then apart from the diode on the top of

the laser head all diodes will have a mixture of e and o polarization with respect to the crystal. The absorption coefficient along the two axes are shown in Fig.III.1.3. Care had to be taken to place them around the rod to get good homogeneity of absorption and hence good gain distribution. As relatively large diameter rods are used in all cases, it is not practical to choose diodes, which emit at the absorption band, as absorption depth will not be sufficient to pump at the centre of the rod.

For the PHIN amplifiers custom built stacks from DILAS were purchased with a larger number of arrays, distributed evenly along the length of the rod. For these amplifiers I deliberately chose diodes in the ~802nm range as the absorption curve is flat here and it will make the amplifiers less

Table III.1.2. Pumping diode characteristics

Parameter	Unit	PILOT	AMP1	AMP2
Optical power/bar	W	100	120	
Number of bars		10	36	48
Operating current	A	<120	<120	
Voltage/bar	V	2.1	2	
Efficiency	%	39	50	
Wavelength	nm	797-807	800-810	
Line width	nm	<5	3	
Wavelength shift	nm/°C	0.3	0.25	
Fast/slow axis angle	deg	40/5	30/5	

temperature sensitive. As I have found no suitable codes available to model the absorption of such system, the optical part of the chamber was modelled in OSLO, while an in house code was written in MathCad for the absorption of the rod. Results obtained from measurements of the gain distribution will be presented in III.1.3.1.

III.1.1.3 Thermal effects/ Cooling

The aspects of thermal effects were discussed in II.2.4. Since the thermal dissipation into Nd:YLF due to the quantum defect is 32% of the excited state pump rate

then it follows that the maximum extractable power is a factor $(1-0.32)/0.32 = 2.13$ higher than the fracture limit, or 56W/cm, putting a limit to the maximum extractable power from given length amplifier.

Here I would like to point out that as thermal distortion due to average power heat is not symmetrical due to the birefringence of Nd:YLF and that the two amplifier stages of the PHIN laser were designed to have similar thermal load. By rotating the near field of the beam by 90° between the two amplifiers without turning the polarization theoretically allows the thermal lensing of the AMP1 to be compensated with that from AMP2. High repetition rate operation of this system however has not been performed to date, but at low repetition rates, up to 5Hz the scheme provided good beam quality with only spherical aberrations to compensate for. As PILOT system has permitted operation up to 100Hz, it was possible to carry out detailed thermal lensing measurement in this system and to scale this for higher power levels to predict performance at CLIC power levels. These measurements will be presented in II.1.3.6.

For simplicity and due to the relatively low thermal load in the case of the PILOT laser the same cooling circuit was used for the diodes and the amplifier rods. In the case of the CTF3 laser the systems were run from separate heat exchangers.

III.1.2 The laser setup

The mode of operation of the amplifier must be selected to give high gain, but at the same time it is necessary to operate under conditions of heavy gain saturation in order to achieve high efficiency and stabilise the output power. For the PILOT system several configurations were tested. First we used four-pass geometry as shown in Figure II.1.4., based on a novel 8-pass pumping geometry^{III.2}. As discussed before, ASE can put a limit to the extractable power and it is important to

avoid coupling between passes, which is difficult in the case of angular multiplexing for small diameter rods. For the 5-pass geometry, which was needed for the test at CERN due to the lower input oscillator parameters therefore a different scheme was used^{III.3}. In all cases the propagation distance between passes of 1m was chosen to decouple passes and to still have a practical length for alignment.

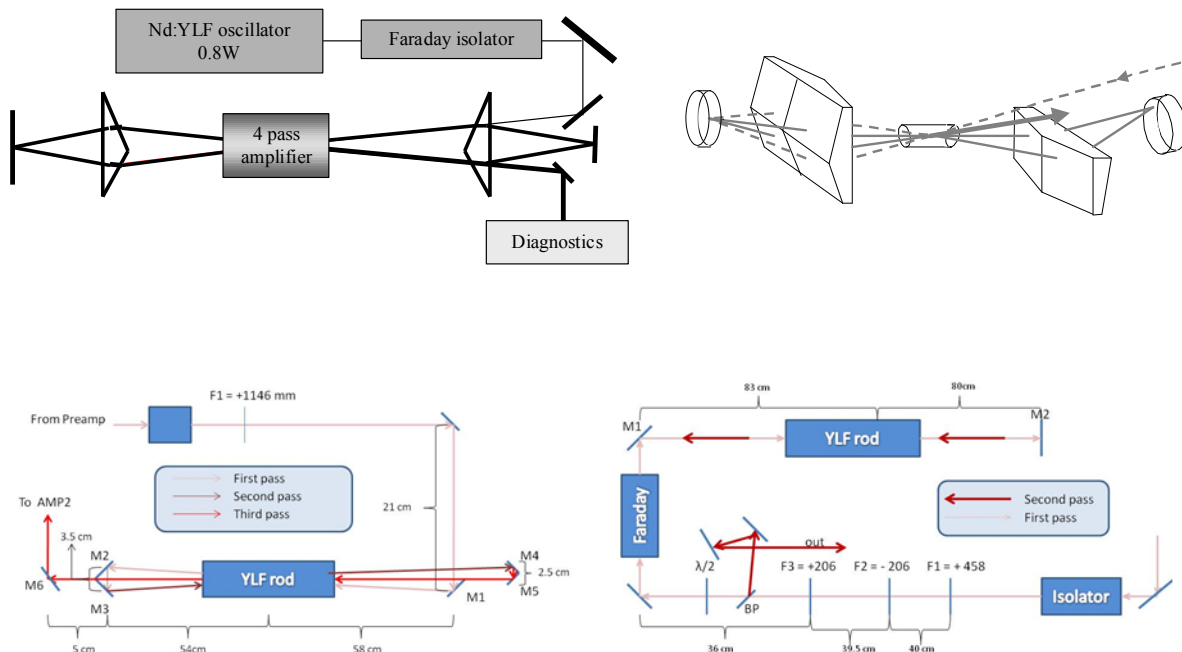


Fig. III.1.4. 4-pass geometry for the PILOT laser system (top) and PHIN AMP1 3-pass and AMP2 2-pass setup (bottom)

In order to establish the best operating mode and optimise the performance, a multi-pass analysis of this amplifier was implemented^{III.4}. We have proposed and analysed a 'quasi-steady-state' mode of operation for a pulsed diode-pumped laser amplifier. Under heavy saturation this amplifier has high extraction efficiency and is highly stable being only sensitive to changes in its diode pump power and coolant temperature. Later on the calculations were simplified for the CTF3 laser system^{III.6}. Detailed studies on the sensitivity to input variations were also carried out.

III.1.2.1 CTF2/ PILOT laser system

The final PILOT system setup is shown on Fig. III.1.5. The seed was initially provided by a cw laser source, a 800mW, CW Nd:YLF laser from Crystalaser and used for gain characterization. For the harmonic conversion studies a commercial (Coherent DMP 1000) additive pulse mode-locked Nd:YLF oscillator was used at RAL. The oscillator delivers ~5 ps pulses at 120 MHz and up to 1.5 W output power. However for the PILOT tests another oscillator has been used (LightWave), with 250 MHz 100 mW output, which is why it was necessary to increase the number of passes for this test. The variable input attenuator was used to check performance with different input parameters. It was followed by a Faraday-isolator to ensure that there are no back-reflections to the delicate synchronizable oscillator. After the 5 passes in the amplifier the signal is converted to UV using two non-linear crystals. In the

case of the PILOT experiment a gating PC, operating in the IR before the conversion stages was also installed.

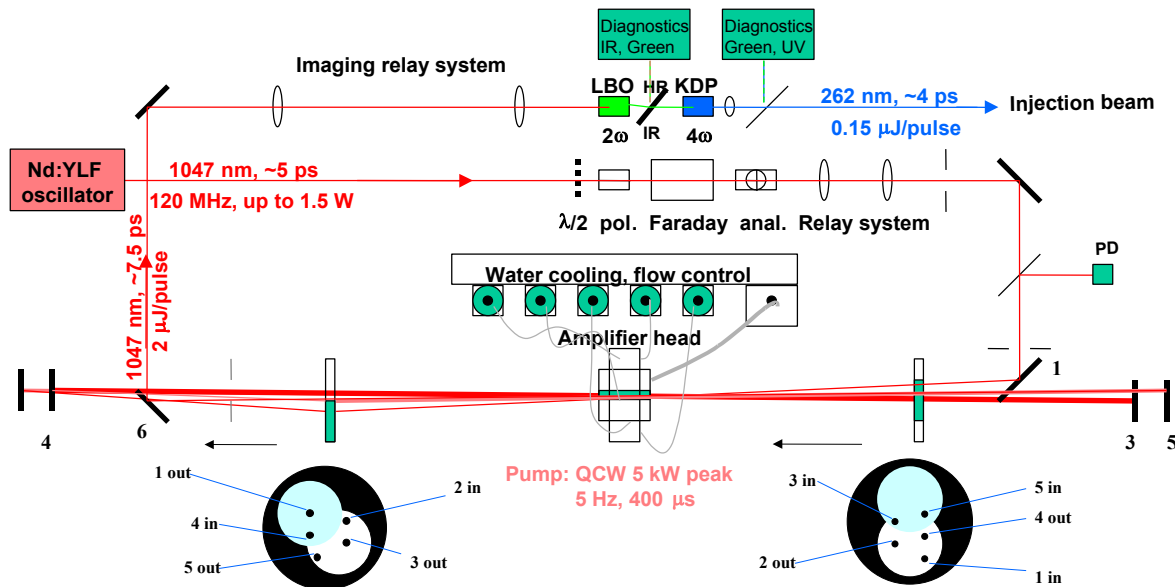


Fig.III.1.5. The PILOT laser system assembled for the CTF2 test

III.1.2.2 CTF3/ PHIN laser system

The PHIN laser system, shown in Fig.III.1.6., starts with a HighQ SESAM mode-locked oscillator at 1.5GHz repetition rate, delivering 320mW of average power and is followed by a cw pre-amplification stage also by HighQ. The preamplifier is based on a diode-pumped zigzag slab geometry and exhibits poor spatial profile, the amplitude stability of the system is ~0.6% rms. The synchronizability exceeded the specification and both with RF phase detection and optical cross-correlation measurements (against a same laser type) have shown excellent 130fs rms jitter. An M^2 value of 1.3 was measured upon delivery of the system.^{III.5} This is followed by the two powerful Nd:YLF amplifiers developed at RAL with the second one running only in 2 passes to utilize the filling factor increase due to the common path geometry, based on the Faraday isolator^{III.6}. This scheme was proposed by IAP Russia. As mentioned before a double periscope is installed between the two amplifiers to turn the beam for thermal lens compensation.

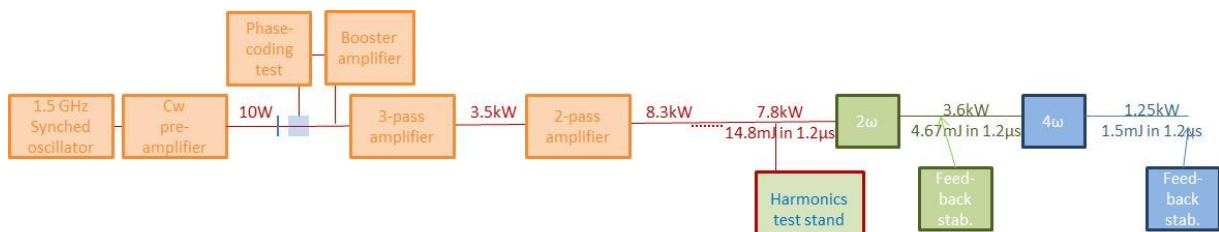


Fig.III.1.6. The schematics of the PHIN laser system

The amplification stages are followed by a PC gate from Leysop to cut out the required pulse-train from the steady-state part of the amplification for the conversion stages. This way minimum power load is sent onto the crystals. After the conversion the beam can be sent to the CTF3 or to the CALIFES experiment (see II.2.1.2.).

III.1.3 The model

If steady-state is reached during the pump period then the excited state population levels in the amplifier stay constant in time and there will be a balance between the input pump power reaching the upper laser level, the so called pump rate, and the sum of the power extracted by the amplified beam and lost to ASE, as described in eq.II.22. To apply to our 4-pass test amplifier, assuming a constant beam size from pass to pass and an intra-pass loss of l , the equation is re-written as:

$$I_p = f_1(G)I_{in} + f_2(G) \quad \text{III.1)}$$

Where:

$$f_1(G) = (1-l)^3 G^4 + (1-l)^2 LG^3 + (1-l)lG^2 + lG - 1 \quad \text{III.2)}$$

and

$$f_2(G) = I_{sat} \ln G \cdot (1 + B_{ASE}) \quad \text{III.3)}$$

and where: G is the single pass gain of the amplifier, B_{ASE} (described in equations II.28.) is the rate of ASE.

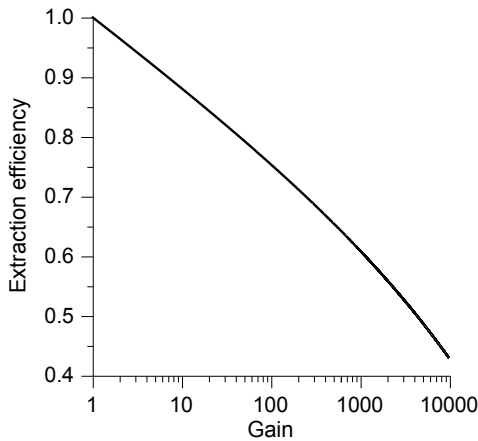


Fig.III.1.7. Extraction efficiency vs. amplifier gain

The extraction efficiency (η_{ex}) of the amplifier, is defined here as the ratio between the intensity increase of the amplified beam and the pump rate. Since the ASE loss increases with gain, it will be necessarily to compromise between efficiency and gain. For our 4-pass test amplifier Figure III.1.7. shows the calculated variation of efficiency with 4-pass gain and predicts that gains in excess of 10^4 can be obtained with Nd:YLF without a major reduction in efficiency.

Having established the expected performance in the steady state mode it is useful to consider the process by which the steady-state can be reached. This is also critical, as for CLIC 140 μ s long trains will be required and to understand how quickly before the end of the pump burst the steady-state is built up is important. To do this we calculate the dynamic response of the amplifier to an input signal beam consisting of a train of pulses and the pump, which is only present for a certain window of time. The dynamics of the amplifier are described by the spatial and temporal changes to the amplifier gain coefficient. For an input pulse train with a time separation of τ_s between pulses the incremental change in the gain coefficient from one pulse is affected by 3 things: the increase due to pumping; the loss due to fluorescence enhanced by amplified spontaneous emission; and the depletion of the population by the previous pulse. The net change is given by:

$$\Delta g(z,t) = \frac{\eta_R}{F_{sat}} \frac{I_p(z,t) \cdot \tau_s}{L} - \frac{g(z,t) \cdot \tau_s \cdot (1+B)}{\tau_{fl}} - \frac{g(z,t) \cdot F(z,t)}{F_{sat}}, \quad \text{III.4)}$$

where $F(z,t)$ is the sum of the single pulse fluence in the train in all passes at position z and time t . It is worth to note here, that time t is always on the scale of the pulse train and not on the scale of an individual pulse. We assume that the equilibrium in the level populations is re-established in $\ll \tau_S$ time. This was confirmed by measurements using single pulse amplification^{III.1}. For a single pass amplifier the pulse fluence at (z,t) is given by:

$$F(z,t) = F_{in} \exp \int_0^z g(z,t) dz \quad \text{III.5}$$

and for a 4-pass amplifier it is given by:

$$F(z,t) = F_{in}(t) \left[\begin{aligned} &\exp \int_0^z g(z,t) dz + l \exp \left(\int_0^l g(z,t) dz + \int_z^l g(z,t) dz \right) \\ &+ l^2 \exp \left(2 \int_0^l g(z,t) dz + \int_0^z g(z,t) dz \right) + l^3 \exp \left(3 \int_0^l g(z,t) dz + \int_z^l g(z,t) dz \right) \end{aligned} \right] \quad \text{III.6}$$

This type of calculation can also be adapted for other number of passes. The advantage is that we

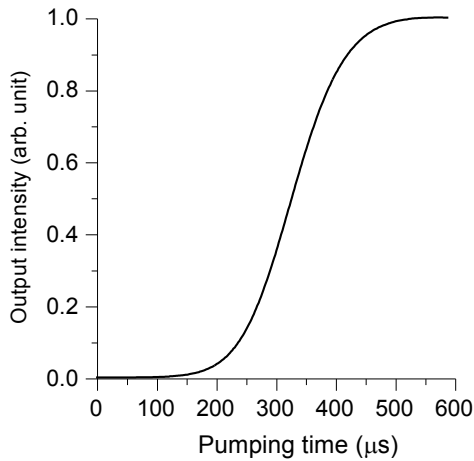


Fig.III.1.8. Gain profile of a 4 pass amplifier reaching steady-state as a function of pumping time (PILOT)

are calculating the amplifier performance from basic parameters of the input and by later fitting to measured values an insight can be gained into where losses occur in the system, or whether efficiencies for coupling, absorption and extraction are as expected.

Equations III.4 and III.6 represent the second amplifier rate equation which has been integrated under the assumption that the beam is a train of short pulses with an individual pulse fluence small in comparison to the saturation fluence and with a time between pulses long compared to the amplifier transit time. Solving these equations for the test 4-

pass amplifier with a constant fluence input pulse train of average power 500mW, and a constant pump pulse starting at $t=0$, gives the output fluence shown in Figure III.1.8. It can be seen that steady-state operation is achieved after 500 μ s with a perfectly stable output after this time. As the fluorescence lifetime of Nd:YLF is 470 μ s, when longer trains are required more passes can help by shortening the time it takes to reach steady-state.

The design obtained for the PHIN laser using the code in MathCad based on the equations above is shown in Fig. III.1.9. Such steady-state mode of operation of the amplifier with long build-up time suffers from an additional efficiency loss due to the amplification of unwanted earlier pulses. This can be reduced by gating the input pulse train to turn on some time after initiation of the pump at a time when the gain has first reached its steady-state value, as it was demonstrated in^{III.36}. This was considered for the PHIN laser scheme as a way of reaching steady-state quicker. As it can be seen pumping time and hence average power load could be reduced by ~30% using this scheme. However this requires accurate timing of the switch as it is shown on Fig.III.1.9 and it is not clear, whether

saturation building up later in the train will affect the beam profile over the train. It also adds additional complexity to the system, and care should be taken not to lose seed pulses, as in case of Pockels-cell failure, as this would increase the chance of parasitic lasing building up from high levels of fluorescence losses.

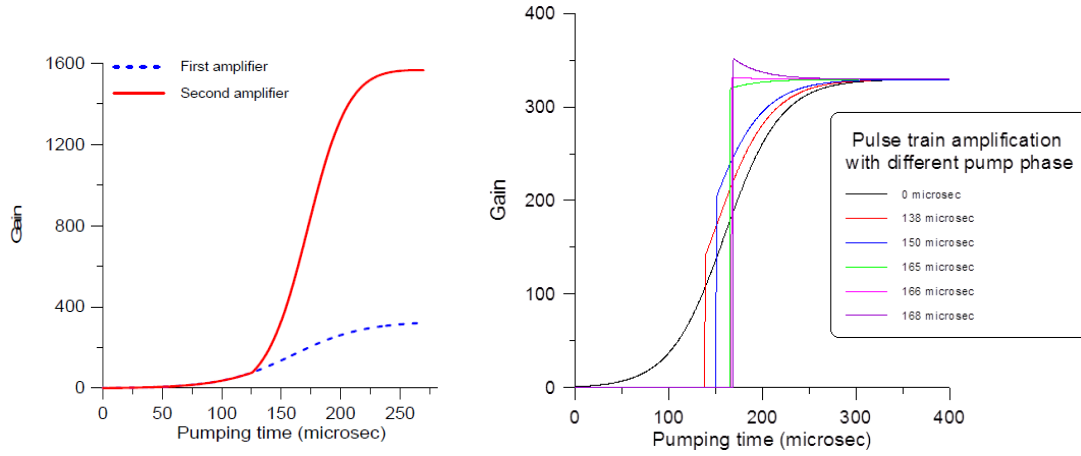


Fig. III.1.9: Calculated gain in the two amplifiers. The diodes in the first amplifier are switched on at $0\mu s$ and the second amplifier is switched on $125\mu s$ later. The dotted blue line shows the gain in the first amplifier and the red line the gain in both amplifiers together. It can be seen that the steady-state is reached after $250\mu s$. On the right the possible pre-pumping configuration is investigated for PHIN AMP1.

The analysis is given for Nd:YLF but can readily be used for other materials and amplifier designs. The code can also be applied for the design and prediction of CLIC amplifiers. For the CLIC specification and assuming a modest 5% conversion efficiency for the fourth harmonic generation the required laser output pulse energy would need to be $100\mu J$ giving an output fluence of $0.13mJ/cm^2$ for each pulse at the expected 10mm diameter for the final amplifier. This fluence is just 0.03% of the saturation fluence for Nd:YLF on the 1047nm line and leads both to negligible depletion of the amplifier stored energy by each pulse and also to negligible distortion of the pulses from amplifier saturation. Consequently it is valid to use a cw analysis to represent the mean power in the pulse train and enables us to use a cw rather than a mode-locked oscillator for a test programme.

III.1.3.1 Steady-state and stability

The output pulse train stability is an important criterion of the laser for PI application and it must be maintainable over periods of several hours. The proposed design of system aims to achieve the best possible stability by using diode pumping and by relying on heavy saturation of the amplifiers to provide a strong clamp on the output intensity. As it will be seen later that temperature also needs to be stable. A measure of the stability in steady state operation can be derived by differentiating equation III.1 to give:

$$dI_p = (f_1' I_{in} + f_2') dG + f_1 dI_{in}. \quad \text{III.7)}$$

Using the substitution $I_{out} = (1-l)^3 \cdot G^4 \cdot I_{in}$ leads to an equation for the interdependence between intensity changes of the input, pump and output beams:

$$I_p \frac{dI_p}{I_p} = \frac{G}{4} (f_2' + f_1' I_{in}) \frac{dI_{out}}{I_{out}} - \left[\frac{G}{4} (f_2' + f_1' I_{in}) - f_1 I_{in} \right] \frac{dI_{in}}{I_{in}}, \quad \text{III.8)}$$

where f_1', f_2' are the differentials of f_1 and f_2 respectively with respect to G . For the PILOT amplifier with measured values of 9 for G , 4.7 kW/cm^2 for I_{out} , and 0.2 for l this reduces to:

$$\frac{dI_{out}}{I_{out}} = 1.85 \frac{dI_p}{I_p} + 0.163 \frac{dI_{in}}{I_{in}}. \quad \text{III.9)}$$

The stability for the laser system is consequently largely determined by the stability of the pumping rate of the final amplifier and can cope with much larger variations from earlier in the system. So stabilising the pump rate in the final amplifier is the ultimate solution for good stability, as long as the seed laser is sufficiently stable, which is expected from an oscillator. However when fast noise in the input seed is present, as it was in the case of the LightWave oscillator used for the PILOT test, the gain does not instantly adjust to the changes of the optical input power, because the gain medium stores the energy and only loses it on the scale of the fluorescence lifetime. As stored energy determines the gain, the gain cannot change fast either, as it is expressed in eq. III.10. The change will be determined by the fluorescence lifetime with a correction depending on the level of saturation in the amplifier (eq. II.25.). An example is shown in Fig. III.1.6. calculated with the code using a suddenly changing input seed or pump. The example shown here were done for the PHIN laser after full amplification and once steady-state has been reached. One can see, that with 1% drop of either seed or pump the amplifier takes $\sim 80 \mu\text{s}$ to recover, and while in the case of seed variation saturation will almost recover output values the change is linear in the case of pump variation. The graph on the right illustrates, that as a result of the limited response time the amplifier even in saturated steady-state is not able to compensate for fast variations of the input parameters.

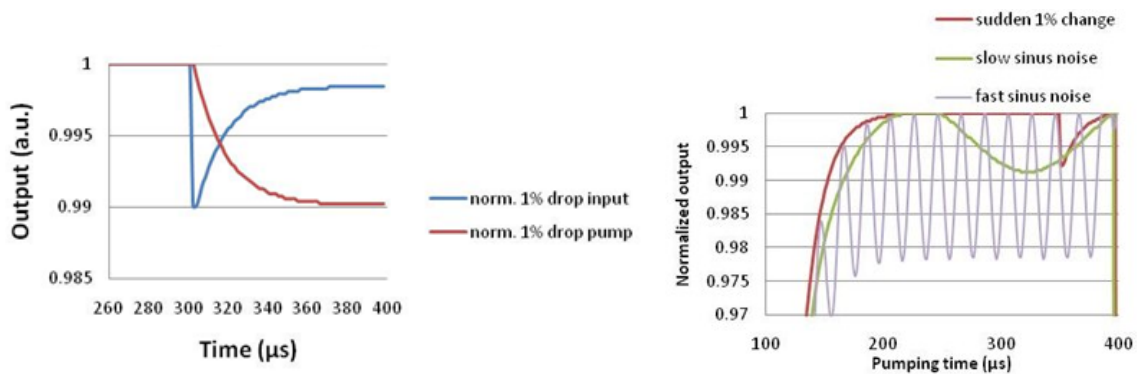


Fig. III.1.10. Response of the amplifier output to sudden 1% variations of the seed and the pump (left) and to periodic variation of the seed (right)

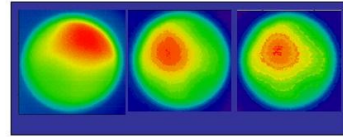
III.1.4 Experimental results and comparison with the model

III.1.4.1 Pump and gain distribution measurements

These measurements were carried out using two principle methods. One was measuring the small signal gain from a beam, which was overfilling the aperture of the rod and then imaged onto a camera. The background was removed by subtracting the unamplified background. The other method was to scan a small area beam across the crystal to measure saturated gain profile with a PD.

For the PILOT system, as only diodes with different emission wavelength were available an optimization was done in order to achieve best gain uniformity. Fig. III.1.11. shows

Changing the position of the diodes



Changing the temperature +/- 5°C

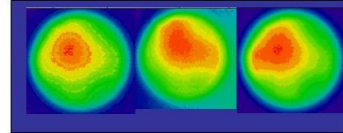


Fig.III.1.11. Fluorescence distribution as a function of diode position and temperature

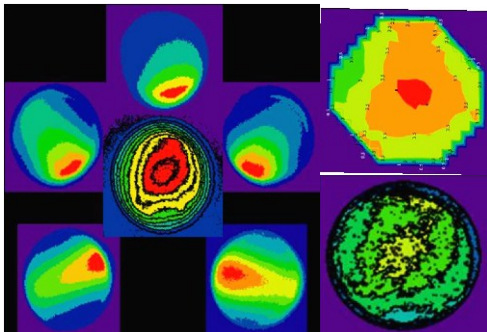


Fig. III.1.12. Fluorescence distribution (left) and small signal (top) and saturated gain distribution (bottom) (contour intervals are 12.5%, where not indicated)

equivalent to 50% ' π ' and 50% ' σ ' and provides a pumping uniformity of 25% over 80% of the rod area as illustrated in the centre image showing the heavily saturated gain distribution.

Figure II.1.13. shows the same measurement carried out on the PHIN laser. The effect of the diode polarisation is visible here as well, with the diodes closest to the horizontal (Fig II.1.13. c,d) being most strongly absorbed. When we pump with all five diodes, the five-fold geometry and slight offset of each diode from the centre-line of the rod enable us to obtain a pumping uniformity of an excellent 80% over the total area of the rod.

examples with different diode arrangements and temperatures. The distribution shown in Fig.II.1.12. was found to be best. The effect of pump polarisation is seen since at the top diode presents an extraordinary ray which is more strongly absorbed by the rod, and the bottom diodes are mostly ordinary ray polarisation at the rod and the absorption is less. The combined effect of all diodes is

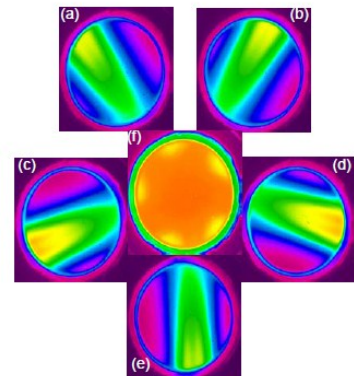


Fig. III.1.13. Measured fluorescence distribution from each of the five diodes individually (a-e) and from all five diodes together (f).

III.1.4.2 Small signal and saturated gain measurements

The PILOT amplifier exhibits very high single pass small signal gain of ~ 27 , leading to a small signal gain of over 10^5 in 4 passes when pumped over $600\mu\text{s}$. This confirms that Nd:YLF was a good choice for its high gain absorption of diode wavelengths. Also shown in Fig. III.1.14. is the measured gain profile for small signal and saturated amplification. The best match to the measured gain curve gave a combined pump cavity transfer and rod absorption efficiency of 53% compared to the

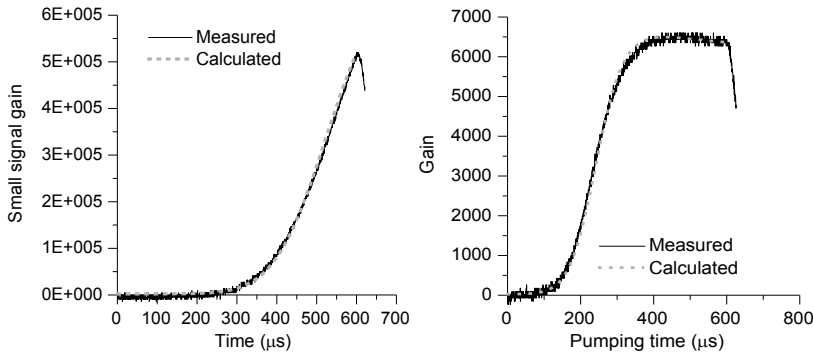


Fig. III.1.14. Small signal gain and saturated gain of the PILOT laser system running in 4 passes.

estimated maximum of 75%. The difference is largely accounted for by the lack of anti-reflection coatings on the flow tube and lenses. These were later added to the system and the efficiency rose to 65%. At the maximum available input power of

450mW into the first pass it was possible to strongly saturate the amplifier, giving the evolution of output intensity shown on the right of Fig. III.1.14.. This is seen to be in good agreement with the calculated profile, and in this case the steady state is reached after $350\mu\text{s}$ as expected, with output intensity at $7\text{kW}/\text{cm}^2$, which is 8 times the saturation intensity for Nd:YLF.

Further evidence for the degree of saturation is indicated by the change in output beam spatial profile as a result of the amplification (Figure III.1.15.). This amplified beam has a flattop of diameter 2.5mm at the 80% points containing a peak power of 380W, in comparison with the unamplified approximately Gaussian profile with a FWHM of 1mm.

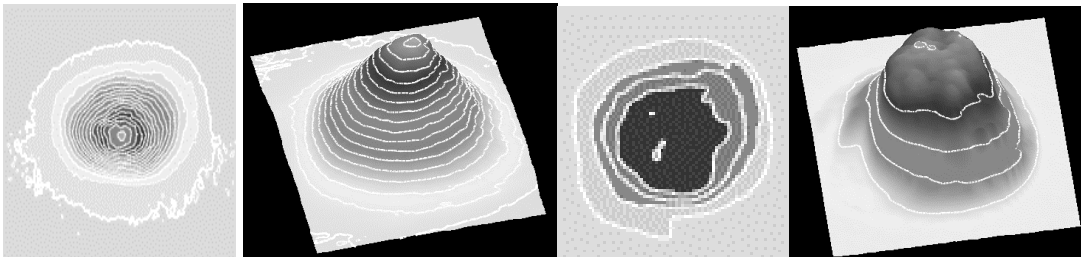


Fig. III.1.15. Unamplified (left) and amplified (right) beam profiles through the system showing the effects of strong saturation, which generates a flattop from a Gaussian profile. (Contour interval is 6% for the unamplified beam and 20% for the amplified beam.)

The same measurements were carried out for the PHIN amplifiers. As the development of AMP2 was done by my colleagues, I will only present here the final results and will concentrate on the 1st amplifier. Fig. III.1.16. shows the small signal gain measurements for AMP1. As this is the higher gain system it was important to check, that ASE does not appear at longer pumping times which will be required to reach the steady-state gain of 300. The measurements presented for AMP2 in^{III.6} were done at extremely long pumping time without extraction of the power from the amplifiers and give an

unrealistic estimate of the ASE. We have measured the gain of the first amplifier in single pass and compared the results against the predictions of the code. The measured and calculated single-pass gains obtained with input powers of 200 mW and 6800 mW are shown in figures 5 and 6 respectively. The measurements show good agreement with the code, except at the highest input and pump powers (f) when the measured gain is ~80% of that predicted. This discrepancy between the code and measurements suggests that the model for ASE used in the code is not correct. However, we do still obtain sufficient gain. With the design values of 6.8 W input power and 15.8 kW pump power, we measure a single-pass gain of >200. Later it was shown, that ASE has indeed hampered the performance at higher pumping powers and harmonics were not possible to produce at the predictable level.

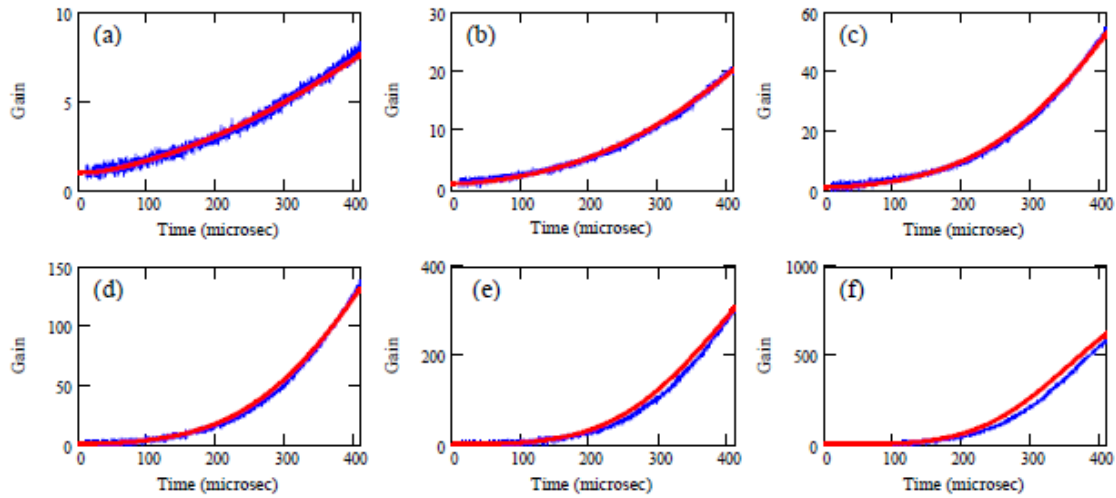


Fig. III.1.16. Measured (blue) and calculated (red) single pass gain with pump powers of (a) 4.7 kW, (b) 6.9 kW, (c) 9.2 kW, (d) 11.4 kW, (e) 13.6 kW and (f) 15.8 kW. The input power was 200 mW.

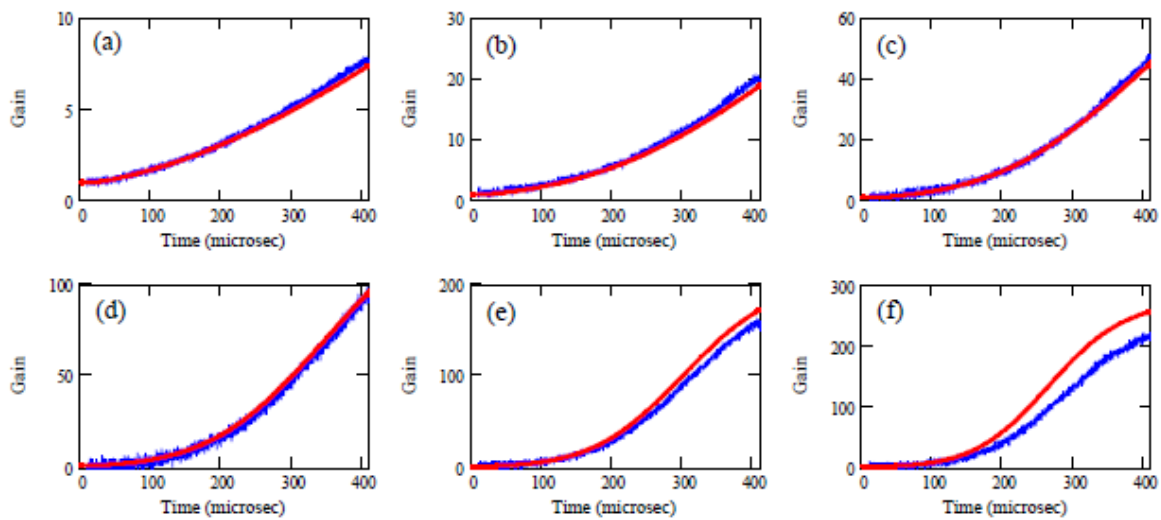


Fig. III.1.17. Measured (blue) and calculated (red) single pass gain with pump powers of (a) 4.7 kW, (b) 6.9 kW, (c) 9.2 kW, (d) 11.4 kW, (e) 13.6 kW and (f) 15.8 kW. The input power was 6800 mW.

After this the amplifier configuration was changed so that the beam was expanding over the passes to obtain high initial rise of the gain. To ensure that extraction is efficient, the beam was expanded for the last pass to ensure the beam filled the diameter of the rod and was sent in on-axis. The experience was, that when the laser is aligned perfectly without internal reflections in long rods or coupling

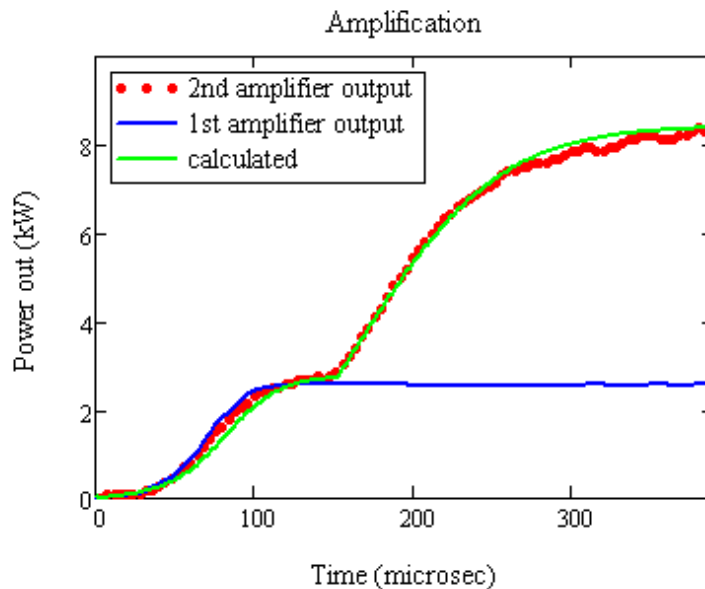


Fig.III.1.18. Measured and fitted saturated gain curves for AMP1 and AMP2 with 90A pump current, (16.2kW for AMP1 and 21.6kW)

between the passes, then the level of ASE did not cause a limitation to the achievable output power. The result with the optimized 3 pass arrangement with the beam expanding over the passes is shown in Fig. III.1.18.. It can be seen that steady-state is reached much faster compared to the III.1.16.f graph, taken under the same pumping and seed power conditions. Using the design code with the input parameters corrected to the small signal gain measurements the fitting was performed. Originally the code was designed to calculate for constant beam size along the passes, but of course this is far from the reality especially in the 3 pass case. I have introduced a beam fill factor to compensate this weakness of the code and obtained good agreement. Efficient conversion with this configuration was taken as a further proof of

reduced ASE levels. Further amplification was done in the above mentioned two pass arrangement to reach higher output powers, a 3 pass arrangement would be the

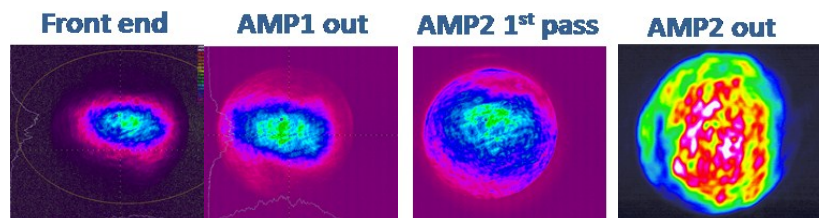


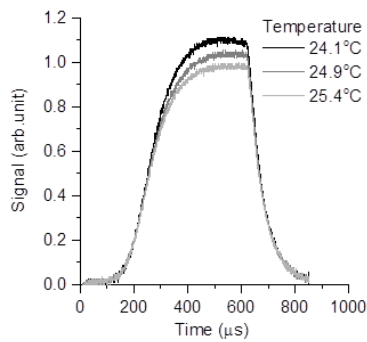
Fig. III.1.19. Obtained beam profiles with the gains of previous graph

ultimate solution and further development in the future towards this could be performed. It can be seen, that the system is still not fully saturated. By pumping for 300 μ s instead of 250 μ s one should be able to reach 9.3kW, and by in the same time increasing the pump current to 100A, instead of the

applied 90A 10.6kW mean power is expected according to the code. Near field beam profiles of the amplifiers were recorded (see Fig. III.1.19.).

III.1.4.3 Stability measurements

As it was shown earlier in the model the main factors, which determine the stability of such system are the seed and its noise frequency, and the stability of the pump, including temperature induces variations. In the PILOT system the diode driver was stable to about 0.5% long term and the temperature of the coolant to 0.5 °C. For the PHIN system both of these were improved to 0.1%. This was achieved by a stabilized diode driver (Lydia) in the latter case. Evidently both of these could be improved. An indication of the need for precise control of temperature is shown by an example of the measured variation of output with temperature shown in Figure III.1.20. .



III.1.20. The dependence of the amplified signal for different coolant temperatures on the PILOT system.

Amplitude stability measurements were conducted using an InGaAs photodiode, which has a very low temperature coefficient at 1047nm and is not sensitive to background visible radiation, together with an oscilloscope with ADC stability in the region of 0.1%. After allowing a period of at least 30 minutes for stabilisation, the short and long-term stability of the output power were measured and are shown in figure III.1.21. The rms stability was measured at less than 0.2% in short term and less than 0.7% over a period of one hour which is comparable to the reported levels of systems which also include feedback stabilisation.

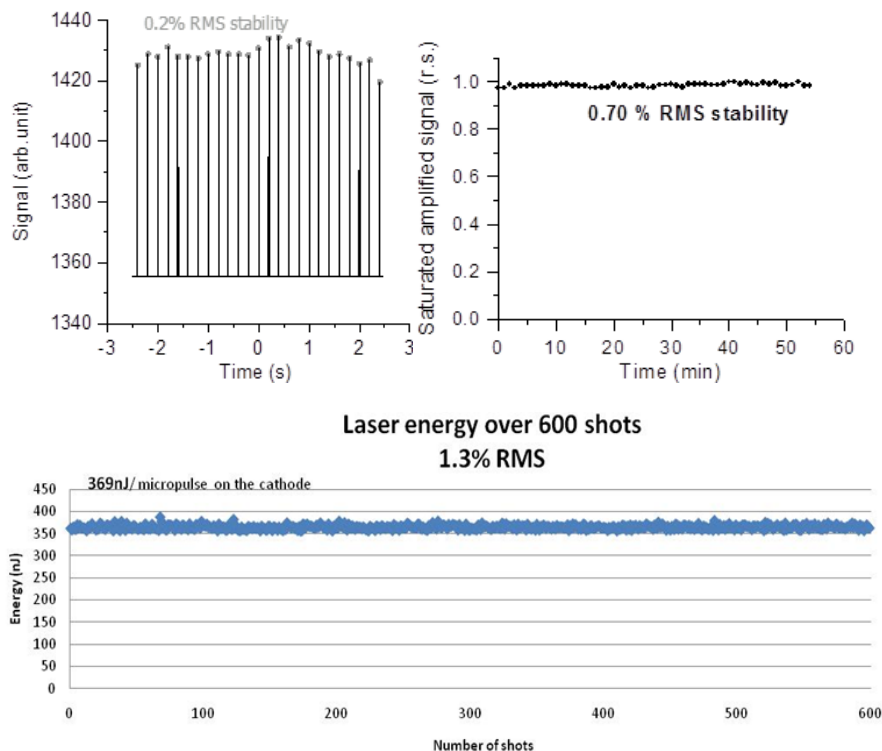


Fig.III.1.21. Short-term and long-term stability of the amplified signal with strong saturation of the PILOT system (top); energy stability at the cathode at 'the harmonic wavelength of the PHIN laser system

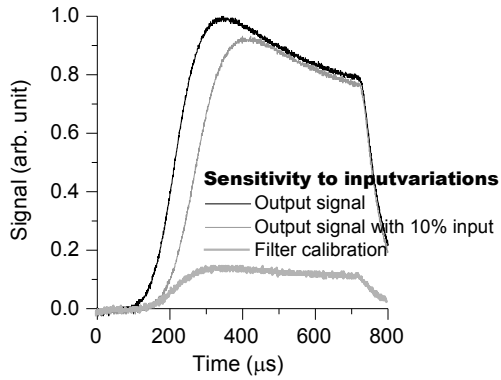


Fig. III.1.22. Low sensitivity of the amplified signal to a large attenuation of the input signal.

In order to demonstrate the insensitivity to variations due to the amplifier input power drift, the amplifier was operated at maximum gain saturation (top curve in figure III.1.22.) and the oscillator was then attenuated by a factor ~ 10 . This led to a reduction of just a few % in the saturated output of the amplifier (middle curve of figure III.1.22.). However when measurements were done in the presence of fast input seed variations during the PILOT test, the output was found to exhibit the same variations. Similar observations were made for the PHIN laser system,

where the oscillator exhibited q-switching instabilities at high frequency (with four characteristic frequencies), which then were carried through the system during amplification as shown on Fig. III.1.23. and were also apparent after the harmonic conversion.

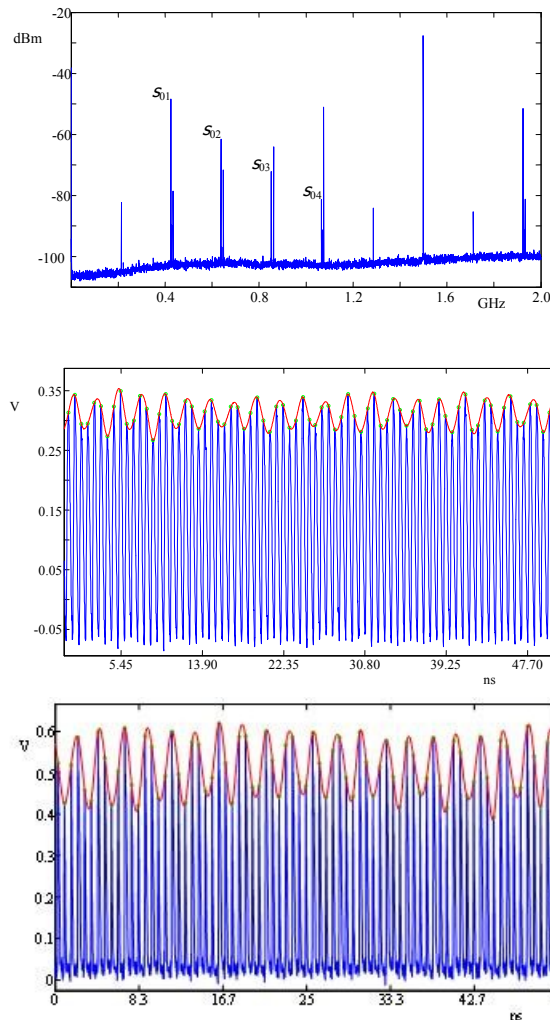


Fig.III.1.23. Modulation of the oscillator power at the PHIN front-end (top and middle); modulation carried through the amplifier, measured after AMP2 (bottom)

III.1.4.4 Thermal effects

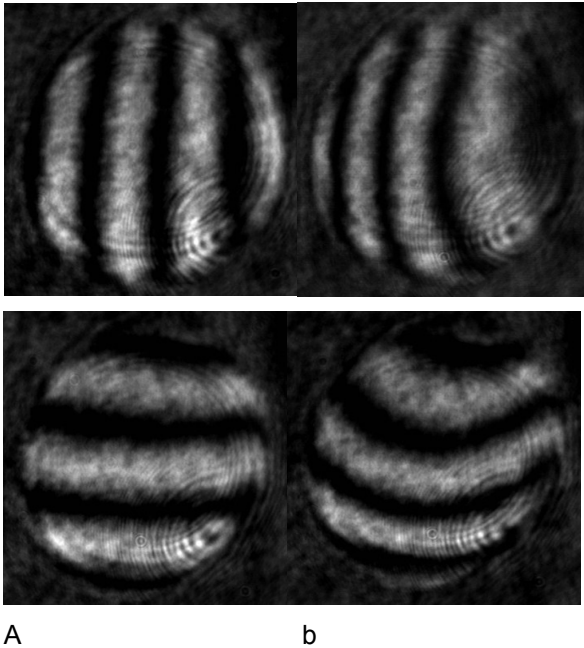


Fig.III.1.24. Interferograms showing the thermal optical distortion of the amplifier for a thermal deposition rate of 10 watts. a) and b) show the interferograms for orthogonal orientations without and with pumping respectively.

orthogonal orientations are shown in Figure III.1.24. for 10 watts average thermal power deposited in the rod. A Zernike analysis of these interferograms suggests only primary astigmatism and defocus are present and indicates that the aberrations can be effectively compensated using cylindrical lenses. Using the measured Zernike coefficients, the Strehl ratio was calculated and plotted in Figure III.1.25. using an extrapolation to higher powers. On this graph it is also shown, that for the thermal powers ~ 170 W at 50Hz operation for an amplifier with CLIC output parameter requirements the Strehl ratio would be at ~ 0.02 . With compensation only by cylindrical optics this could be improved to ~ 0.7 . Taking 0.8 as a minimum acceptable value for the Strehl ratio, this analysis predicts that the amplifier can be used up to a thermal power deposition in the rod of 15 W without requiring optical compensation and this corresponds to an average output power of up to 40 W for an amplifier operating at high efficiency. As for the PHIN amplifiers the maximum operational repetition rate so far was 5Hz,

As the optical quality of the amplified beam is important for the harmonics stages and for long distance propagation to the cathode, I have carried out extensive thermal lensing measurements for the PILOT laser system, where the higher repetition rate operation in the test phase was possible. Nd:YLF was selected as the gain medium due to its much reduced thermal lensing in comparison with other materials such as Nd:YAG. I used a radial shear Sagnac interferometer placed in the amplified beam to measure the thermal lensing, and the recorded interferograms were captured and analysed using a CCD, frame store and software package Fringe Analyser (Oxford Frame store Applications Ltd.). Examples of the interferograms recorded with and without the amplifier being pumped and for

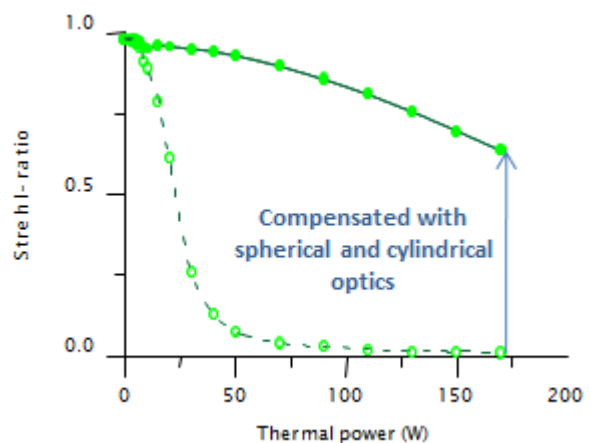


Fig.III.1.25. Strehl-ratio for a 5mm diameter rod at different levels of thermal deposition extrapolated from the measurements at low power (dashed) and after compensation of astigmatism (solid)

corresponding to ~13W thermal deposition and compensation was not necessary. As the design also included the same thermal load for both amplifiers, with the beam turned in between, only minimal astigmatism is expected after the second amplifier.

III.1.4.5 Harmonic conversion

For the PILOT system an LBO Type I crystal is used as second harmonic crystal and a KDP Type I as a fourth harmonic, both 2 cm long. To reduce losses and simplify the arrangement the same relay imaging system creates the ideal beam size for both harmonic stages. The pulse is stretched up to ~7.5 ps during the amplification due to gain narrowing of the spectra, and the pulse-energy is ~2 μ J/micro pulse. The over-all conversion efficiency is 5%, as can be seen on Fig.III.1.26. The uncompensated astigmatism from the amplifier is visible on the final beam shape (III.1.26. right) and can easily be compensated for when the beam transport is designed to the cathode. The total efficiency is slightly below the specification and can potentially be improved by compensating for astigmatism before the crystals.

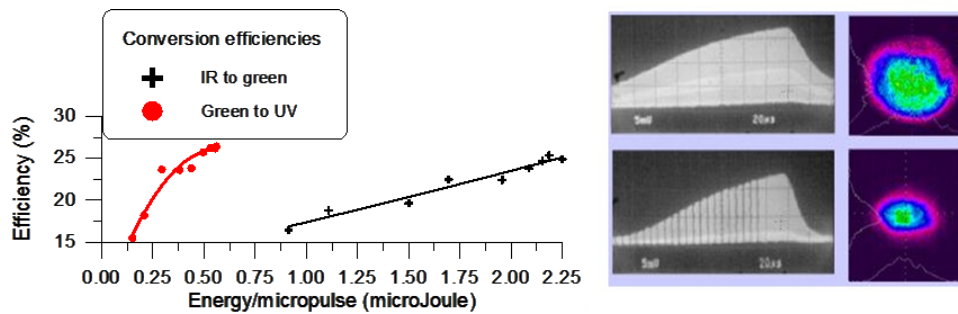


Fig.III.1.26. Conversion efficiencies (left) and gain and beam profiles (right) for the PILOT laser system.

For the PHIN laser system the development of the harmonics stages were done in conjunction with CEA France and IAP Russia. The performance is shown in Table III.1.3. For the second harmonic Type II LTB and for the 4th harmonic Type I ADP was chosen to get higher efficiencies due to its temperature tuneability and hence non-critical phase-matching. The ADP crystal was not performing well for long trains, where thermal effects have caused detuning at the centre of the beam, causing the distortion. For this reason the crystal was changed to a lower efficiency KDP (20mm long), but with improved beam profile. With this configuration up to 450nJ/pulse was delivered to the cathode in the nominal train length, exceeding the specified 370nJ/pulse.

Table III.1.3. Conversion efficiencies for the PHIN laser system

	1047nm	523nm	262 nm
RMS stab. (train)	0.23%	0.8% (0.45%)	1.3% (1.6%)
Energy/pulse (μ J)	5.37	2.5	0.87
Pulse length (ps)	7	7	~5ps
Beamsize (μ m \times μ m)	418 X 372	370 X 224	
Conversion efficiency	(T=89% to harmonics)	47% (best 50%)	35% (best 47%)
Crystal	-	KTP 11mm	ADP 20cm @23.6°C

III.1.5 Conclusion

A multi-pass diode-pumped amplifier designed to provide a combination of high gain and efficiency with high stability was developed for CERN CTF2 and CTF3 photo-injectors. A simple rod-cavity design and the establishment of quasi-steady-state operation resulted in a high gain saturated operation with mean output intensity during the pulse train of $7\text{kW}/\text{cm}^2$ in the case of the PILOT laser and $9\text{kW}/\text{cm}^2$ in the case of the PHIN laser.^{III.3,III.4,III.5,III.6,III.7,III.8,III.9.} A code was developed to verify the operation of the amplifiers and provide a useful tool for further designs^{III.6.}

The amplifiers showed an output stability of 0.2% rms and 0.34% rms respectively and proved the capability to compensate for slow drifts of the input intensities. Response to fast variations was studied for the steady-state regime and time- and frequency domain measurements were carried out to study noise propagation through the system. The output pulse stability already competes favourably with the best previous measurements on lasers with active stabilization and we know this can be improved using a more stable diode-laser power supply and improved coolant and room temperature stability. Additional stabilisation is also achievable using a closed cycle feedback control system.

Zernike analysis of the measurements of thermal distortion from the pump beam showed an almost pure astigmatic phase error and showed that Nd:YLF was indeed a good choice as an amplifier material and that the distortions can be compensated, up to high average power levels.

The PILOT system has allowed the first long train injector operations at CERN and the PHIN laser system, used for studying high charge photo-injectors is still unique of its kind with its high average current capability.^{III.10-III.17} The specified energy levels were delivered to the cathode and by providing the laser for the CALIFEs injector the first two-beam acceleration experiments took place as a proof of principle for CLIC scheme. The stability of the laser is planned to be further improved in the future by the installation of an active feedback stabilization system.

III.2 Correlation measurements of the laser and electron beams

To understand the net effect of all the noise sources existing in the laser system on the produced electrons and to see how much further parameters would have to be improved to achieve the performance, I have carried out correlation measurements between the laser and the electron beam both for amplitude (laser energy, beam charge) and for pointing stability. Study of the evolution of the pulse train was also carried out as a function of laser beam segment. The measurements are detailed in the following sections.

III.2.1 Electron beam diagnostics

A detailed description of the beam diagnostics (Fig.III.2.1.) and the measurements during commissioning of the machine can be found in references [III.10] and [III.17].

A fast current transformer (FCT), installed directly after the gun, is used to monitor the extracted charge. With the provided 1GHz bandwidth the individual bunches cannot be resolved, so only bandwidth limited measurements were carried out which give a signal proportional to the beam

current. Focusing solenoids and steering magnets ensure the delivery of the beam centred on the vacuum pipes, by monitoring the signal on the Faraday-cup (current measurement) and on the Beam Position Monitor (BPM). The beam position monitor is based on quadrant detection and is calibrated for charge measurement. This signal was used for total pulse (bunch-train) charge measurements. For the pointing stability measurements the electron beam was directed onto the centre of the Optical Transition Radiation (OTR) screen and the radiation produced was imaged onto an intensified camera.

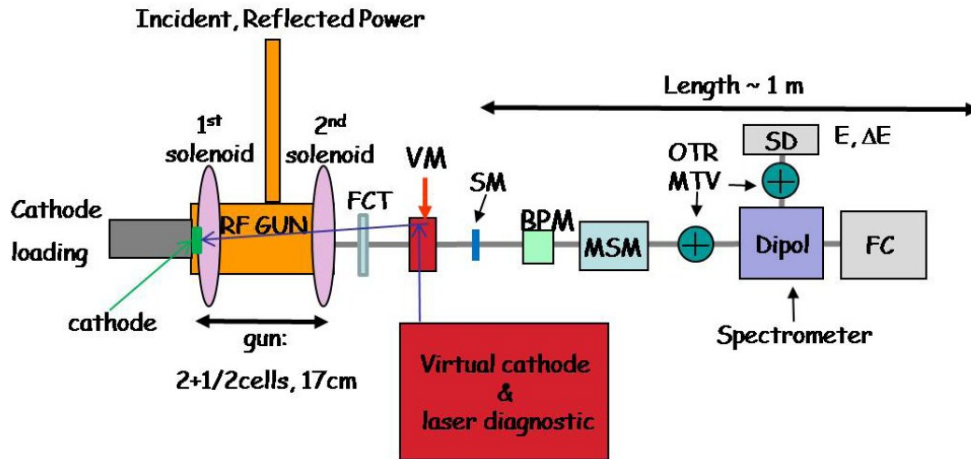


Fig.III.2.1. Beam diagnostics for PHIN. FCT: Fast current transformer; VM: Vacuum mirror; SM: Steering magnet; BPM: Beam position monitor; MSM: Multi-slit mask; OTR: Optical transition radiation screen; MTV: Gated cameras; SD: Segmented dump; FC: Faraday cup.

III.2.2 Transport line and virtual cathode

The PHIN transport line is based on a simple two-lens system design, where imaging onto the cathode is achieved with the nominal beam size on the cathode. As cost restraints did not allow automation of the optics mounts, both lenses were located in the laser room and could be manually moved or exchanged to vary the beam size on the cathode. The aim was also to keep the beam size on the vacuum mirror as small as possible, as the usable aperture for the laser beam there is <1cm. The total beam path was ~14m, of which 11m was not accessible during operation. Fig. III.2.2. shows the beam propagation from the 4th harmonic crystal to the cathode with mirror positions marked.

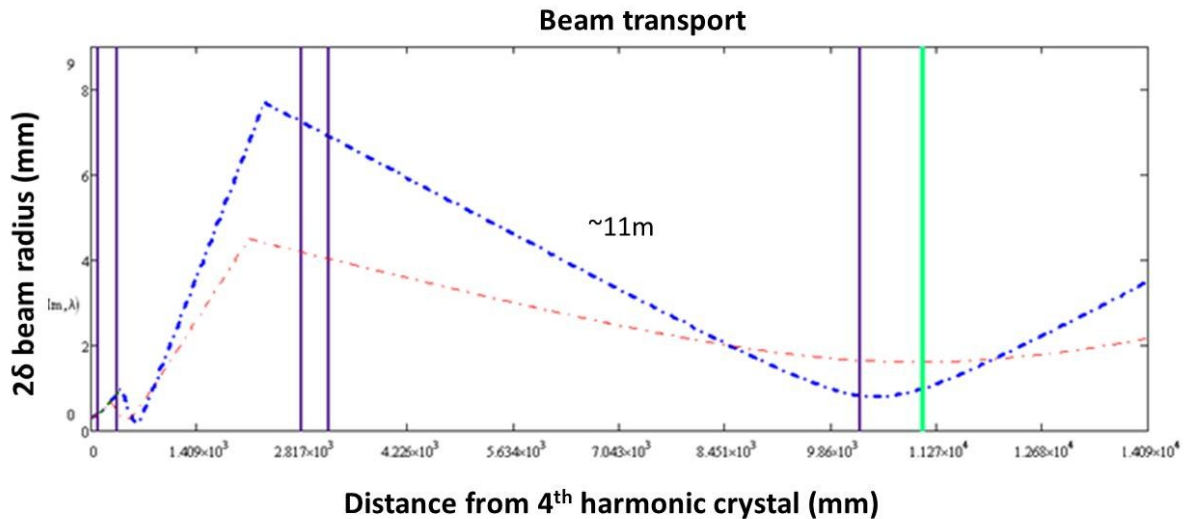


Fig.III.2.2. Beam transport design for PHIN starting from the 4th harmonic crystal to the cathode. Blue lines indicate transport mirror positions, while the green is the mirror inside the vacuum pipe.

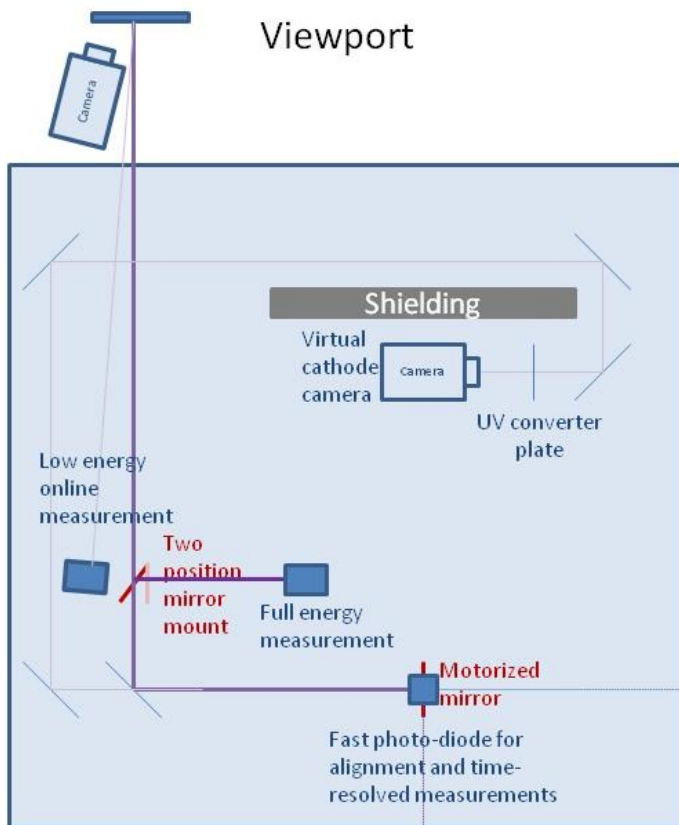


Fig.III.2.3. Virtual cathode beam diagnostics for the PHIN system

The diagnostics were placed equidistance to the cathode on a diagnostics table to measure laser beam parameters before entering the vacuum pipe and are shown in Fig.III.2.3. A remotely controlled flipping mirror allows a direct energy measurement of the full beam. An online energy measurement calibrated to this, using the reflection from the viewport is also available. In both cases LaserProbe silicon detectors were used. A virtual cathode (VC) camera looking at the fluorescence produced by the UV light on a YAG screen is used to monitor the laser beam size and position. The macro-pulse amplitude stability measurement over the train was obtained by both the energy measurement and the integration of the window of interest from the VC camera and showed a good agreement.

III.2.3 Pointing stability measurements

Electron beam and laser beam positions were recorded shot to shot with camera acquisition software written in MatLab. A gaussian fitting routine was used to determine the centre and the size of

the beam. Figure II.2.4. shows a typical correlation measurement between the laser and the electron beam showing that most of the beam movement is induced by the movement of the laser beam on the cathode. As the beam transport is in free space over 3 floors and a few degree temperature gradients, large relative movements of the beam are not surprising.

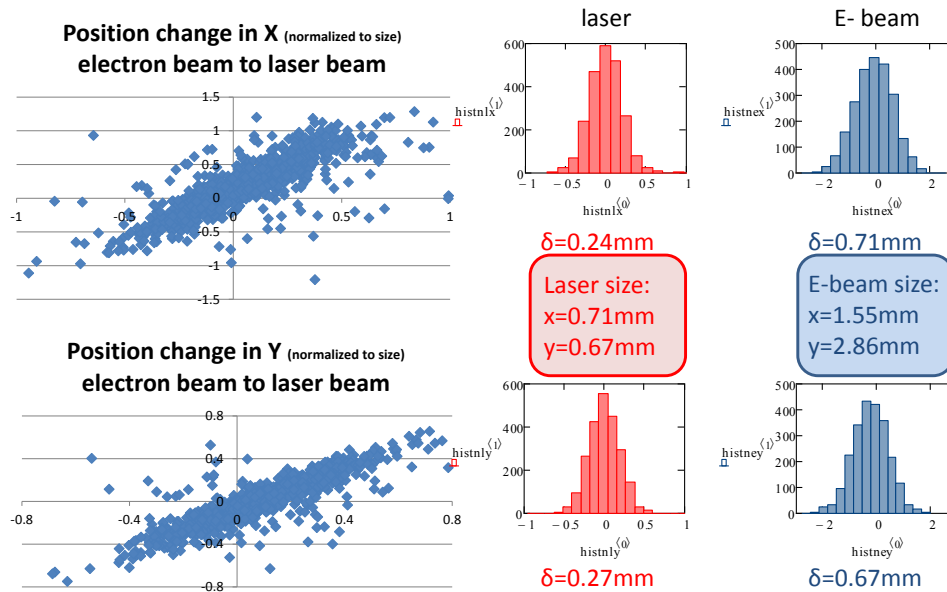


Fig.III.2.4. A typical beam correlation plot between the laser and the produced electron beam

Similar measurements were carried out between the laser beam in the laser room and on the virtual cathode camera in the machine building. The pointing stability was almost three times better in the laser room, as can be seen from Fig. III.2.5. Several steps were taken to improve the stability passively. The laser system was covered with a ‘plastic cage’ to avoid airflow on the table. An antireflection coated fused silica window was installed between the laser room and the rest of the transport line to avoid airflow caused by temperature gradients and a solid metal pipe installed to transport the beam down to the covered VC table. Installation of the fiber booster amplifier and image relay of the fiber output caused further improvement. A summary can be seen in Table III.2.1.

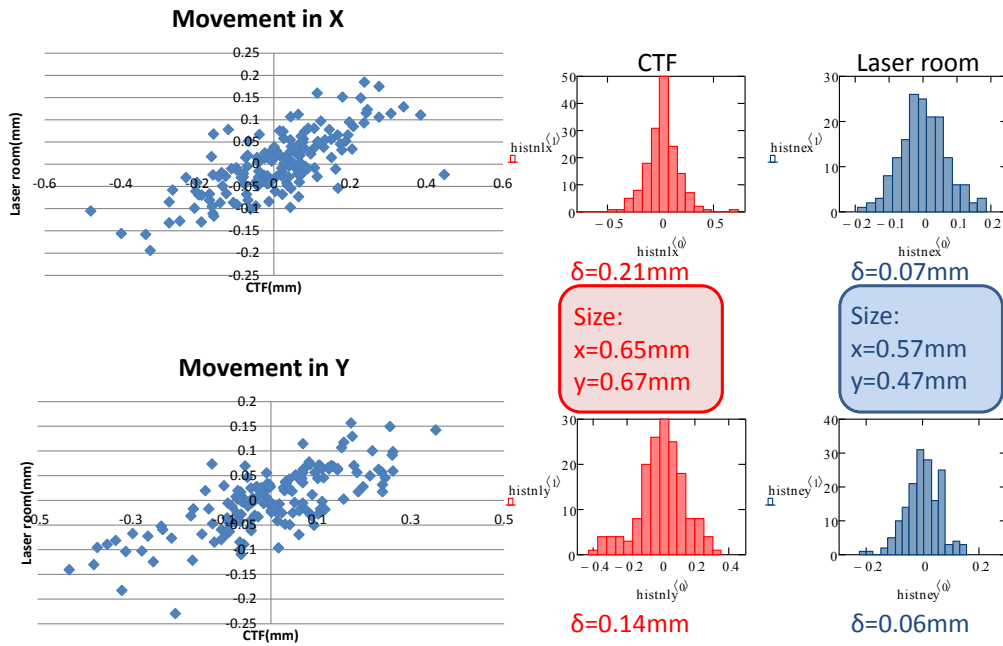


Fig.III.2.5. Virtual cathode beam diagnostics for the PHIN system

Table III.2.1.: Improvement of beam pointing stability with the installation of passive stabilizing elements.

mm	June 2010 no cover	Feb 2011 HighQ booster and cover	Feb 2011 fiber booster and cover
Size x	0.65	2.76	0.344
δ movement	0.21 (32%)	0.74 (27%)	0.067 (19%)
Size y	0.67	2.73	0.524
δ movement	0.14 (21%)	0.87 (32%)	0.079 (15.2%)

Further improvement would be possible with active stabilization, where quadrant detectors and piezo controlled mirrors together with a closed loop feedback could control the position of the beam on the cathode.

III.2.4 Amplitude stability measurements

Apart from the laser amplitude stability, the stability of the power both in terms of phase and in terms of amplitude will also affect the charge stability of the electrons. A typical measurement of the RF quality shows about 0.3% rms variation of the RF power, which has a linear effect on the charge and 0.4° rms variation of the RF phase, which will result of a sinusoidal dependence on the charge. When the machine is operated for best emittance the phase is 30° off crest, meaning 30° off the top of the sine wave, where this dependence can be approximated as linear. Apart from these effects the laser energy stability is one of the main contributors to the charge stability. Stability both integrated over the pulse train (laser)/ pulse (electron beam) and also along the train/pulse has been investigated and the measurements are summarized below.

III.2.4.1 Pulse to pulse stability

The best stability measured for PHIN with the electron bunch is shown on Fig. III.2.6. This was recorded at the same time as the energy measurement for the laser on Fig III.1.21, showing 1.3% rms variation of the laser amplitude. The charge was more stable with 0.8%rms stability, which can be explained by the fact, that the charge production was saturated due to the usage of small beam on the cathode (0.3mm sigma). Typically this regime is to be avoided, as it can cause faster degradation of the cathode.

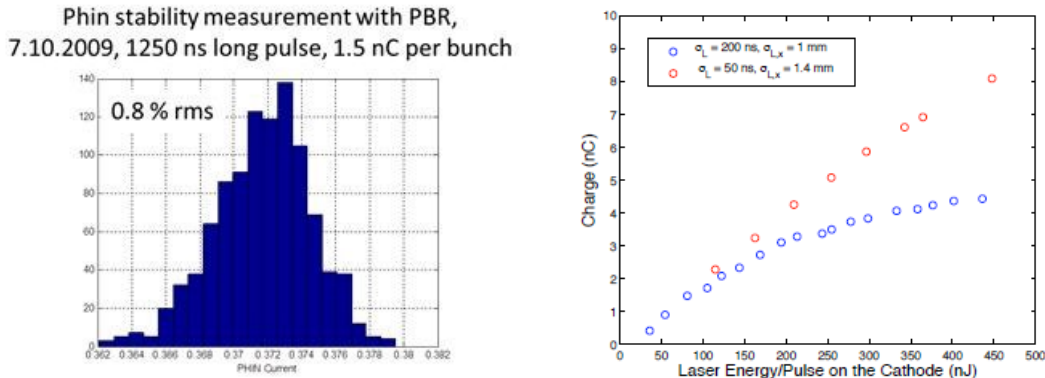


Fig. III.2.6. Beam charge measured with BPR over 1500 shots (left), saturation of the charge with small beam and linear behaviour with larger beam (right)

III.2.4.2 Intrapulse stability

Intrapulse stability variations are also important, so the full beam can be efficiently transported and that energy, emittance of the beam are preserved during the train. As I suggested before, by installing a hard aperture downstream from the harmonics crystals and imaging this onto the cathode we can achieve better beam pointing stability. However, when this aperture was also used to change the beam size amplitude, a variation, depending on the transverse position of the aperture across the laser beam, distortions of the pulse train was observed (Fig. III.2.7.). This has important implications to the amplitude stabilization.

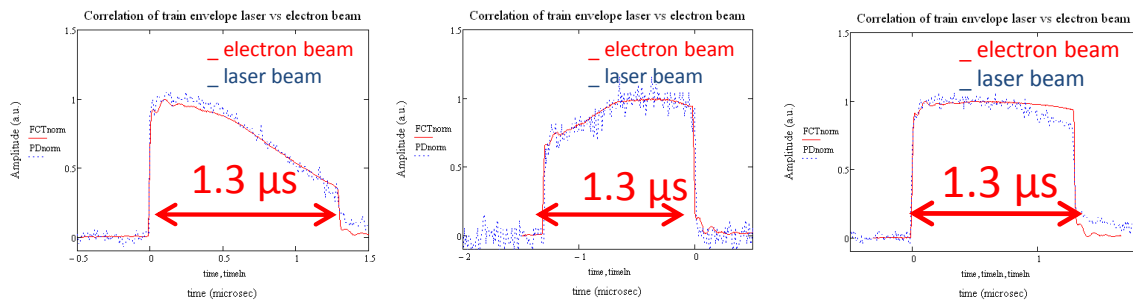


Fig. III.2.7. Beam current measured with FCT after the gun together with laser energy on DET10A Thorlabs PD in the laser room. Small hard aperture was installed to monitor the evolution of the pulse train at different transverse parts of the laser beam. Centre of the beam (left), edge of the beam (middle), all beam (right).

Strong thermal lensing due to UV absorption in the KDP crystal is a suspect to produce such effect. This will cause phase-matching conditions to change over the train at different cross-sectional parts of the beam. It also seems, that this effect is accumulated from pulse to pulse of the laser and so

further investigation of the long pulse-train production in the UV was started, but is outside the scope of this thesis.

III.2.5 Conclusion

I have improved the pointing stability of the laser by using passive stabilization, including image relay system, isolation of the beam from airflow and the installation of a fiber front-end laser. A summary of the measured stability is listed in Table III.2.2. The installation of the hard aperture, which was imaged to the cathode, was not practical to use for this purpose, as amplitude variations along the train were observed due to thermal lensing effects in the harmonic crystals. Active stabilization could improve pointing stability further in the future. Amplitude stability of the electron pulse was measured down to <1% rms stability over 1500 shots, which is excellent for a high power UV laser driven machine without the use of any active stabilization on the laser or the RF.

Table III.2.2: Summary of amplitude and pointing stability measurements during the summer 2010 run showing best, worst and typical values.

Date	Laser position/size		Electron beam position/size				Amplitude stability			Train (ns)		
	Size (mm)		Movement (mm)		Size (mm)		Movement (mm)		Laser energy on cathode/ micropulse (nJ)		Current (nC)	Corr. magnet
	x	y	δx	δy	x	y	δx	δy				
07/10 12:10	0.72	0.66	0.18	0.2	1.04	1.24	0.65	0.57	320 1.66%	1.3 -	ON	1250
07/10 19:20	0.74	0.64	0.15	0.13	1.46	1.76	0.6	0.65	369 1.3%	1.5 0.8%	OFF	1250
16/10 11:55	0.71	0.67	0.24	0.27	1.55	2.86	0.71	0.67	330 2.6%	1 2.4%	OFF	1300

III.3 Two-photon absorption measurement of non-linear crystals

I have carried out the measurement with a sub-picosecond KrF laser provided by the Department of Experimental Physics, Szeged with long history of high power excimer laser development. Four different samples were used during the measurements. CLBO 14mm 61.5°, KDP 15mm 41°, BBO 5.3 mm 22.9°, LTB 5mm 31.9°. The BBO crystals were grown at the Research Institute for Crystal Physics, Budapest, Hungary, by the top-seeded solution growth (TSSG) method from a $\text{Na}_2\text{O} \cdot \text{BaB}_2\text{O}_4$ - BaB_2O_4 solution, while the CLBO and LTB single crystals were pulled from stoichiometric melt by the Czochralski method. The KDP crystal was taken out from the frequency converter unit from a Quantel Nd:YAG laser.

III.3.1 Experimental setup

The experimental setup is shown in (Fig.III.3.1.). The 2 cm x 3 cm flattop beam at 248nm, and the 650 fs long pulses have a 10mJ maximum energy^{III.13}. A homogeneous part of the beam was selected using a circular aperture. I have used fused silica dielectric mirrors for splitting the beam and sending it to the sample to avoid TPA in the beam splitter itself. To measure the beam size the plane of the input surface of the crystal was imaged onto a CCD camera (Fig. III.3.1.).

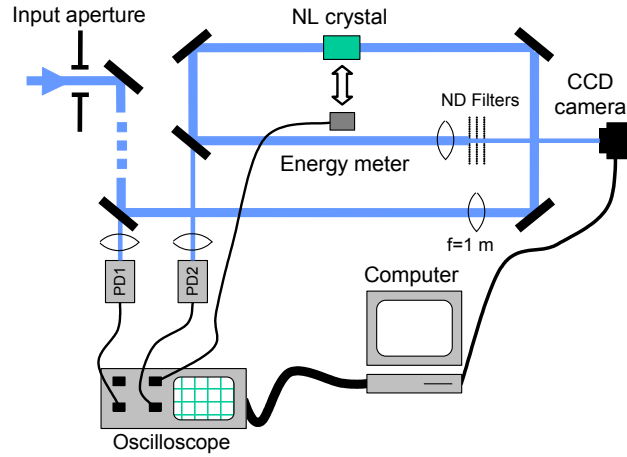


Fig.III.3.1.: Setup for measuring TPA of long crystals by energy-transmission

The first photodiode PD1 was calibrated to an energy meter (EM LaserProbe Rm3700) placed at the sample position. The photodiode PD2 was calibrated to PD1 by measuring the same pulse on both photodiodes (homemade). The photodiodes were kept at their linear working regime by using additional filters and repeated calibration for each filter set. The fast oscilloscope working in peak detection mode picks up the signals of both PD1 and PD2 and transfers them to the computer via GPIB and a LabView routine collects dataset.

III.3.2 Measurement results

A MathCAD program calculates the theoretical fit to the retrieved data, which is proportional to the transmission through the sample, while taking into account the Fresnel-reflections from the crystal surfaces, Airy diffraction image of the flat top beam in the focus, linear and nonlinear absorption and also the saturation effect in the absorption.

In our case the solution of eq. II.54. is derived at the output of an L long crystal assuming temporally Gaussian beam leads to the expression of intensity transmission for modeling purposes:

$$T = \frac{(1-R)^2 \cdot \exp(-\alpha \cdot L)}{\sqrt{\pi \cdot q_0}} \int_{-\infty}^{\infty} \ln[1 + q_0 \cdot \exp(-x^2)] dx \quad \text{III.10}$$

$$q_0 = \beta \cdot (1-R) \cdot I_0 \cdot L_{eff} \quad \text{III.11}$$

$$L_{eff} = \frac{1 - \exp(-\alpha \cdot L)}{\alpha}, \quad \text{(a,b)}$$

where where R : Fresnel-reflection at the interface of the material with air I_0 : peak on-axis intensity of the incident light, L : length of the crystal, x : time-related parameter (as defined in eq.II.10).

Beam profiles were recorded to verify the presence of TPA as well as to provide the correct beam shape as an input for the analysis of the data. The pictures in Fig.III.3.2. were taken by using an aperture significantly smaller than the size of the beam and focusing with a long focal length lens. The 1st picture shows the beam-profile close to the focus, the second is an image of the same plane, but

with the KDP crystal placed in the beam path, and the one on the right shows the same, when the energy in the beam is significantly increased. The one on the right shows the change of the contrast between the main peak intensity and the ring's intensity. Two-photon absorbers are successfully used in UV laser systems, for smoothing the beam-profile, and decreasing the noise in the beam, if one can afford the losses introduced during the process^{II.58-II.59}.

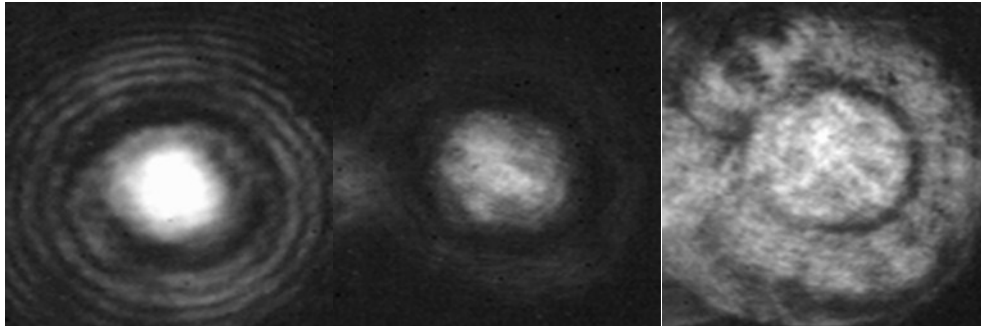


Fig. III.3.2. Input beam profile (left), output beam profile at low intensity(middle), output beam profile at high intensity(right)

For each crystal three sets of measurements were performed each with different incident energy regions, and sampled over 500 measurement points. Please note that the intensity range in the measurement extends from 0.2 GW/cm^2 to 90 GW/cm^2 , which is significantly larger than in the earlier experiments. The large variation was achieved by changing the exciting voltage of the KrF excimer amplifier. Smaller variation was given by the 20% shot to shot variation of the laser energy. The values of linear absorption were determined from the transmittance measurements at extremely low intensity. This was supported by a linear absorption measurement using a Shimadzu spectrophotometer and the results are shown in Table III.3.1. The reflectivity at the surfaces was calculated from the Fresnel formula using the appropriate refractive index polynomials.

The curves of the measured and fitted transmission are shown in Figure III.3.3., while the results and crystal data are listed in Table III.3.1.

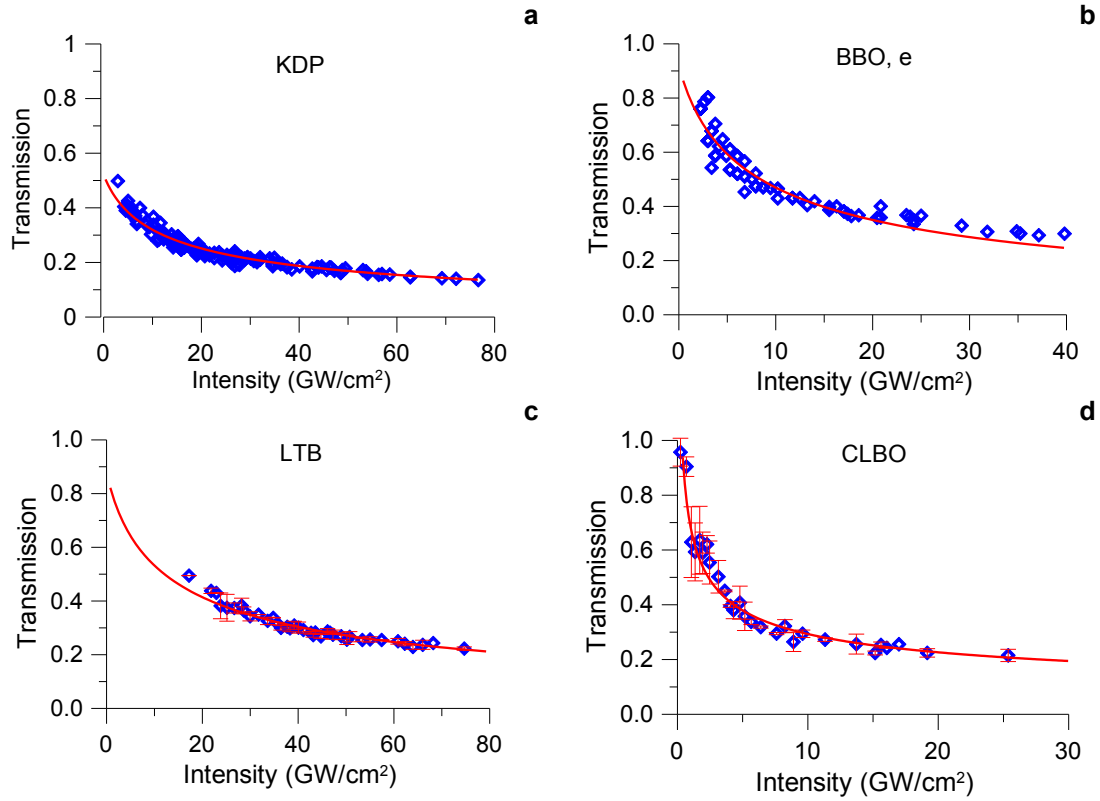


Fig.III.3.3. Measured and fitted nonlinear transmission for KDP (a), BBO (b), LTB (c) and CLBO (d).

One can see that the TPA coefficient for the KDP crystal is in a good agreement with the data found in the literature. Similarly to Ref. II.65 we found that the TPA coefficient of BBO depends on the polarization. The main values of our experimental data are, however, slightly smaller than the previously reported values. On the ground, that the absolute nonlinear coefficients were also found to be different for crystals grown using stoichiometric and non-stoichiometric procedures, we think that this slight difference of β in favour of our BBO sample may be resulted in the different crystal growth methods.

Table III.3.1. Measured TPA-coefficient at 248 nm for different crystals

Crystal	Length [mm]	Cut(θ)	α [cm^{-1}]	Measured β [cm/GW] at		
				248 nm	264-266 nm	211-216 nm
KDP	15	41°	0.23	0.48±0.06	0.26 - 0.27 [II.63],[II.62]	0.6 – 1.36 [II.63],[II.60]
BBO	5.3	22.9°	0.05 0.09	0.50±0.12 (o) 0.34±0.09 (e)	0.47 - 0.93 [II.63],[II.64],[II.65]	2.43 [II.63]
LTB	5	31.9°	0.01	0.22±0.03	-	-
CLBO	14	61.5°	0.02	0.53±0.12	-	-

III.3.3 Conclusion

The two photon absorption coefficient of 5 mm - 15 mm long BBO, CLBO, KDP and LBO samples was determined from the measurement of intensity dependent transmission at 248 nm. The theoretical fit to the experimental results show a TPA value of 0.48 cm/GW, 0.5 cm/GW, 0.34 cm/GW, 0.22 cm/GW and 0.53 cm/GW for KDP, BBO (o-ray), BBO (e-ray), LTB and CLBO, respectively. These values were measured for the first time for LTB and CLBO crystals, providing a good reference when choosing conversion or OPA crystals for high intensity applications in the UV regime.

III.4 Phase-coding development for photo-injector laser system

The requirements for the phase-coding were detailed in II.2.1.4, a summary of the available fast optical switches has been given in section II.2.5. Here, I detail the design choice which was made and describe the setup based on fiber optic modulators and detail the measurements, which were carried out for accurate setup of the system and for verification both on the laser and on the electron beam produced by it.

III.4.1 Design considerations and the final setup

The specification of the phase-coded train is listed in Table II.2.7. In the past, a system based on fast-switching Pockels cells at the end of the laser chain had been considered. However, for good transmission at high laser power levels, a ~ 7 kV, ~ 7.1 MHz pulsed driver is necessary, which together with the fast rise and fall times of < 500 ps, is too challenging for the solid-state voltage switches available at present. A possible setup based on Pockels cell is shown in Fig. III.4.1.

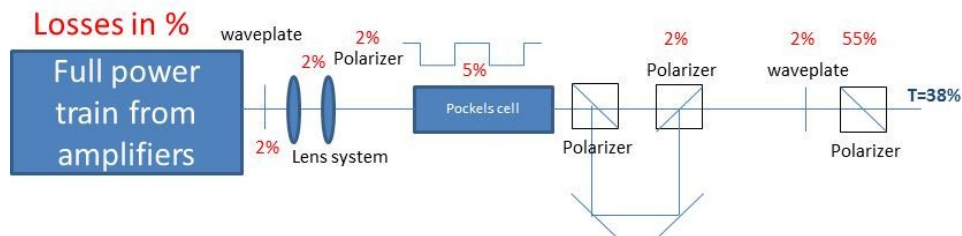


Fig.III.4.1. Possible Pockels cell based phase-coding setup in the infrared

High bandwidth, 10GHz, LiNbO₃ modulators are available at the laser's 1047nm wavelength. This speed ensures the fast rise time necessary for the application. However, LiNbO₃ suffers from photorefractive damage, and at 1 μ m power levels are limited to 100mW average power. Depending on the manufacturing process, each modulator will have a different damage threshold, which is estimated to be ~ 4 W peak power in pulsed operation. To achieve a high extinction ratio, stable active control of the operating point (bias voltage) is necessary. To compensate for the drift of the operating point, several feed-back loops techniques can be implemented. Photline proposed the MBC-1000 Modulation Bias Controller that locks the operating point of the modulator at a user selected position. The principle relies on applying a low frequency tone signal to the DC electrodes of the modulator and

analysing the modulated optical output power. The frequency and amplitude of this modulation has to be set right for the operating point (QUAD+/-) and will depend on the time-structure of the produced signals. In addition, special attention must be given to the driving electronics to reach the required power stability of the resulting optical signal. For our purpose an AC coupled driver DR-PL-10-MO-LR was purchased from Photline to achieve flat pulses over the required period, with adjustable gain. At low power, LiNbO₃ modulators are expected to have a 20-year lifetime under laboratory conditions, and the small physical size of the modulator ensures that there is no additional jitter to the timing of the laser.

Therefore, a LiNbO₃ fiber optic modulator was chosen as the switching element for the phase-coding setup. To comply with maximum input power constraints, it was installed after the laser oscillator, where the pulse energy is lowest. The two modulator scheme implemented is shown in Fig. III.4.2. The light leaving the 1.5GHz mode-locked oscillator is coupled into a single-mode polarization maintaining fiber splitter. One arm contains a variable delay line (Ozoptics, ODL-300), consisting of an input and an output collimator, and free-space manually adjustable delay which providing the total delay of 333ps delay to the second arm (180° degree phase shift at 1.5GHz). The second arm contains a variable attenuator (Ozoptics BB-700) to match the total attenuation in the delay arm. The modulators (Photline Techn. NIR-MX-LN-03) use the same drive signal, with separate voltage amplifiers for working point adjustment and are driven in 0% to 100% transmission mode in one case and 100% to 0% in the other. The output of the modulators is then added using a non-polarizing beam splitter in reverse. This results in a signal in which every second sub train is delayed 180° in phase (333 ps in time) as shown in Fig.2. The transmission of the setup was 1.5%, and mainly limited by losses on injection to the fiber, splitters and connectors used for its assembling. The signal is then amplified to 200mW using a fiber amplifier (Fianium FPA-320mW) to bring the power level back to the oscillator's level, and is then coupled back into the rest of the laser chain (Fig.3.).

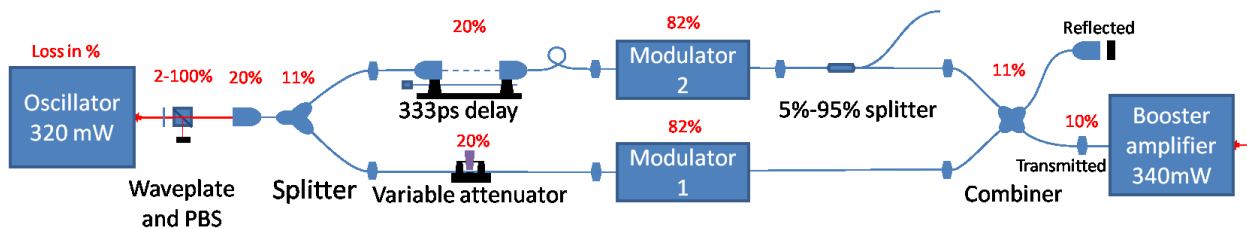


Fig.III.4.2. Two-modulator based scheme with measured losses

The two-modulator scheme is safe against power damage. Lossy elements, such as the fiber splitter, attenuator and the delay line can be placed before the modulators. Furthermore the power is split in between the two modulators. This way full power of the 320mW oscillator can be utilized without risking stepping over the 100mW safety limit for the modulators. As the total delay introduced is only 333ps between the two arms, sensitivity to temperature changes is very small, well below the requirement. The fiber oscillator purchased from Fianium provides amplification back to the oscillator power level of 320mW and includes an active feedback stabilization system with ~100μs response time to ensure constant output power by adjusting the pump current. Amplitude stability

measurements taken by monitoring the mean value over the 500 microsecond 'amplification window' for the laser chain and over 215 shots using Thorlabs DET10A show < 0.1% rms amplitude stability.

The required RF modulating signal to drive the modulators was produced by a custom made electronic circuit designed at CERN. A low phase noise 1.5GHz beam synchronized signal was provided and capacity coupled to an 8 bit programmable ECL counter (MC100EP016F). The counter is followed by a D flip flop (MC100EP31DG). These circuits together allow the selection of a pulse length within the required range (140ns) and the terminal count output connected to the D flip flop creates the required square wave signal. The signal is only delivered for the amplification window of the burst mode amplifiers (AMP1, AMP2) to allow resynchronization between each burst. The electronics box also includes AC amplifiers (DR-PL-10-MO-LR) which provide the fast rise times necessary and also dampen variations on the driving voltage. With the 300ps accuracy of the switching, cutting between two consecutive pulses can be easily ensured by choosing the right cable length between the output of the driver box and the modulators.

III.4.2 Amplitude and timing accuracy

A measurement method was needed to provide easy, accurate and preferably online measurement of the timing difference and the amplitude balance between the sub-trains produced in the two arms of the setup.

Photo-diodes provide fast and accurate measurement for both. Our highest bandwidth photodiodes are the fiber-coupled New Focus 1024 with an impulse response of 12ps FWHM and the New Focus 1014 with a 3dB bandwidth of 45GHz. The New focus 1024 is optimized for time domain measurements and the 1014 is optimized for frequency domain measurements, however they were both found to be well suited for both applications in this case, although the 5.5ps laser pulses cannot be fully resolved by these detectors.

While the delay can be roughly set using the digital oscilloscope LeCroy Serial Data Analyser SDA18000 (18GHz, 60 Gsamples/s), this does not provide an accurate measurement, because of the timing jitter of the trigger signal and the digitization itself. Furthermore the oscilloscope has nowhere to trigger on a balanced train as the sub-trains are indistinguishable, thus a single trace has to be recorded and post-processed, which can be very tedious. Post analysis provides an accurate evaluation of the timing switch, but is not suitable for a fast setup.

It is possible to check the output signal in the frequency domain. The Fourier transform of the oscillator pulstrain consists of spectral lines at multiples of 1.5GHz and of course at DC. If a part of this signal is phase shifted, other frequency components also appear, depending on the sub train length. When no drive voltage is applied to the modulators a continuous 3GHz signal will be created after recombination of the two 1.5 GHz arms with half of the nominal amplitude due to the QUAD (50%) working point of the modulators.

The electric field of the pulse train, which gives the sum of the envelope function of each pulse E_p with unit amplitude, can be defined as:

$$E(t) = \sum_{n \in \mathbb{Z}} E_p(t - n\tau), \quad \text{III. 12)}$$

where τ is the period of the signal. $\tau=1/f_{rep}$. As the condition length of the $E_p(t)$ laser pulse $< \tau$ is satisfied, the Poisson summation formula can be used to determine the spectrum:

$$\sum_{n \in \mathbb{Z}} E_p(t - n\tau) = 1/\tau \cdot \sum_{m \in \mathbb{Z}} S_p(m/\tau) \cdot e^{2\pi i m t / \tau}, \quad \text{III.13)}$$

where $S_p(f)$ is the Fourier transform of $E_p(t)$. Hence, the spectrum of this signal will consist of a comb spectrum, where each line is an integer multiple of the repetition frequency (f_{rep}). When two functions described in (III.1) are added with different amplitude, a_1 and a_2 , and a delay of d , an additional term will appear in (III.2). By substituting $2\pi d/\tau = \phi$, the phase-difference between the pulse trains at $f_{rep}=1.5\text{GHz}$ (2) will be multiplied by:

$$(A_1 + A_2 \cdot e^{-i\phi \cdot m}), \quad \text{III.14)}$$

where A_1 and A_2 are linearly proportional to the electric field amplitudes a_1 and a_2 . When calculating the resulting spectral amplitude variation with A_1 and A_2 and ϕ at different values of m , we get:

$$\sqrt{(A_1 + A_2 \cdot \cos(m\phi))^2 + (A_2 \cdot \sin(m\phi))^2}. \quad \text{III.15)}$$

If amplitudes were exactly matched, $A_1=A_2=A$ (4) becomes

$$A \cdot \sqrt{2} \cdot \sqrt{1 + \cos(m\phi)}. \quad \text{III.16)}$$

From here we can easily see that at odd multiples of the f_{rep} the lines will disappear from the spectrum, while at even multiples of f_{rep} the spectral lines will increase as we approach a perfect 180° phase-shift, corresponding to a clean 3GHz periodic signal spectrum. At different amplitudes of the two signals, however, the odd spectral lines will remain with some non-zero amplitude even at perfect time-delay.

At odd multiples of the 1.5GHz the lines will disappear from the spectrum while at the even multiples of the 1.5GHz the spectral lines will increase as we approach perfect 180° phase-shift, corresponding to a clean 3GHz periodic signal spectrum. At different amplitudes of the two signals however the odd spectral lines will remain with some non-zero amplitude even at perfect time-delay. By minimizing the 4.5GHz peak through iteration of time and amplitude adjustment, peak suppression 40-67 dB below the 3 GHz reference was achieved depending on the noise arriving from the oscillator noise on each day. This corresponds to a maximum amplitude error of 1.76-0.044% with maximum timing error of 0.1-0.016 ps. The change of the 4.5 GHz peak by varying delay is shown on Fig.III.4.3. The effect of time delay on the spectrum is greatest if we look at higher multiples of 1.5 GHz, unlike the effect of the amplitude unbalance between the arms. Measured accuracy was limited by the finest

adjustment possible manually in the delay and attenuator arm and shows that with stable input source phase-coding scheme can provide accurate settings well within specification.

The frequency domain method is capable of setting the delay and amplitude balance to accuracy significantly better than 0.1 ps and 0.1%, and can be achieved due to the high dynamic range of the spectrum analyser. A great advantage of this measurement method is that noise, such as detector noise, generally increases the measured peak and thus makes our calculations of maximum amplitude balance and delay error conservative.

There is however still some limiting factors remaining:

- Fluctuation of the measured peak due to noise from the laser oscillator limits the accuracy.
- Modulators have to be turned off, this can cause drifts of the working point and so for amplitude error measurement between the arms the time domain method is preferred.
- The attenuation drift of the in fiber attenuator was a major problem. As the measured peak has drifted accuracy for setting the timing goes down. This was solved by changing to the variable neutral density attenuator wheel.

III.4.3 Integration into the laser system

The scheme was planned such that the oscillator output provides the input for the phase-coding after which the losses are recovered by a fiber booster amplifier. The output is then to be amplified with a HighQ preamplifier to 10W and then the high power amplifiers as in the original system. However, the preamplifier was not available at the time and so direct amplification of the low power booster amplifier was done in AMP1 and AMP2. Tests were done on the AMP1&2 stages to find out how much energy per pulse we could expect, if we reduce the input to AMP1 and AMP2 from the usual 7W to 250mW (including losses between the fiber output and the APM1 input.)

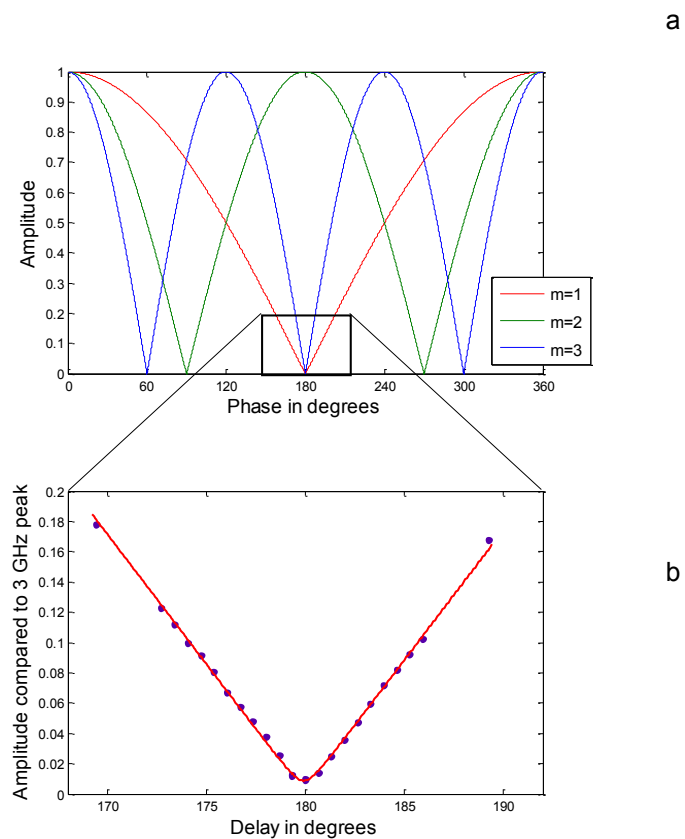


Fig.III.4.3. a) Expected variation of the spectral line relative to the peak at different frequencies with perfect amplitude balance; b) Amplitude of the 4.5GHz peak respect to the 3GHz main peak with fit including amplitude error

Close to the nominal 350nJ per pulse was still achievable with these parameters, as show in Fig.III.4.4. Several other modifications were necessary to the laser system to accommodate for the phase-coding setup:

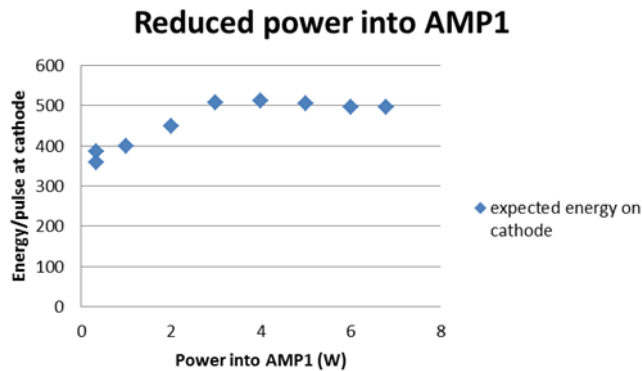


Fig.III.4.4. Expected energy/pulse (nJ) on the cathode with reduced input power to the amplifier chain.

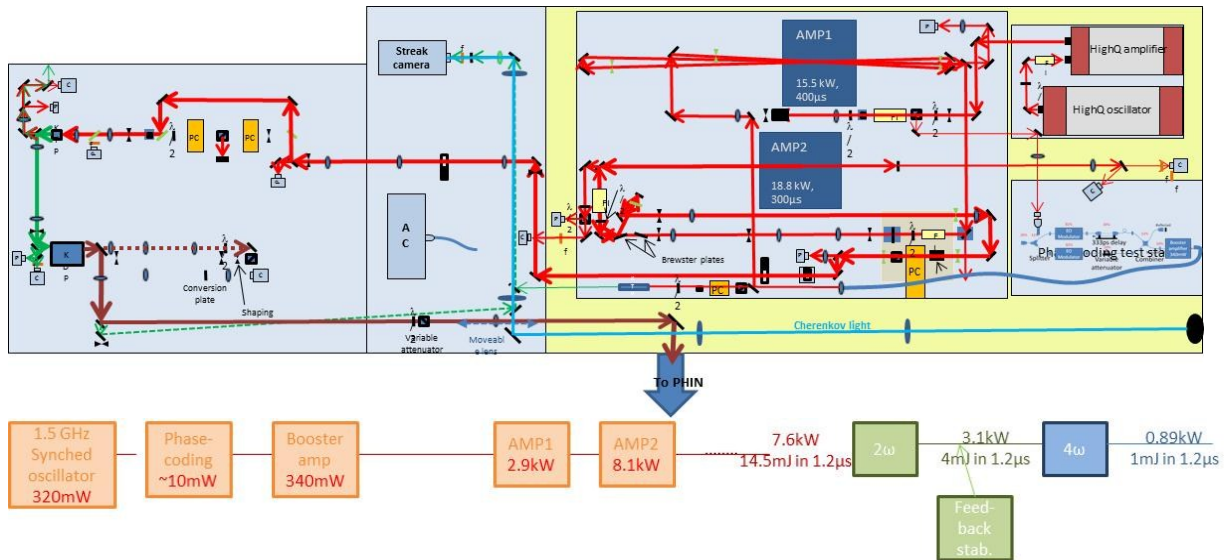
- As power of the oscillator was not sufficient to drive the phase-coding without the booster amplifier, part of the HighQ pre-amplified beam had to be coupled into the fiber.

The final setup is shown in Fig III.4.5. The beam was amplified to 1.7kW mean power after AMP1 with 90A pump current, corresponding to 1.1μJ per pulse. However, strong over-pumping was observed and so pumping time of AMP1 was reduced to 250μs from the original 400μs. The mean power in this case was 1.6kW. Conversion was checked to see the ASE content of the signal. 30% conversion efficiency to green was measured and confirmed clean amplification. For AMP2 the pumping time - following the change on AMP1- was reduced to 200μs. 9.4kW meanpower was measured this way with excellent beam profile after AMP2. This corresponds to 6.3μJ/ pulse at the exit of the PC.

- The interlocks had to be modified to make sure AMP1 and 2 turn off in case of failure to the booster amplifier.

- The output of the booster amplifier had to be matched to the rest of the laser chain both in power and in size.

- The amplification of the phase-coding had to be confirmed at several stages around the system, and so beam-passes had to be created to send the beam to the streak-camera station.



Legend:

- Mirror
- Lens
- Halfwave plate
- Faraday isolator (or part)
- Polarized beam splitter
- Pockels Cell
- Power meter
- Periscope
- Camera
- Photodiode
- Shutter
- Filter
- Optional iris
- Optional mirror

Fig. III.4.5. Setup of the laser system including optional beam passes for measurements to analyse the phase-coding setup.

Fig. III.4.6. shows the improved output profile with the excellent input beam quality from the fiber amplifier. Although mean power levels at the time of the PC switching are comparable with the higher seed input to AMP1 and AMP2, reduced pumping time results in slower build-up of the steady state. Even so the amplitude stability of the booster seed is higher, than that of the HighQ preamp, we benefit less from the stabilizing effect of the steady-state saturated amplification. In this case. 0.6% RMS stability was measured in the IR, which is only slightly above the 7W seeded case, where 0.35% was the typical value. With no additional adjustment made to the lens systems in the harmonics stages 710 nJ/ pulse was obtained in the UV, which given a

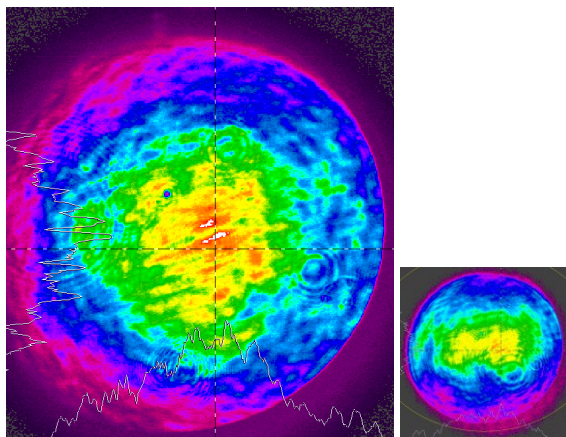


Fig. III.4.6. Beam profiles after AMP2 with booster amp input at 140mW at AMP1 (left) and with previously used HighQ 7.4W input (right), with same attenuators in front of the camera.

Even so the amplitude stability of the booster seed is higher, than that of the HighQ preamp, we benefit less from the stabilizing effect of the steady-state saturated amplification. In this case. 0.6% RMS stability was measured in the IR, which is only slightly above the 7W seeded case, where 0.35% was the typical value. With no additional adjustment made to the lens systems in the harmonics stages 710 nJ/ pulse was obtained in the UV, which given a

maximum of 450nJ/ pulse on the cathode is well above the 370nJ specification. Conversion efficiencies of 38% and 27% were measured to green and to UV respectively.

III.4.4 *Electron beam diagnostics*

Measurements on the electron beam were performed to verify the switching performance of the system. A detailed description of the beam diagnostics (Fig.III.4.7.) and the measurements during commissioning of the machine without phase-coding can be found in references III.10. and III.17.

A fast current transformer (FCT), installed directly after the gun, is used to monitor the extracted charge. This provides a good tool to check phase- and amplitude errors between sub-pulses. The phase error and amplitude imbalance between the laser's sub-pulses appear as a current imbalance between the sub-pulses of the electron pulse.

A dedicated Cherenkov-line was built to deliver photons back to the laser room. A 300 μ m aluminium-coated sapphire Cherenkov-target is used, which generates a larger flux of visible photons compatible with the sensitivity of the streak camera. The electrons which propagate through the plate produce photons both at the entry and the exit surface with a time delay, which is proportional to the relative speed of the electrons and the photons in the material and also to the thickness of the plate. With 2mm sigma electron beam size measured at the focus in PHIN one would expect 11ps time resolution from the plate. The number of photons produced and detected will depend on the electron energy, the thickness of the plate, the spectral range observed and also the transverse and angular acceptance of the streak camera. We are expecting $\sim 5 \cdot 10^{-3}$ photons/electron to arrive to the streak camera, which with the 2.3nC nominal charge should be easily visible. However, we have found that to have enough photons on the streak camera for single bunch measurements the smallest bandwidth filter which could be used to improve resolution was ~ 200 nm, unfortunately this is too broad to significantly improve the resolution. The conclusion is, that the setup is suitable for establishing the bunch separation, but not for precise bunch length measurements.

III.4.5 *Phase coding measurements*

Verification of the switching was first necessary on the laser system. It was also important to understand how long term drift would affect the quality of the pulsetrain delivered in the UV and finally to the photo-injector. Comparative measurements between the sub-trains were carried out to check, that basic parameters of the electron-beam were not affected by the phase-coding.

III.4.5.1 *Contrast and timing measurements*

As the final laser wavelength to the cathode is at the 4th harmonic of the phase-coding wavelength, even an extinction ratio as poor as 0.1 would provide the contrast required in the ultraviolet (<0.01), due to the nonlinearity of the conversion process. Extinction ratios of less than 1:300 were measured in the IR, where accuracy was limited by the noise floor of the system (Fig.III.4.7.). When a bias drift occurs in the modulators, the extinction ratio between the ON and OFF

state deteriorates. This was of particular interest for the long term reliability and stability of the system. In this case the ON state signal will drop and in OFF state there will be pulses leaking though as shown in figure II.4.8. resulting in satellites between the required electron bunches.

As there was no active stabilization used for the bias this time, we were interested to see how these bias errors affected the amplification and later the conversion and electron production. A bias error larger than expected from temperature drifts was introduced (1.5 Volts), causing satellites at ~20% level (Fig. III.5.9.). For illustration the other modulator was kept in a perfect switching state and amplitudes were set to be equal in both arms for the main pulses. The satellites on the relative slow detectors will appear as a DC error in the other sub-train. These pulses are conserved and amplified with the same gain as the main pulses. However, as these pulses contain a very small pulse energy relative to the main pulses, then during the two non-linear processes the energy in the UV drop to only ~5% of the main pulses. To be within the specified 4% for CLIC one would have to make sure, that bias drift is kept below 1V, which with the full switching voltage of 5V is reasonable under normal laboratory conditions.

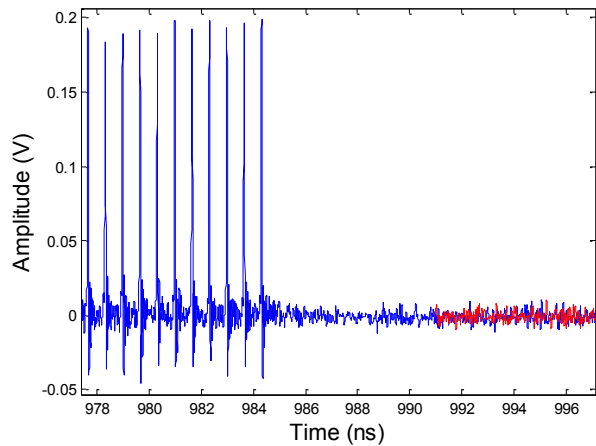


Fig. III.5.7. Switching between 1.5GHz pulses, with noise floor marked in red.

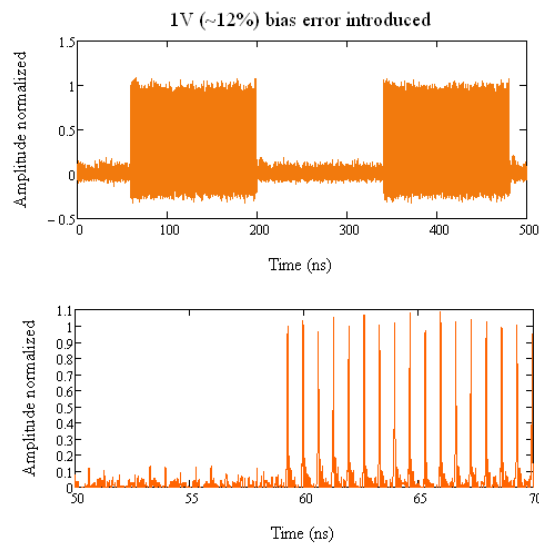
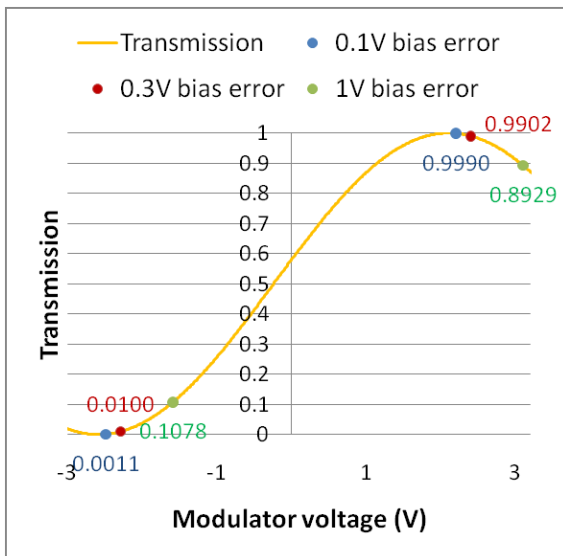


Fig.III.5.8. Bias error measurement. Left: Calculated contrast error between ON and OFF state at different bias errors. Right: Measurements with the fast oscilloscope in the case of 1V bias error.

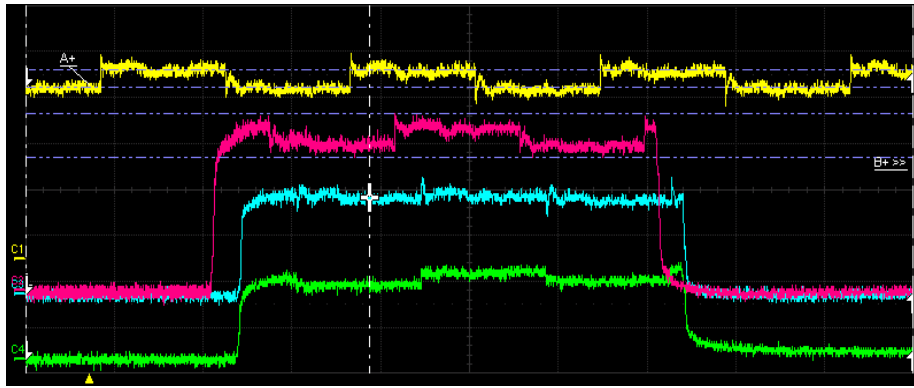


Fig.III.5.9. Bias error propagation measurement. Yellow: Signal after AMP1 and signal after AMP2 with 1.5V bias error, corresponding to 20% satellites introduced. Green: same after second harmonic conversion Blue: Same after 'the harmonic conversion.

Furthermore, measurements using the second harmonic wavelength of the laser sent to a streak-camera were carried out to show, that when bias and delay settings are correct, then the pulse separation is also correct at switching and no satellites are present (Fig.III.4.10.). To carry out the same measurement on the electron beam Cherenkov-radiation was image ralyed back into the laser room onto the same streak camera and results are shown on Fig. III.4.11.

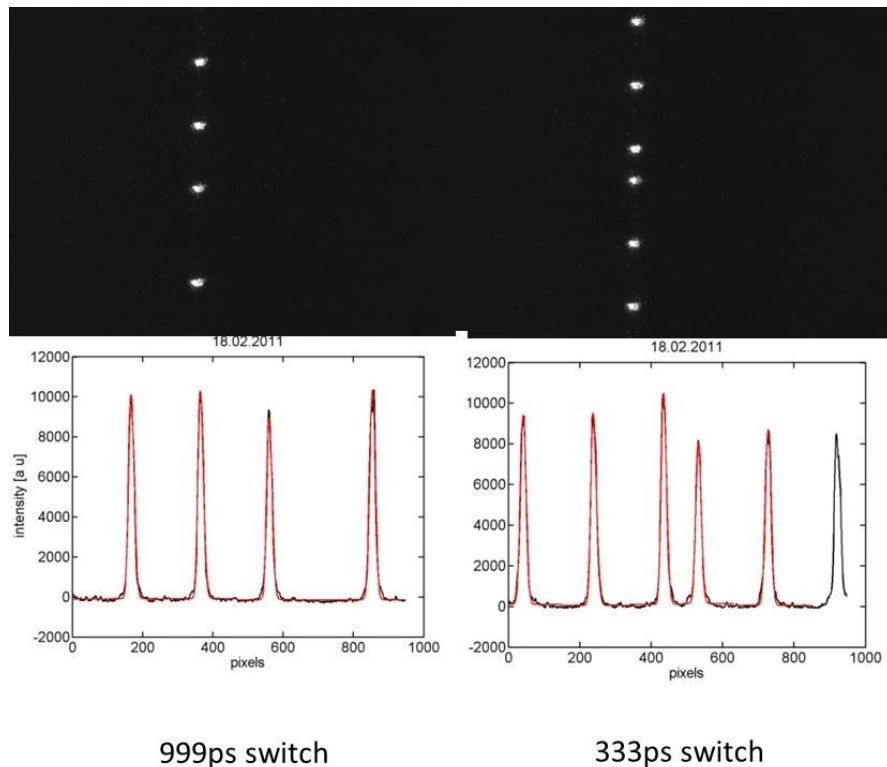


Fig. III.4.10. Measurements performed on the laser system using streak-camera to confirm switching

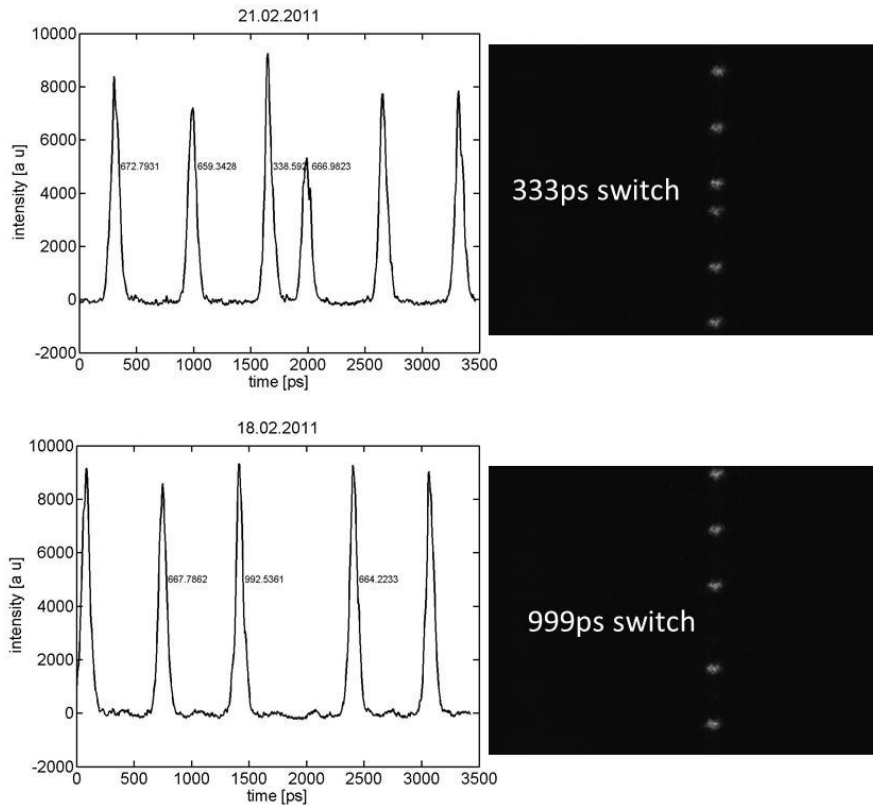
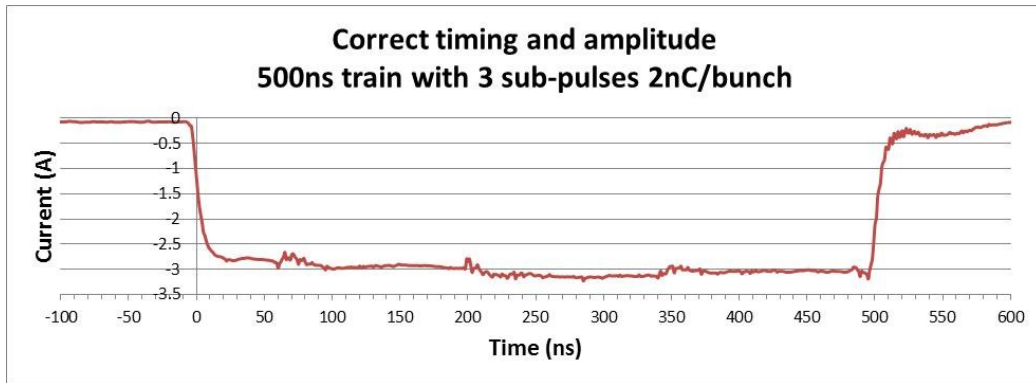


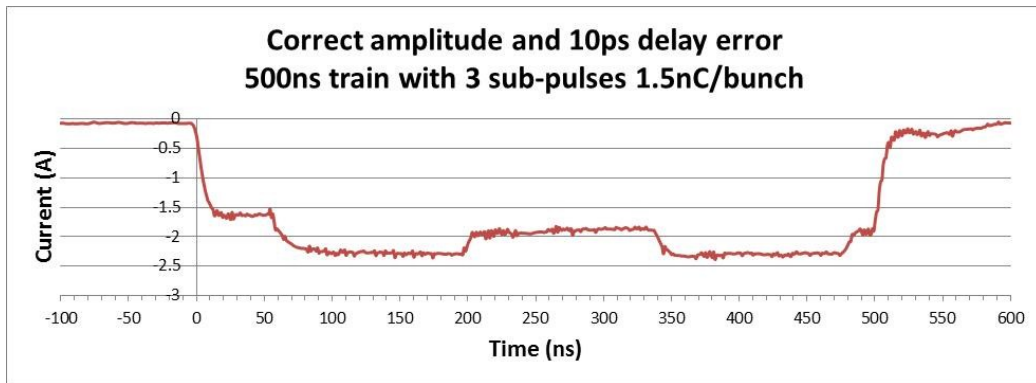
Fig. III.4.11. Bunch separation when switching takes place measured on the streak camera with Cherenkov-light from PHIN

In both measurements taking into account the time resolution of the streak at 250ps/mm sweep speed, the observed bunch separation was within the specification. Amplitude variations over the sub-trains came directly from the laser oscillator.

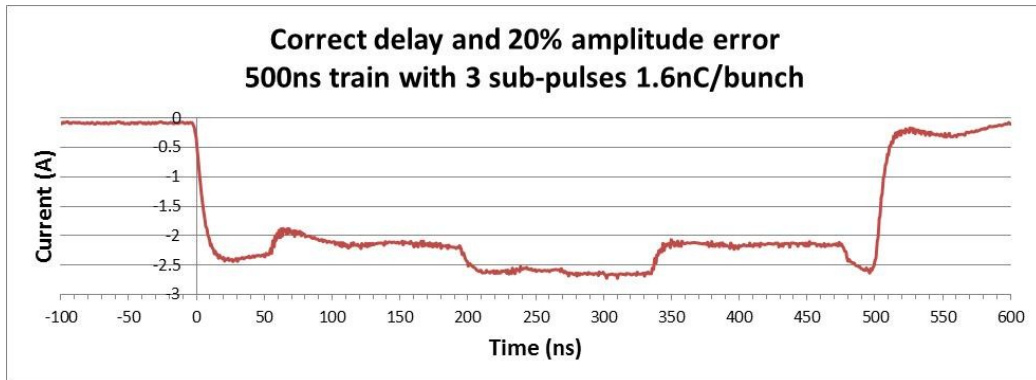
Measurements with FCT were carried out to check the effect of delay error. A 10ps error was introduced in the delay arm of the phase-coding. This resulted in a reduction of extracted charge in that sub-pulse, which appears as a DC change with the 30MHz bandwidth filter on the oscilloscope, Fig. III.4.12. An amplitude error was also produced between sub-pulses to check the sensitivity of the FCT, which was found to be <1%. An example with 20% amplitude error is also shown here.



a



b



c

Fig.III.4.12. Fast current transformer measurements. with (a) $<0.1\text{ps}$ delay error and $<0.5\%$ amplitude error settings. (b) deliberate 10ps delay error introduced to the sub-trains in the phase-coding delay line. (c) with 20% amplitude error introduced to the sub-trains.

III.4.5.2 Measurement of electron beam properties

Beam size and emittance (Fig.III.4.13.) were measured on the first OTR. The gated camera was set to integrate over the centre of each 140ns sub-pulse, with 100ns gate time. No degradation of performance was observed with phase-coding. The nominal charge of 2.3nC in 8 sub-pulses, with 7mm mrad normalized emittance, in a 5.5MeV beam was produced with a phase-coded beam.

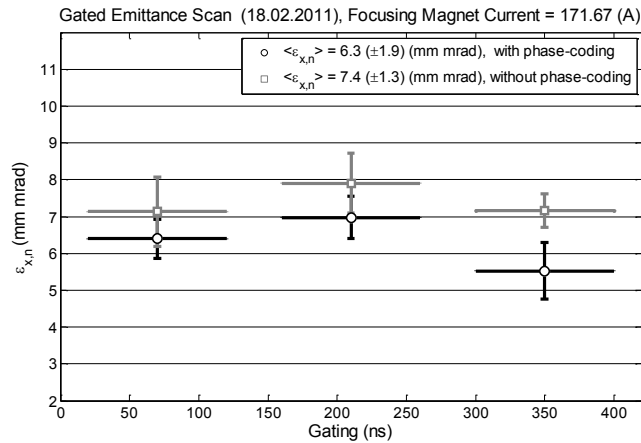


Fig.III.4.13. Emittance measurements over three consecutive sub-pulses using 100ns gating time

III.4.6 Conclusion

I have designed and implemented a phase-coding system for the PHIN laser, which provides the required pulse structure for electron beam combination in CTF3 and for the future CLIC application too. An accurate timing and amplitude balancing system was developed using frequency domain measurements. The phase-switch can be set with 0.1ps accuracy and introduces no additional jitter to the laser oscillator. The amplitude balance between sub-trains can be set to the required accuracy of 0.1% rms, and is currently limited by fast noise of the laser oscillator. Verification of the system was done on the electron beam too, showing that with the laser based phase-coding satellite free, clean switching can be achieved.

In the future, several improvements could maybe be made to the system. To increase transmission through the phase-coding system losses from all the FC/APC connectors could be suppressed by fusing the fiber components together, which would lead to a 20% increase in the output power. An additional fiber booster amplifier, providing 10W input to the burst mode amplifiers, would bring higher saturation levels and, in return, greater stability. Active control of the amplitude balance via a waveplate- and polarizer-based remotely controlled attenuator could compensate for long-term temperature drifts, and would provide a finer and more reliable attenuation. The modulators themselves could be temperature-stabilized to $\sim 40^{\circ}\text{C}$ to ensure that any drift is minimized.

III.5 Temporal contrast of high intensity UV pulses

In a FEL environment short pulse, probe lasers with high temporal quality are required for pump probe experiments. As explained in II.1 and II.2.2.5, the temporal contrast ratio of ultrashort laser pulses is degraded by spectral and phase aberrations caused by spectral clipping or misalignment in the stretcher or compressor. Measurement of the temporal contrast is necessary; however the available single pulse measurement techniques in the UV regime are limited due to the available materials at the second harmonic wavelength. Our aim is to estimate the best achievable temporal contrast from the measured spectrum and with the simplest available pulse measurement techniques.

For instance at what level of spectral intensity (S_c) is necessary to be measured for the knowledge of the ultimate temporal contrast? Understanding the effects mentioned above on the contrast is important for system optimization and to know the tolerances acceptable for the different components.

III.5.1 Modelling results

Initial calculations have been carried out for pulses with Gaussian and sech^2 spectra, the two typical pulseshapes in real laser systems (Fig.II.2.1.). We assume, that $S(\omega)$ spectral intensity of the laser pulse is defined or can be measured to some S_c level. There are two ω_1 and ω_2 cut frequencies corresponding to this level, where $S(\omega) > S_c$, when $\omega_1 \leq \omega \leq \omega_2$, and $S(\omega) = 0$ otherwise. For the calculations we have applied hard spectral clipping at different S_c levels of the corresponding spectral intensity distribution and introduced different levels of spectral phase aberrations in the Fourier transform (eq. III.17.) to obtain the temporal distribution.

$$I_c(t) = \left| \frac{1}{2\pi} \int_{\omega_1}^{\omega_2} \sqrt{S(\omega)} \cdot e^{i\phi(\omega)} e^{i\omega t} d\omega \right|^2 \quad \text{III.17)}$$

III.5.1.1 Effect of spectral clipping

In practice the cut of the spectrum at the level S_c is the equivalent of a “hard” spectral aperture in the dispersive part of the laser system. Fig. III.5.1. shows the spectral distribution the applied cut and the corresponding dispersion free temporal distribution. Contrast was defined as the level of the highest pre-and postpulse in the normalized temporal intensity distribution.

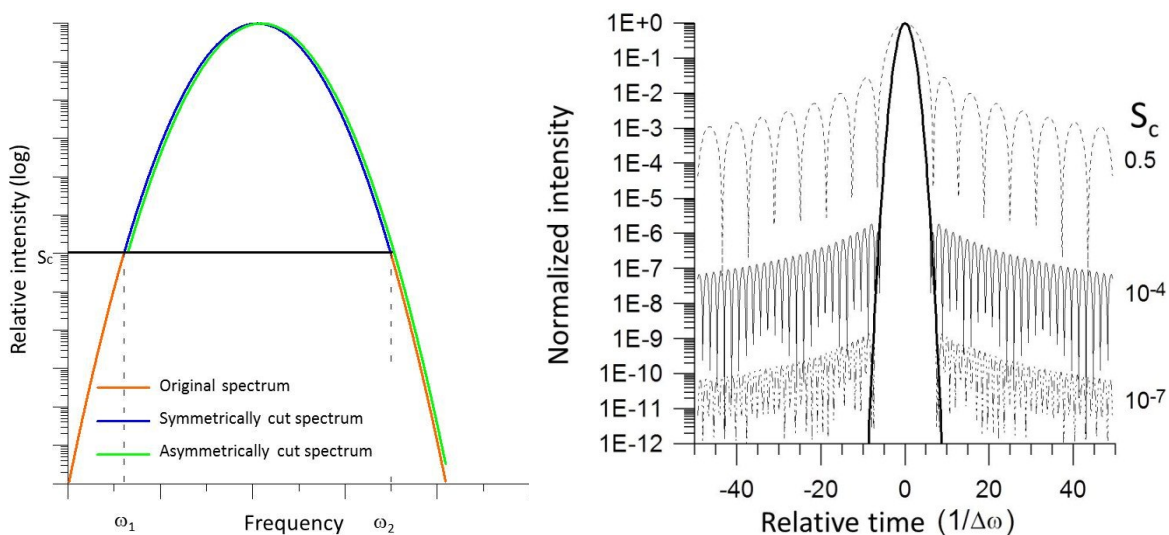


Fig.III.5.1. Definition of hard spectral clipping (left) and the corresponding temporal distribution for a Gaussian pulse in the case of symmetrical cut at different levels of S_c (right)

The contrast as a function of the clipping level is shown in Fig. III.5.2. for both pulse shapes, also detailing the corresponding energy content and relative cut bandwidth compared to the transform

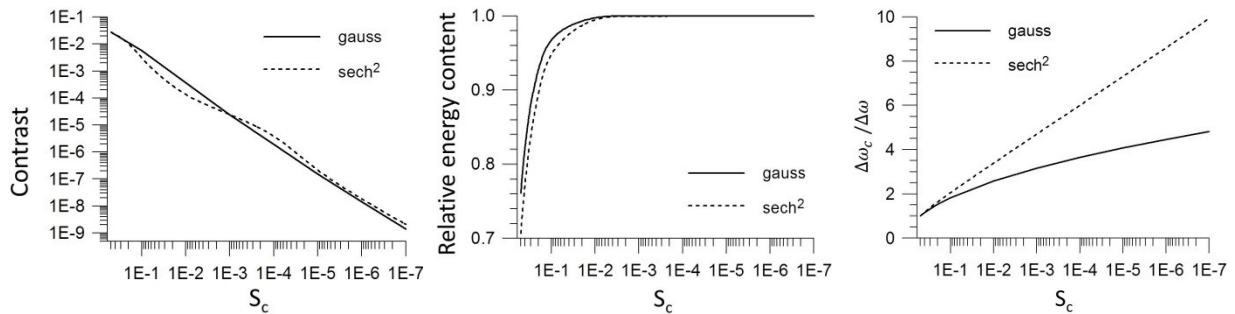


Fig.III.5.2. Contrast as a function of hard symmetrical spectral clipping at different levels of the spectrum (left); the energy content at these cuts (middle); the relative cut bandwidth (right)

limited case. It can be seen that from the knowledge of the pulse spectrum at the spectral clipping (S_c) level, the best achievable contrast can be estimated at an almost two orders of magnitude deeper level ($S_c/50$). For example if the contrast of a sech^2 pulse in a Ti:Sa CPA laser (10 fs, 830 nm) is to be held clean at least to the 10^4 level, then all the optics of the laser system should accommodate a bandwidth of at least 250 nm. The middle graph also demonstrates well, that even spectral components which carry relatively small fraction of the energy can contribute to the temporal shape significantly. For example for sech^2 pulses at $S_c=10^{-1}$ cut level although the energy content is still 95% the best achievable contrast drops to $3 \cdot 10^{-3}$. We can also see, that the energy loss due to spectral clipping is also becoming significant at levels, where the cut bandwidth is less than 3 times of the original one. As a consequence for a Ti:Sapphire laser system with sech^2 pulses of 20 fs FWHM at 830 nm central frequency to maintain a contrast of 10^4 the bandwidth acceptance of the stretcher and compressor system has to be 217 nm.

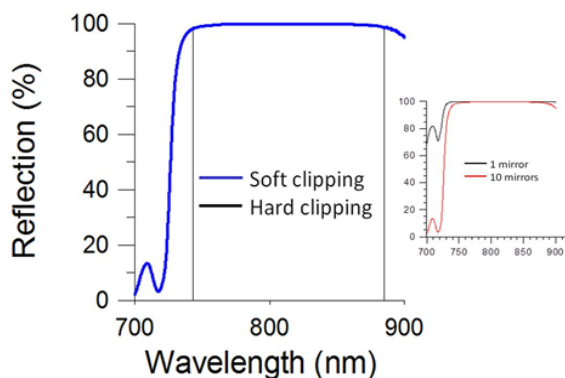


Fig.III.5.3. Definition of soft spectral clipping taking the typical spectral reflectivity of a dielectric mirror

However, most of the optical elements will exhibit a “soft” spectral cut, with a finite rise and fall spectral reflectance. For example, dielectric laser mirrors or gratings illuminated by laser beam of finite size exhibit such clipping. In terms of the contrast this is favourable compared to the hard clip as these “soft” apertures in the spectrum affect the contrast ratio less than the “hard” aperture case (similar to the near field characteristics of a beam when passing a hard or soft spatial filter). Using the typical spectral reflectivity of a dielectric mirror for our model (See Fig. III.5.3.), I have also calculated temporal contrast as the function of ratio between the bandwidth of the pulse and the spectral rise of the dielectric mirror. Spectral rise is defined as the half width of the half Gaussian fitted to the spectral profile. This model as approximation was used by us for the first time.

As expected the increasing sharpness of the cut makes the contrast worse, as shown on Fig. III.5.4. It can also be seen, that in the case of soft spectral clipping the Gaussian pulses show better contrast than sech^2 pulses. Furthermore compared to the hard spectral clip case the theoretical contrast, without ASE and phase errors, is better by a few orders of magnitude depending on the relative spectral rise and fall of the spectral clipping.

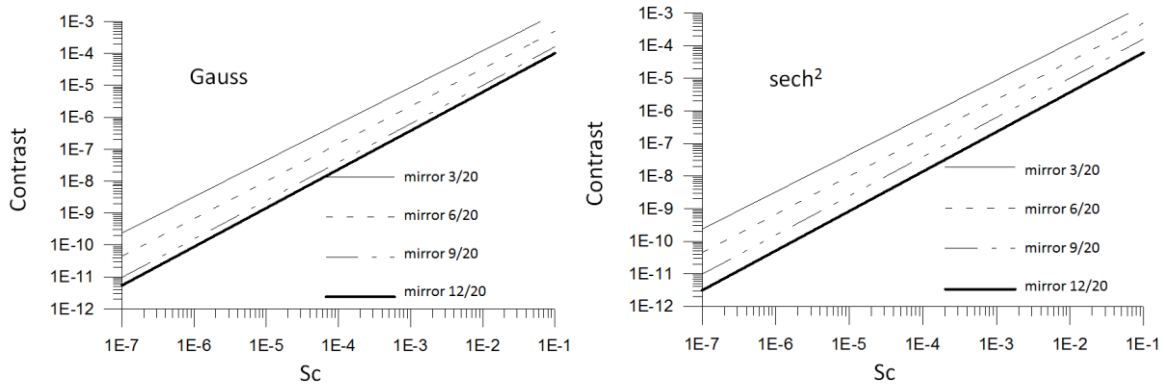


Fig.III.5.4. Contrast as a function of spectral clipping at different spectral 'softness' for both pulse shapes. Softness is defined by the ratio of the halfwidth of the pulse's spectrum vs the cut spectrum

III.5.1.2 Third order dispersion

Apart from the spectral clipping during beam propagation through the CPA system phase errors introduced by non-matched stretcher and compressor and misalignment of these elements can cause higher order phase distortion. As even spectral phase contribution will cause symmetrical distortion of the pulseshape in the pre-and postpulses I have studied in more detail the effect of 3rd order (TOD) phase. Our aim was to see at what level the effect of third order distortion becomes significant.

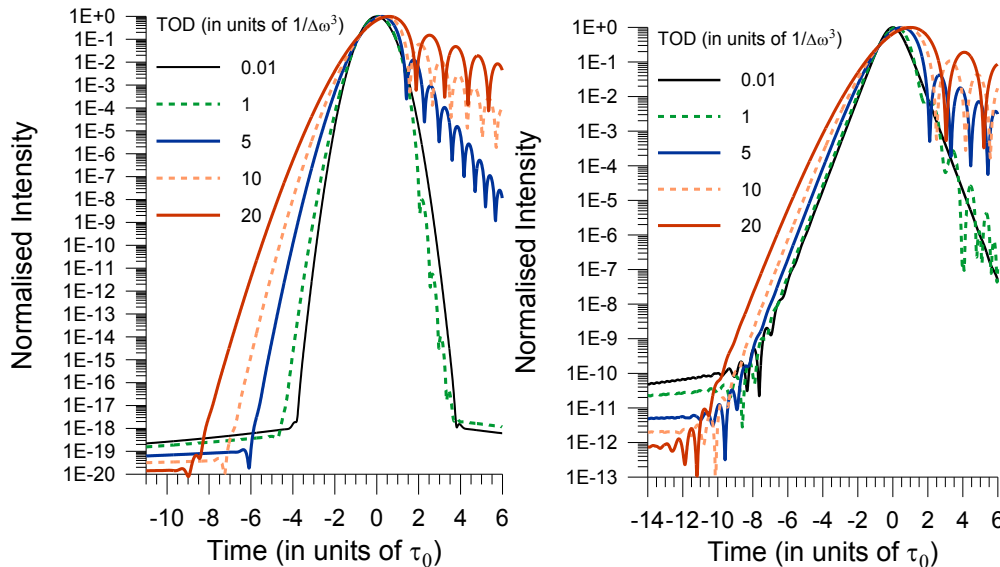


Fig.III.5.5. Temporal distribution of the pulses at different levels of TOD for Gaussian (left) and sech^2 pulses (right)

The temporal distribution of the pulses in the presence of TOD is shown in Fig. III.5.5. The contrast, relative pulse length (compared to the transform limited case) and peak intensity are plotted

as a function of TOD (Fig.III.5.6.). TOD is displayed normalized to the 3rd power of the original bandwidth, so applicability to different wavelengths and pulse durations is easier. The effect of TOD was calculated within a broad enough spectral range to avoid the clipping effect.

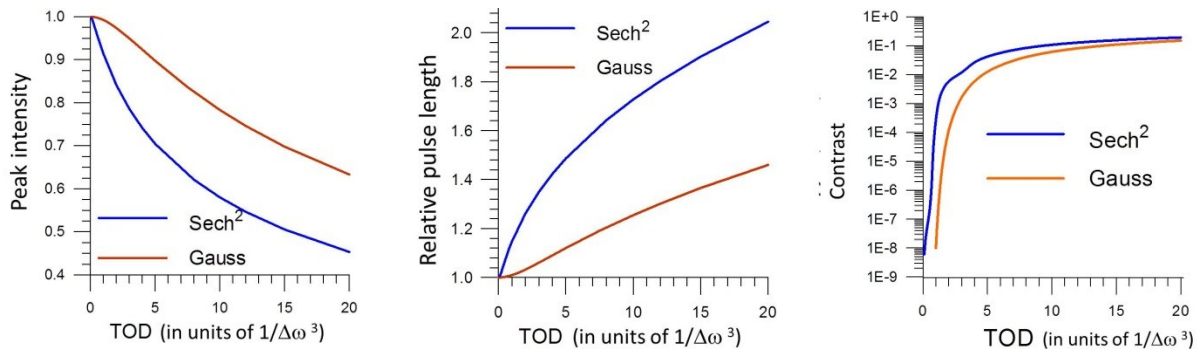


Fig.III.5.6. Pulse characteristics as a function of the TOD level

It can be seen, that peak intensity drops much faster in the case of sech² pulses, as in this case the pulse lengthening is more dramatic in the presence of TOD. For example in the case of the before mentioned laser pulse, at 830nm central wavelength and 10fs BWL pulse length, the TOD has to be less than 110 fs³ in order to keep contrast at least at 10⁻⁴ level. We can also see that TOD has a much larger effect on the temporal contrast than on other parameters of the laser pulse. For instance in the case of TOD=2 1/Δω³ the duration of the Gaussian pulse changes by 4% and the peak intensity drops by 3%, which does not seem significant. However the best achievable contrast in this case is only 10⁻⁴.

Fig.III.5.7. shows the effect of large negative TOD (-100 1/Δω³) at different levels of asymmetrical spectral cut. It can be seen, that although contrast is poorer as expected, the secondary peaks appear in the post-pulse region and hence when clean rising edge is required for the experiment negative TOD would be preferable to the positive. This can be considered when the clip is due to limited grating size and contrast in the post-pulse regime can be sacrificed to improve pre-pulse performance.

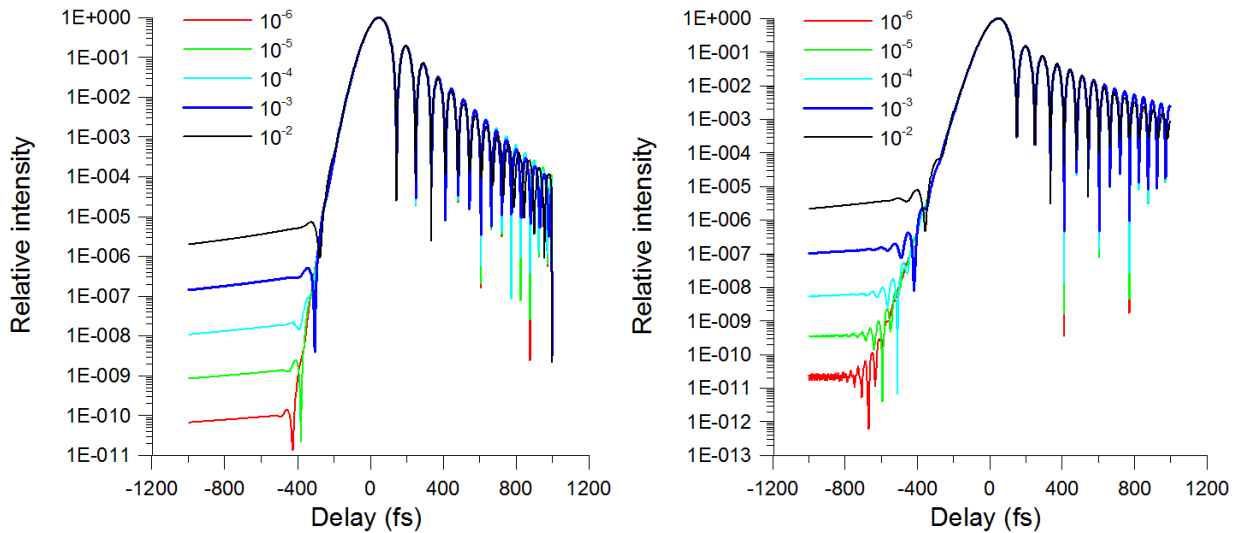


Fig.III.5.7. Contrast as a function of hard spectral clipping with presence of TOD at different levels of the spectrum

III.5.2 Measurements

III.5.2.1 Detection of contrast with correlators and spectrometers

We have already seen that temporal contrast can be estimated at 2 orders of magnitude higher intensity levels, than where the spectrum is measured. With high dynamic range spectral measurement spectral features even at the low intensity spectral components can be observed and utilized to optimize the system for better contrast. If “dips” in the spectrum can be compensated through amplification by pre-shaping the spectrum, then potentially higher contrast can be achieved, as it is shown in Fig.III.5.8.

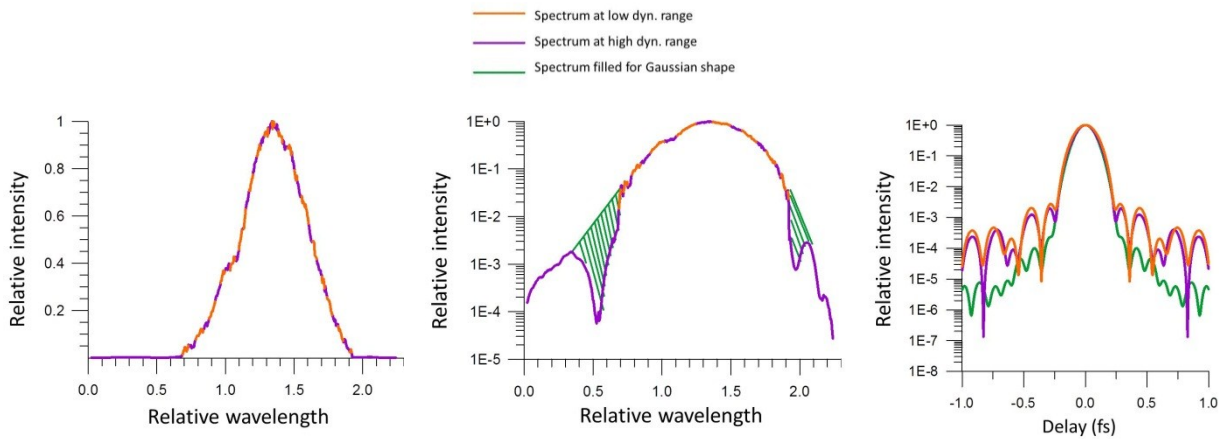


Fig.III.5.8. Effect of spectral “filling” at high dynamic range

Apart from spectrometer, usually most ultrashort pulse laboratories are equipped with autocorrelators, which are relatively easy to operate. However these devices are not able to estimate contrast or show asymmetrical features linked to TOD. Fig. III.5.9. shows 2nd order interferometric autocorrelation curves calculated at different levels of TOD.

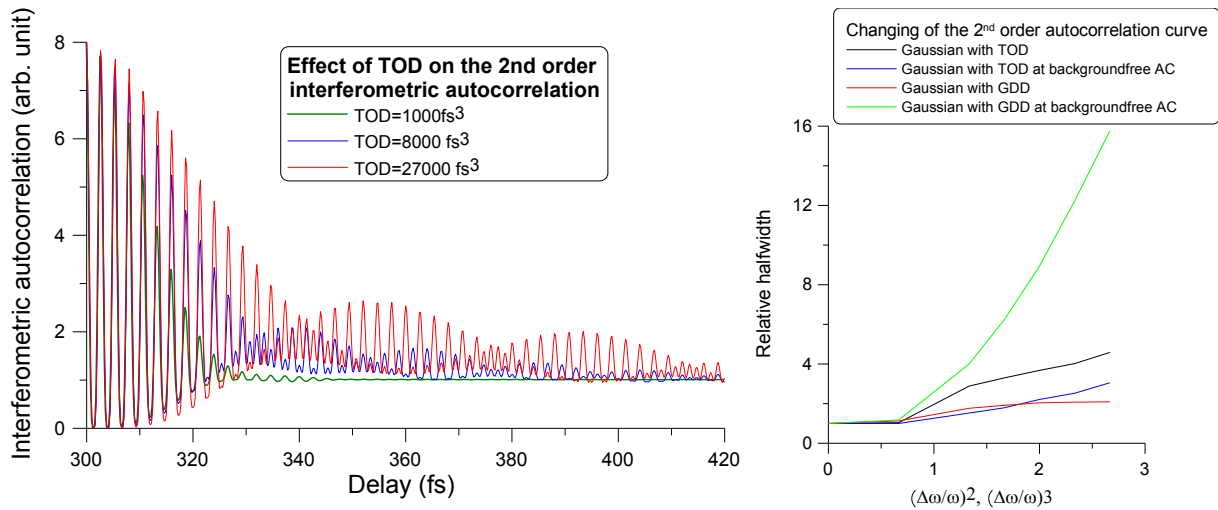


Fig.III.5.9. Interferometric autocorrelation curves and their relative half width at different levels of TOD

Using the relative half width of the pulse as an indicator is also not reliable, as it can be seen from Fig III.5.10. Even at four orders of magnitude of contrast change the autocorrelation curves will not show a significant feature suggesting contrast degradation, as our models have suggested before.

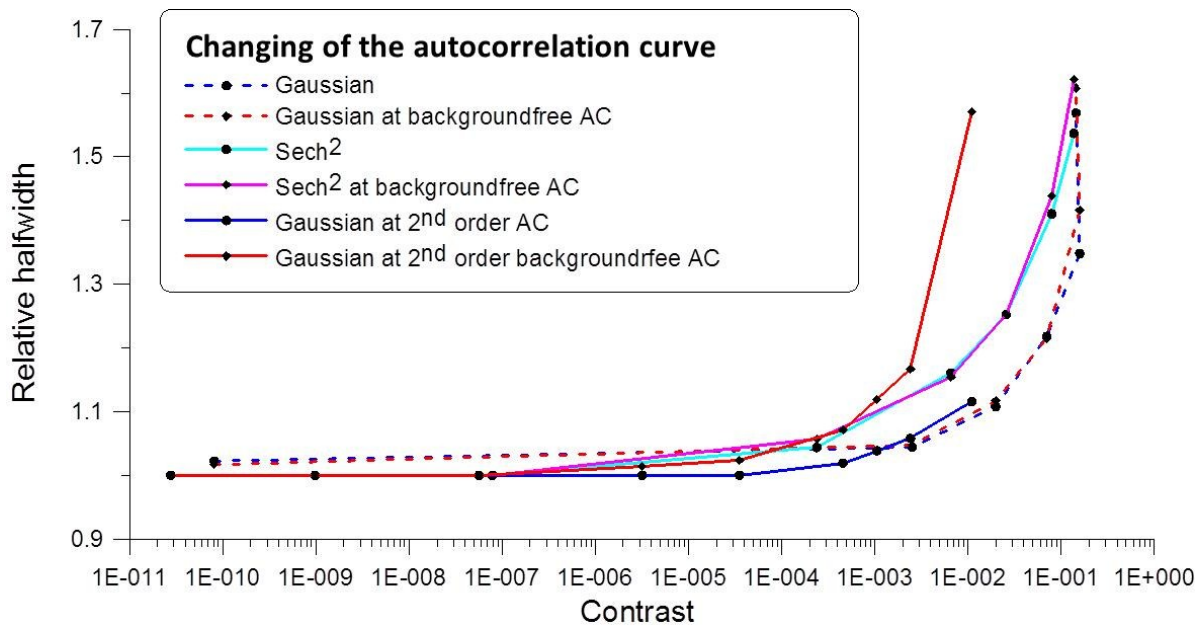


Fig.III.5.10. Relative half width at different contrast levels in the presence of TOD calculated for 2nd and 3rd order auto-correlators in background free and not background free case

III.5.2.2 Measurements on TITANIA Kr:F system*

Measurements were carried out on the TITANIA Kr:F laser system at Rutherford Appleton Laboratory to check the validity of the best achievable contrast estimation from the high dynamic range spectral characterization of the pulse. The temporal contrast and the spectral distribution were measured by a cross correlator and by a home-made spectrometer with a dynamic range of 10^7 and 10^2 , respectively. Fig.III.5.11. shows a typical and a distorted spectral intensity profile for the seed pulse of the laser system with the corresponding calculated temporal distribution. From here one can already see, that almost an order of magnitude contrast change corresponds to relatively small changes in the spectrum and the pulse duration.

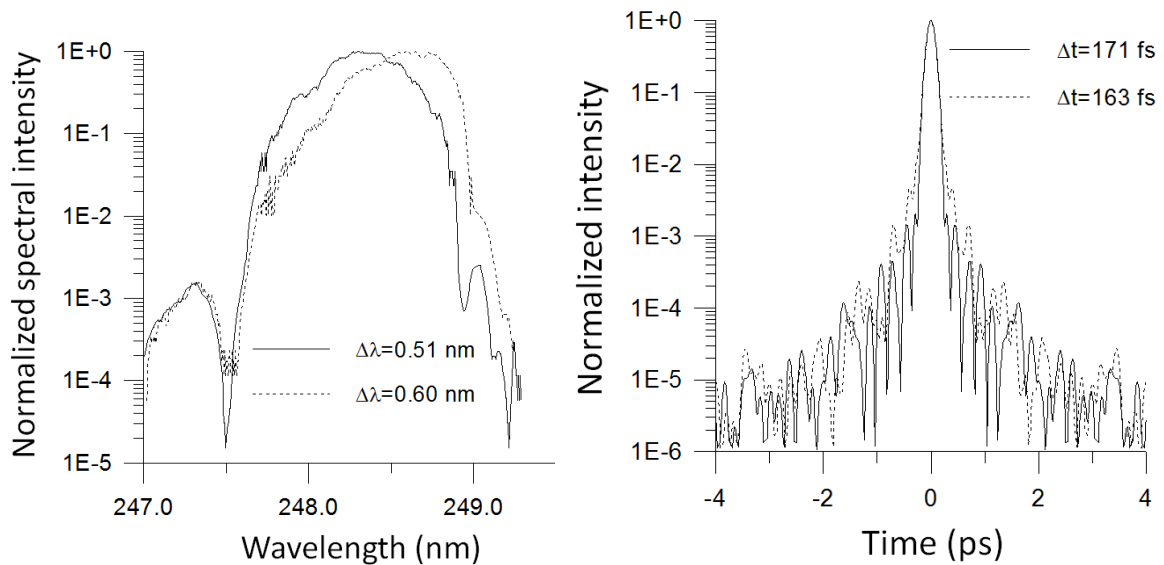


FIG.III.5.11. The seed pulse of the TITANIA laser system plotted on the left in a case of normal operational spectrum (solid line) and in a distorted case (dashed line). The calculated temporal distribution is shown on the right.

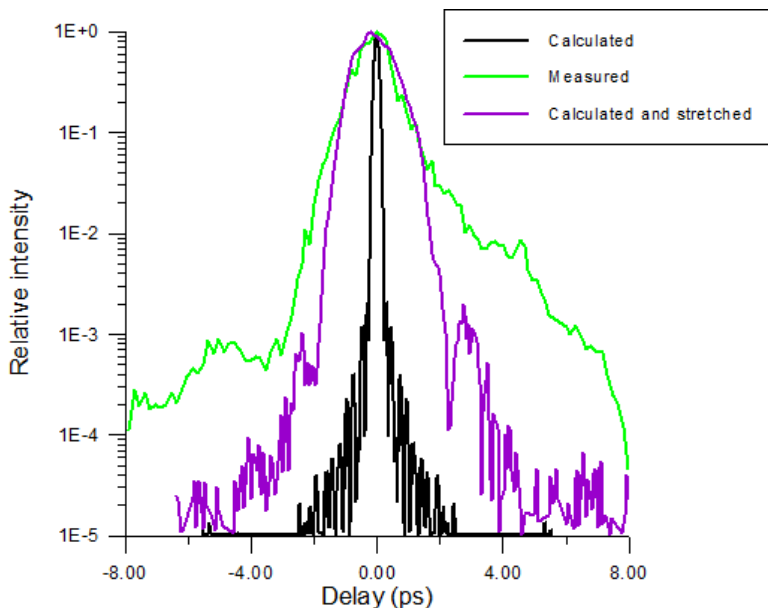


Fig.III.5.12. Pulses of the KrF TITANIA laser system retrieved from the spectrum

For better temporal resolution the sech^2 seed pulse of the system was stretched by a factor of 8 and measured by cross-correlation (Fig.III.5.12). The retrieved pulse duration from the spectrum (black curve) was also stretched by applying the same amount of GDD as expected from the stretcher (purple) and is compared to the measured temporal distribution of the stretched pulse (green).

The agreement between the measured contrast and the retrieved pulse shape is excellent above the level of 6×10^{-4} . A better fit down to the theoretically predicted level of 1.4×10^{-4} determined from the calculation for a transform limited pulse with no chirp could be achieved by also taking into account the higher order dispersions.

III.5.3 Conclusion

I have shown a quick, reliable and universal method for estimation of the temporal contrast of high power pulses, which is especially useful in everyday laboratory practice. The calculation predicts, as was also proved in an experiment, that the best achievable temporal contrast of an ultrashort pulse can be estimated from the spectrum at a significantly lower dynamic range^{III.18,III.19}. Tolerances for the spectral transmission of the optics as well as for the non-compensated residual third order dispersion of a laser system have been established in order to obtain ultrashort pulses with high temporal contrast. As a result of the calculation I have also found, that Gaussian pulses are less sensitive to spectral clipping than sech^2 pulses. It also has been shown, that more realistic soft spectral clipping allows for higher contrast, than hard cutting of the spectrum. Through calculations I have proved, that conventional autocorrelators are not capable to estimate the contrast.

Measurements on the Titania Kr:F laser system have been carried out to confirm modelling results. Temporal shape retrieved from the spectrum and the theoretical phase show good agreement. We have also shown that by pre-shaping the spectrum prior to amplification significant improvement of the contrast can be achieved.^{III.20,III.21}

IV. SUMMARY

1. I have built a multi-pass diode-pumped MOPA for CERN CTF2, offering a combination of high gain and efficiency with high stability. A simple rod-cavity design and the establishment of quasi-steady-state operation resulted in a high gain saturated operation with mean output intensity during the pulse train of $7\text{kW}/\text{cm}^2$ in the case of the Photo Injector Long Train (PILOT) laser for CTF2. I have developed a code to verify the operation of the amplifier and to provide a useful tool for further designs^{III.3,III.4}. Zernike analysis of the measurements of pump distortion exhibited an almost pure astigmatic phase error from the thermal load, which can be compensated, up to high average power levels. PILOT system has allowed the first long train injector operation at CERN.
2. I have designed a two stage MOPA system for CTF3 with $25\text{kW}/\text{cm}^2$ output mean intensity in the IR. Photo-injector laser^{III.5,III.6,III.7,III.8,III.9} (PHIN) amplifiers exhibit an output stability of 0.2% rms and 0.34% rms, respectively, and proved the capability to compensate for the slow drifts of the input intensities. Response to fast variations of the input seed amplitude was investigated for the steady-state regime and time- and frequency domain measurements were carried out to study noise propagation through the system. The output pulse stability already competes favourably with that of the best already available lasers with active stabilization. This can be further improved using a more stable diode-laser power supply and improved coolant and room temperature stability, which was varying $5\text{-}6^\circ\text{C}$ over the day. Additional stabilisation is also achievable using a closed cycle feedback control system. Specified energy levels were delivered to the cathode. The CTF3 photo-injector driven by the PHIN laser is still unique of its kind with its high average current capability. The laser was also used to deliver photo-electrons for the Concept d'Accélérateur Linéaire pour Faisceau d'Electron Sonde (CALIFEs) probe beam injector, where the first two-beam acceleration experiments took place as a proof of principle for CLIC scheme.
3. I have determined the two photon absorption coefficient of 5 mm - 15 mm long BBO, CLBO, KDP and LBO samples from the measurement of intensity dependent transmission at 248 nm ^{III.13,III.14}. The theoretical fit to the experimental results show a TPA value of 0.48 cm/GW, 0.5 cm/GW, 0.34 cm/GW, 0.22 cm/GW and 0.53 cm/GW for KDP, BBO (o-ray), BBO (e-ray), LTB and CLBO, respectively. To our best knowledge, this was the first measurement of the TPA coefficient of LTB and CLBO crystals, providing a good reference when choosing conversion or parametric amplifier crystals for high intensity applications in the UV regime^{III.15,III.16}.
4. I have designed and implemented a phase-coding system for the PHIN laser, which provides the required pulse structure for electron beam combination in CTF3 and for future CLIC application too^{III.9-III.10}. The system was based on fast Mach-Zehnder fiber modulators used in telecommunication. An accurate timing and amplitude balancing system was invented using frequency domain measurements. The delay can be set with 0.1ps accuracy and introduces no

additional jitter to the laser oscillator. The amplitude balance between sub-trains has been set to be within the required error level of 0.1% rms. Further improvement is currently limited by fast noise of the laser oscillator. The performance of the system was verified also on the electron beam. Indeed, it showed a laser based switch free from satellites while all the important electron beam parameters have been preserved as charge, charge stability, energy spread, and emittance.

5. I have developed a quick, reliable and universal method for estimation of the temporal contrast of high power pulses, which is especially useful in everyday laboratory practice. The calculation predicts, as was also proved in an experiment, that the best achievable temporal contrast of an ultrashort pulse can be estimated from the spectrum at a significantly lower dynamic range^{III.18}. Tolerances for the spectral transmission of the optics as well as for the non-compensated residual third order dispersion of a laser system have been established in order to obtain ultrashort pulses with high temporal contrast. As a result of the calculation I have also found, that Gaussian pulses are less sensitive to spectral clipping than sech^2 pulses and that more realistic soft spectral clipping allow for higher contrast, than hard cutting of the spectrum. I have also shown that conventional auto-correlators are not capable to estimate the contrast. I have shown, that double pulses within less than $\times 10$ of the laser pulse length will also be present in the spectrum through modulation. To confirm the modelling results, measurements have been carried out on the Titania Kr:F laser system. There is a good agreement between the measured temporal shape and that one retrieved from the spectrum^{III.18-III.19}.

Magyar nyelvű összefoglaló

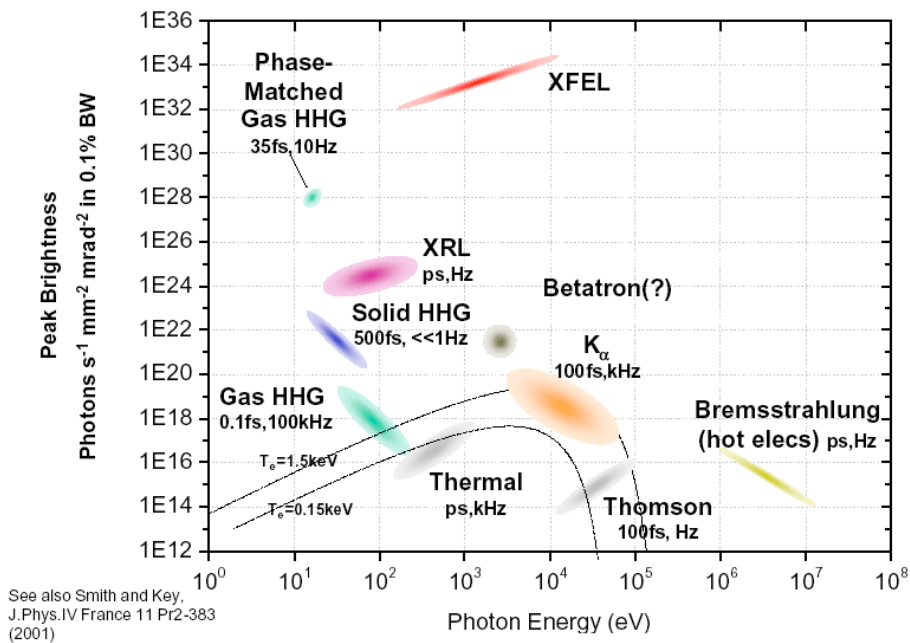
1. Bevezetés

Napjainkban a nagyenergiájú nukleáris kísérletek a teraelektronvoltos (TeV) tartományban keresik a választ a fizika alapkérdéseire és a standard modellt megalapozó, illetve az azon túlmutató elméletekre utaló bizonyítékok után kutatnak. A Nagy Hadronütköztető gyűrűben (LHC, Large Hadron Collider) a protonok fognak végleges 7 TeV-os energiára gyorsulni, így ez lesz a legnagyobb energiájú ütköztető a világon. Ezzel párhuzamosan lepton gyorsítók fejlesztése is zajlik annak érdekében, hogy a felfedezett részecskéket a megfelelő energiatarományban nagy pontossággal tudják vizsgálni. Mivel a gyűrű alakú gyorsítóknak elérhető energia kis tömegű részecskék esetén a szinkrotron sugárzás útján elvesztett energia miatt korlátozott, nagyobb energiájú elektronokat csak lineáris gyorsítókkal lehet előállítani. Az egyik nagyszabású kutatás-fejlesztési program ebben az irányban az 1980-ban elindított Kompakt Lineáris Gyorsító projekt (CLIC, Compact Linear Collider). Ennek a célja egy nagy fényességű elektron-positron ütköztető kifejlesztése néhány TeV tömegközépponti energiával. A CLIC-ben a gyorsítás két nyalábon alapul. Egyrészt, egy nagyáramú 12 GHz-es meghajtó nyalábot állítanak elő alacsonyabb frekvenciájú nyalábkötegek egyesítésével. A teljesítményt a nyaláb lassításával nyerik ki, és nagy térerősségű gyorsító struktúrákban egy második, ún. próbanyaláb felgyorsítására használják. A harmadik CLIC teszt konstrukció (CTF3, CLIC Test Facility 3) ezt a gyorsítási tervet bizonyítja és optimalizálja.

Ezzel párhuzamosan világszerte megindult az ún. szabadelektron lézerek (FEL, Free Electron Lasers) fejlesztése is azzal a céllal, hogy extrém ultraibolya tartományban nagy fényességű foton nyalábokat állítsanak elő, mellyel kondenzált anyagok kutatására, illetve az ultragyors reakciók és folyamatok vizsgálatára nyílik lehetőség. A szabadelektron lézerek ugyancsak lineáris elektron gyorsítón alapulnak, amit egy fotonok előállítására szolgáló undulátor követ. Ezek a típusú lézerek az elmúlt évtizedben egyre rövidebb hullámhosszú és egyre koherensebb sugárzást tudnak előállítani, és jelenleg egyedülálló fényességet nyújtanak az 1 keV-os foton energia tartományban. Ehhez azonban rövid, minőségi elektronkötegek előállítása szükséges. Ezeket az elektronokat fotoinjektorokkal állítják elő. A fotoinjektor vagy más néven foto-elektron ágyú fotoemisszió útján egy lézer által besugárzott fotokatódából állítja elő az elektronokat. Ezek az elektronok az ágyúban lévő elektromos tér hatására néhány MeV energiára gyorsulnak fel kilépésük után. Foto-elektron ágyúk segítségével két nagyságrenddel nagyobb fényességű elektronnyalábot lehet előállítani, mint a hagyományos, termikus (izzókátódos) elektron injektorokkal. Emiatt mind a CLIC meghajtó, mind a próbanyaláb esetében mérlegelik ennek a típusú elektronforrásnak a használatát. Azon kívül, hogy minőségi nyalábok állíthatók elő ezen az úton, a foto-elektron ágyún alapuló injektorok kihasználják a lézerek által nyújtott előnyöket is. A lézer impulzusok idő- és térbeli alakja változtatható; a lézereszcillátorok által előállított impulzusok ismétlési frekvenciája a gyorsítóhoz hangolható; az impulzusok erősíthetők; és optikai kapuk segítségével az impulzussorozat struktúrája is változtatható. Manapság ennek köszönhetően a lézerek fontos részét képezik egy szabad elektron-lézer rendszernek nemcsak az elektronok

előállításával, hanem azzal is, hogy az ún. pumpa-próba kísérletekhez szinkronizált lézer impulzusokat szolgáltatnak.

Nagy intenzitású ultraibolya impulzusok más úton is előállíthatók. Az egyik, hagyományos lézereken (nem FEL-konstrukción) alapuló technika a többszínű lézer, ahol a rövid impulzusokat az infravörös tartományban állítják elő és erősítik, majd nemlineáris folyamatok útján konvertálják rövidebb hullámhosszakra. A fázismodulált erősítési technika (CPA, Chirped Pulse Amplification) kifejlesztése és a módus szinkronizálási technikák fejlődése jelentős előrehaladást hozott a rövid impulzusok szilárd anyagokban történő nagy hatásfokú erősítésében. A CPA kihasználja, hogy a szélessávú, rövid impulzusokat diszperzió útján meg lehet nyújtani, és ezáltal alacsony intenzitáson erősíteni. Ezzel elkerülhetőek a nemlineáris effektusok, az anyag roncsolása és az erősítés után az impulzus közel eredeti hosszúra nyomható össze. A pumpáló energia tárolásán alapuló erősítőknél túl az optikai parametrikus erősítők is kihasználják a CPA-technikát, és ultra szélessávban erősítik a megnyújtott impulzusokat. Ezeknek a komplex lézerrendszereknek minden eleme befolyásolhatja a nyaláb minőségét, csökkentheti a kimeneti energiát, annak stabilitását, vagy a sáv szélességet. Mindezek a végső fókuszált intenzitást és a lézer felhasználhatóságát korlátozzák.



1. Ábra: A jelenleg létező fotonforrások fényessége a fotonenergia függvényében. Innen látható, hogy az 1keV-os tartományban a szabad elektrón lézerek jelenleg egyedülálló fényességgel rendelkeznek, bár a magas harmonikus keltésével előállított mély ultraibolya sugárzás még tartogathat meglepetést.

1. A kutatás motivációja és célkitűzések

A második CLIC teszt konstrukcióban (CTF2) az elektronok előállítására szolgáló lézer rendszer 2001-ben villanólámpával pumpált regeneratív és több nyalábutas erősítőknél alapult. A különálló impulzusokat szétválasztva, késleltetve, majd „összerakva” állította elő a kívánt 48 impulzust. Ezzel a módszerrel hosszabb impulzussorozat előállítása nem volt célszerű. Mivel a végső CLIC nagy

átlagáramú elektronnyalábjának előállításához több ezer impulzusra van szükség 500MHz-en, további lézerfejlesztésre és technológiai változtatásokra volt szükség a nagy átlag- és impulzussorozat teljesítmények eléréséhez. **A kutatás során olyan dióda pumpált 'master' oszcillátor teljesítményerősítőt építtek többutas nyaláb elrendezésben, amely a Nd:YLF módus szinkronizált oszcillátor impulzusait ötezerszeresükre erősíti. A rendszer kimeneti paramétereit állandósult állapotban vizsgálom, majd hosszú, negyedik harmonikusra konvertált impulzussorozatokat állítok elő, ezzel megfelelő energiát szolgáltatva a CTF2 elektron ágyúhoz az ultraibolya tartományban. Dolgozok egy kód kifejlesztésén is, ami a „többutas erősítőt” modellezi, majd összehasonlítom a modellt a mérési eredményekkel.**

A fent említett PILOT (Photo-injector Long Train) lézer a stabilitás kivételével minden szempontból megfelelt a CTF2 elektronágyúhoz. Ezért megkezdődött egy PHIN (photo-injector) teszt konstrukció építése is, ami egy nagyobb teljesítményű lézer építését magába foglalva, nagy átlagáramú elektronágyú megépítését tűzte ki céljául. A lézer stabilitása az ultra-ibolya tartományban 0,25% négyzetes középértékre volt megszabva. **A PILOT lézer mintájára két lézer erősítőt tervezek többutas elrendezésben, és összehasonlítom a mért és számolt kimeneti erősítést. Megmértem a lézer stabilitását és analizálok a zaj forrásait. A lézer és az általa előállított elektronnyaláb paramétereit között korrelációs méréseket végzek.**

A CTF3 rendszer egyik legnagyobb kihívása a nagy teljesítményű meghajtó elektronnyaláb előállítása, ahol az ismétlési frekvenciát 1,5 GHz-ről 12 GHz-re kell megnövelni. Ez késleltető és összefésülő gyűrűkkel érhető el, ahol nagy frekvencián működő, ún. elektronkilöklőt használnak fel az elektronok terelésére. Ehhez az elektron nyalábokat úgy kell rendezni, hogy „fázisban” és „nem fázisban” érkezzenek meg a kilöklőhöz. Ez az úgynevezett „fázis-kódolás” a jelenleg használt izzókatódos elektronágyúval, alacsony harmonikusokon alapuló gyorsítóüregekkel és nagyfrekvenciás kapcsolókkal érhető el. A kapcsolat nyolc elektronkötegen keresztül történik és mellékimpulzusokat eredményez a nem kívánt fázisban. Ezek a mellékimpulzusok a teljes töltésnek kb. 7%-át tartalmazzák, és jelentős sugárveszélyt jelenthetnek a jövőben a CLIC gyorsító esetén, mivel a fő elektronnyalábtól eltérő nyalábutat követnek. **A munkám során tehát olyan fáziskódolási rendszert építünk a lézeren, ami két egymást követő impulzus között kapcsol 200 ps-nál kisebb fel- illetve lefutási idővel minden 140 ns-ban. Emellett pontos, 180 fokos fázistolást kell létrehozni az 1,5 GHz-es elektron nyaláb ismétlési frekvenciájához képest a két kapcsolt impulzussorozat között. Ezen túl a fáziskódolt impulzussorozatot erősítem és a negyedik harmonikussal keltett elektronok tulajdonságait vizsgálom a CTF3 PHIN elektronágyún.**

A nagyintenzitású ultraibolya impulzussorozatok magas hatásfokú előállításához az impulzusokat infravörös tartományban állítjuk elő és erősítjük, majd nemlineáris kristályokban – az elektronágyú esetén – negyedik harmonikusokat keltünk. Annak az esélye, hogy két foton egyszerre nyelődik el az anyagban négyzetesen nő az intenzitással. Ezt az effektust „egy-nyalábos kétfotonos abszorpciónak” hívják (single beam two photon absorption TPA). Az elmélet jól ismert, de a nemlineáris abszorpció

tényező nem mindig adott az előállított hullámhosszokon a leggyakrabban használt kristályokra, sőt, néha a rendelkezésre álló adatok sem konzisztensek. **A célom az, hogy megmérjem a nemlineáris abszorpció tényezőt BBO, CLBO, LTB and KDP kristályokban 250 nm-es hullámhossz környékén.**

A fényesség, mint már korábban is említettem, az impulzus egyik legfontosabb tulajdonsága, annak energiaeloszlásától és fókuszálhatóságától függ. Mikor rövid impulzusok intenzitását adjuk meg, gyakran tipikus impulzuseloszlással számolunk, például gaussi vagy sech^2 alakokkal. Valós rendszerekben az impulzus időbeli eloszlása eltérhet ettől. Elő- és utóimpulzusok alakulhatnak ki a nyújtás, az erősítés és az összenyomás során. Az időbeli kontraszt – ami az elő- és utóimpulzusok intenzitásaránya a fő impulzushoz képest – ezt az időbeli eloszlást jellemzi. Az időbeli kontraszt befolyásolja az impulzus és az anyagok közötti kölcsönhatást a különböző kísérletekben. **A célom, hogy a valós optikai elemek fázisra és spektrumra gyakorolt hatását vizsgáljam, és ezen keresztül az időbeli kontrasztra vonatkozó következtetéseket vonjak le. Ezen túl kiszámolom, hogy hagyományos mérőeszközökkel – mint például spektrográffal és autokorrelátorral – milyen pontossággal lehet megbecsülni a kontrasztot.**

2. Vizsgálati módszerek

Az elektronágyúhoz szolgáló lézerek fejlesztése során folytonos és módus-szinkronizált Nd:YLF lézereket használok 300 mW kimenő teljesítményig, illetve 1,5 GHz-es ismétlési frekvenciáig. Ezek szolgáltatják az erősítők bemenő jelét. A pumpálás homogenitásának és a kimenő nyalábok térbeli eloszlásának mérésére CCD kamerákat alkalmazok. Gyors fotodiódákkal és gyors mintavételezésű oszcilloszkópokkal mérem az erősítést és az állandósult állapot kialakulását. Ugyanezekkel az eszközökkel mérem az elektro-optikai kapuk kapcsolását is. Az impulzus hosszát és az erősítés által okozott effektusokat (pl. telítődés, erősítés által okozott sávszűkülés stb.) Femtochrome háttérmentes letapogatásos (scanning) autokorrelátorral vizsgálom.

A kimeneti paraméterek és a konverziós hatásfok méréséhez különböző teljesítmény és energiamérő eszközöket (Gentec, Laser Probe, Coherent) használok. A termikus hatásokat sugárirányban nyíró Sagnac interferométerrel mérem, amit az erősítő kimeneti nyalábjába helyezek. A mért interferogramokat CCD képtároló és vonal analízáló rendszerrel dolgozom fel (Fringe Analyser Oxford Frame Store Applications Ltd.). Az erősítést és az állandósult állapot kialakulását számoló kódot MathCad-ben implementálok.

A kétfotonos abszorpció mérését a Szegedi Tudományegyetem TTIK Kísérleti Fizika Tanszékén kifejlesztett KrF lézerrendszerén végzem. A házilag készített elektronikával ellátott fotodiódákat LaserProbe energiamérővel kalibrálok be és oszcilloszkóppal digitalizálom a jelüket. Az adatokat Labview-ban írt kóddal olvasom ki, tárolom, majd analízálom. A pontos utóanalízist MathCad-ben írott kóddal végzem. A nyalábok térbeli eloszlását CCD kamerával mérem.

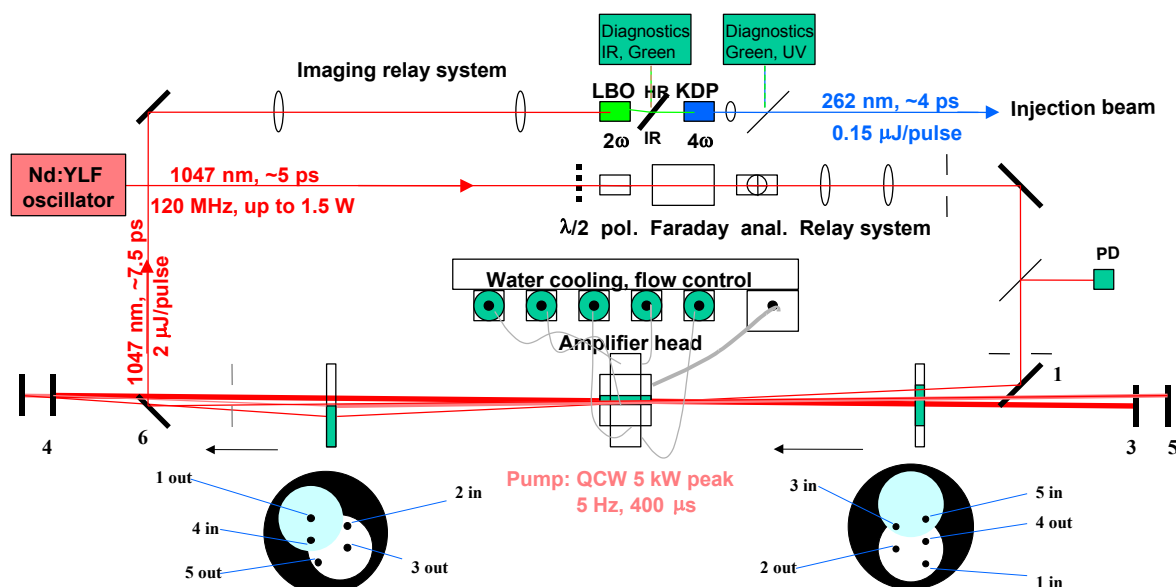
A fáziskódolás kifejlesztése során Hamamatsu „streak” kamerát használtak a kapcsolás pontosságának mérésére; illetve párhuzamosan, optikai szálás fotodiódákkal méretek egy 18 GHz-es LeCroy digitális oszcilloszkópon is.

Az elektronnyalábok által előállított Cserenkov-sugárzás időben bontott méréséhez ugyancsak Hamamatsu „streak” kamerával, ZEMAX-ban optikai vonalat terveztek. Az elektronnyaláb mérésére az optikai átmeneti sugárzást használva kapuzott, erősített jelű kamerákat használtak. Az előállított teljes töltés mérésére gyors áram transzformátort használtak.

Az időbeli kontraszt számolására egy általam írott MatLab kód szolgál. Az impulzushossz és a spektrum eloszlásának számításához bemeneti adatként mért adatokat és tipikus optikai elrendezéseket használtak.

3. Új tudományos eredmények

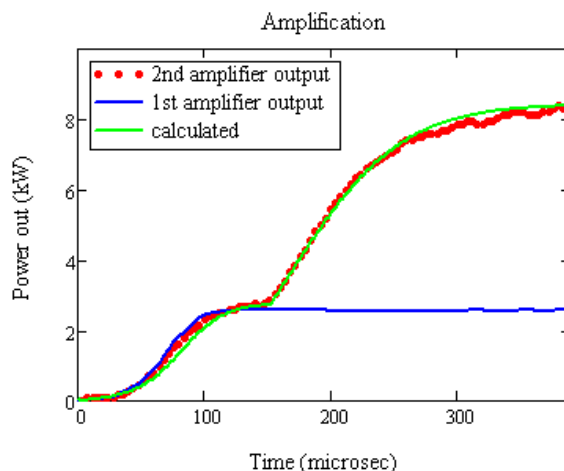
1. Megépítettem egy több utas dióda pumpált „master” oszcillátor teljesítmény erősítőt a CERN (Centre Européen pour la Recherche Nucléaire, ill. European Organization for Nuclear Research) CTF2 fotoinjektorához, melynek során egyszerű oldalpumpált rúd geometriával dolgoztam.



2. Ábra: A PILOT lézer rendszer vázrajza

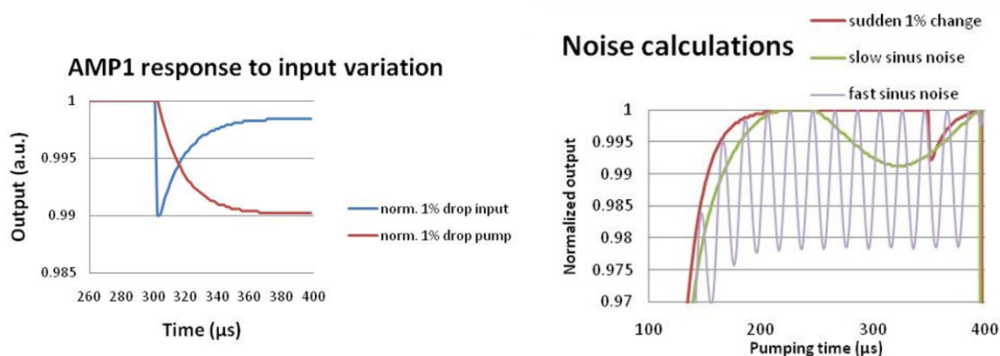
A megépített PILOT rendszer nagy erősítéssel, hatásfokkal és stabilitással bír. Az állandósult állapotban (steady-state) fennálló telített erősítéssel 7 kW/cm^2 kimeneti impulzussorozat átlagteljesítményt értem el. A MathCad-ben kifejlesztett kód jó egyezést mutat a mért eredményekkel, és alkalmazható a rendszer felskálázására. A pumpálási eloszlás Zernike analízise azt mutatta, hogy a nyalábban csak asztigmatikus torzulás van a termális hatások miatt, ami könnyen kompenzálható nagyobb átlagteljesítmények esetén. A PILOT lézer rendszer lehetővé tette az első hosszú impulzussorozatú működést a CERN elektronágyn, ezzel nagyáramú elektronnyalábot előállítva.

2. Megterveztem egy két erősítőből álló rendszert, ami a PILOT lézerhez hasonlóan egy dióda pumpált „master” oszcillátor teljesítmény erősítő, 25 kW/cm² kimenő impulzussorozat átlag



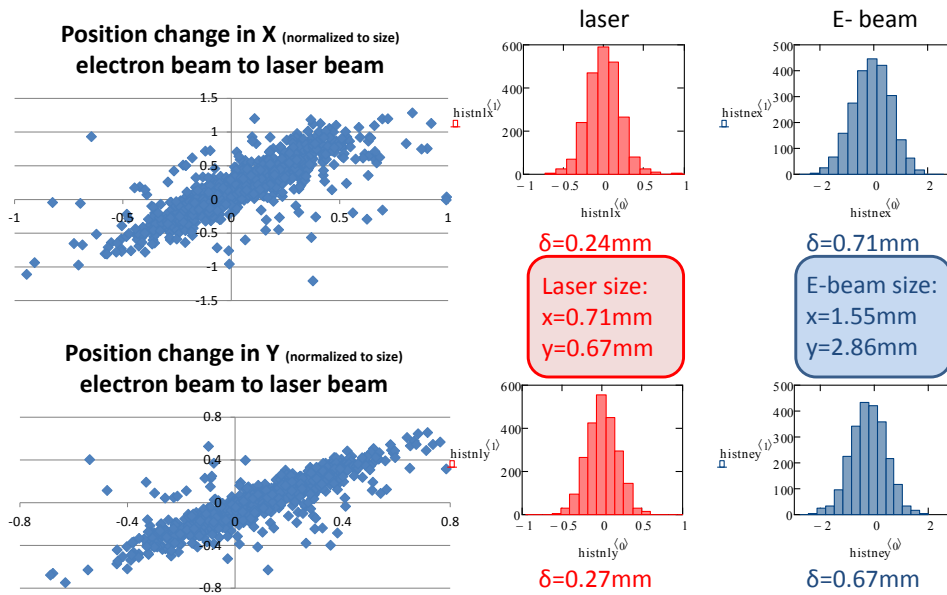
3. Ábra : Állandósult állapotú erősítés mért és számolt időbeli felépülése a CFT3 PHIN lézerrendszeren

teljesítménnyel. A fotoinjektor lézer (PHIN) erősítők 0,2% és 0,34% négyzetes középátlag stabilitást mutatnak és a bemenő jel lassú változását nagymértékben kompenzálják. A bemenő jel gyors változásait a kimeneten vizsgáltam az állandósult állapotban időbontott és frekvencia tartományban végzett mérésekkel, majd ezeket a modellel összehasonlítottam.



4. Ábra : A kimenő jel változása különböző bemeneti változások esetén a két erősítő után

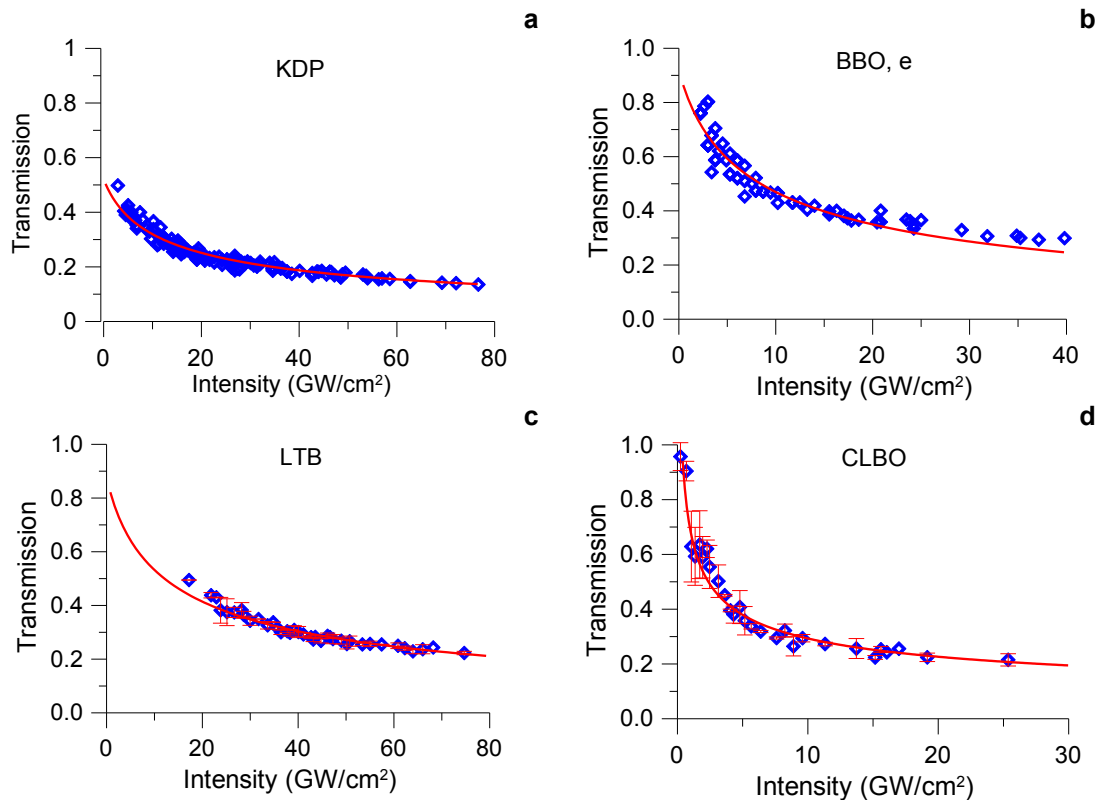
A kimenő jel stabilitása a hasonló fotoinjektor lézerekhez képest – aktív stabilizálás alkalmazása nélkül – kiemelkedő. Ez tovább javítható a pumpáló diódák tápegységének stabilizálásával, az erősítő vízhűtőjének pontosabb szabályozásával, valamint a lézerszoba hőmérsékletének kontrolljával (a hőmérséklet 5-6 °C változott a nap során). Zárt körű visszacsatoló rendszerrel további stabilizálás lehetséges. A kívánt energiaszintet a katódnál elérte a rendszer, és a CTF3 fotoinjektor ezzel a lézerrel meghajtva mai napig egyedülálló átlagáramot állít elő.



5. Ábra : A lézer és az elektronnyaláb között végzett korrelációs mérés a nyalábmozgás vizsgálatára

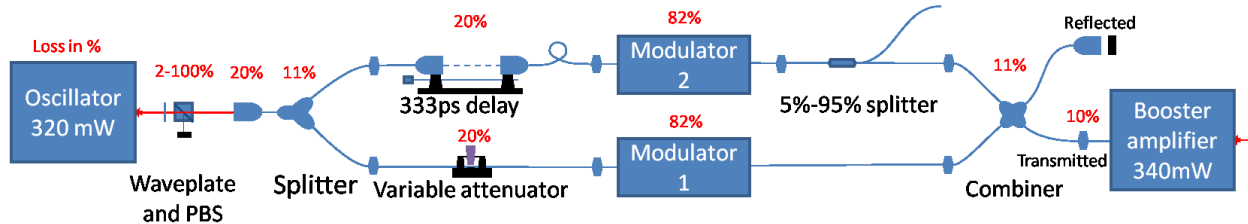
A lézerrendszert a CALIFEs (Concept d'Accélérateur Linéaire pour Faisceau d'Electron Sonde) próba nyaláb injektorhoz is használtuk elektronok előállítására, ahol az első két nyalábos elektron gyorsítást bizonyítottuk a CLIC rendszerben.

3. Meghatároztam a kétfotonos abszorpciós tényezőt 5 mm és 15 mm közti hosszúságú BBO, CLBO, KDP and LBO kristályokban 248 nm-en intenzitásfüggő transzmisszió mérése útján. Az elméleti illesztés a mért adatokhoz a következő nemlineáris abszorpciós tényezőket eredményezte: 0,48 cm/GW, 0,5 cm/GW, 0,34 cm/GW, 0,22 cm/GW és 0,53 cm/GW ebben a sorrendben a KDP, BBO (o-sugár), BBO (e-sugár), LTB és CLBO kristályokra. A legjobb ismeretünk szerint ez volt az első mérés LTB-re és CLBO-ra, hasznos referenciát nyújtva arra az esetre, amikor nemlineáris kristályt választunk nagyintenzitású ultraibolya impulzusok előállítására parametrikus erősítés vagy harmonikus keltés útján.



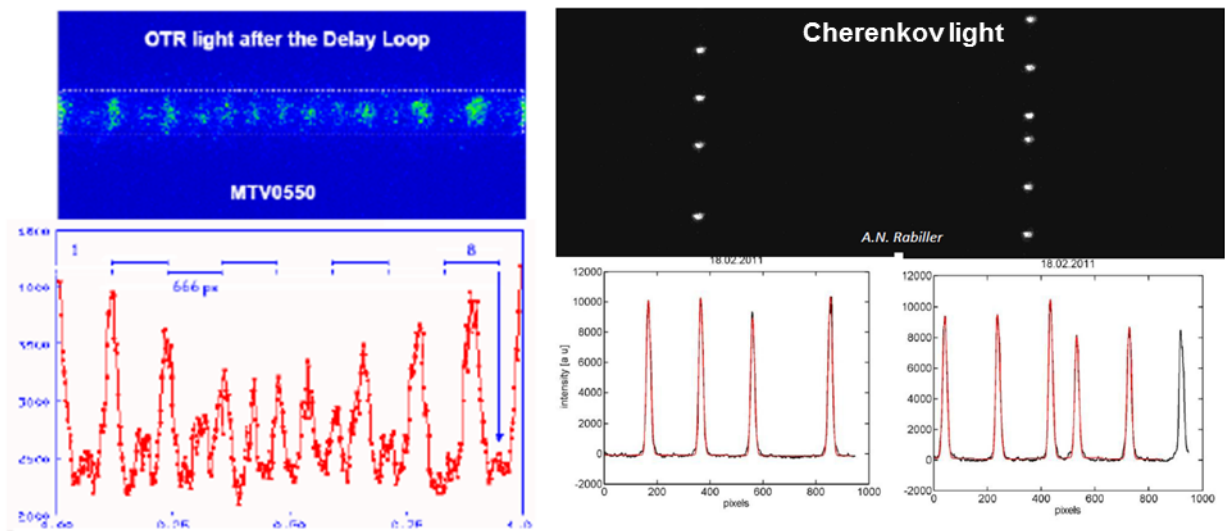
6. Ábra : Nemlineáris abszorpciós mérések KDP (a), BBO (b), LTB (c) és CLBO (d) kristályokra.

4. Megterveztem és megépítettem egy fáziskódoló rendszert a PHIN lézeren. A kódoló megfelelő impulzusstruktúrát állít elő, és alkalmazható mind a CTF3, mind pedig a CLIC elektron nyalábköteg kombinációjához. A rendszer gyors kapcsolási idejű Mach-Zehnder száloptikás modulátorokon alapul, amelyek használata a telekommunikációban már elterjedt.



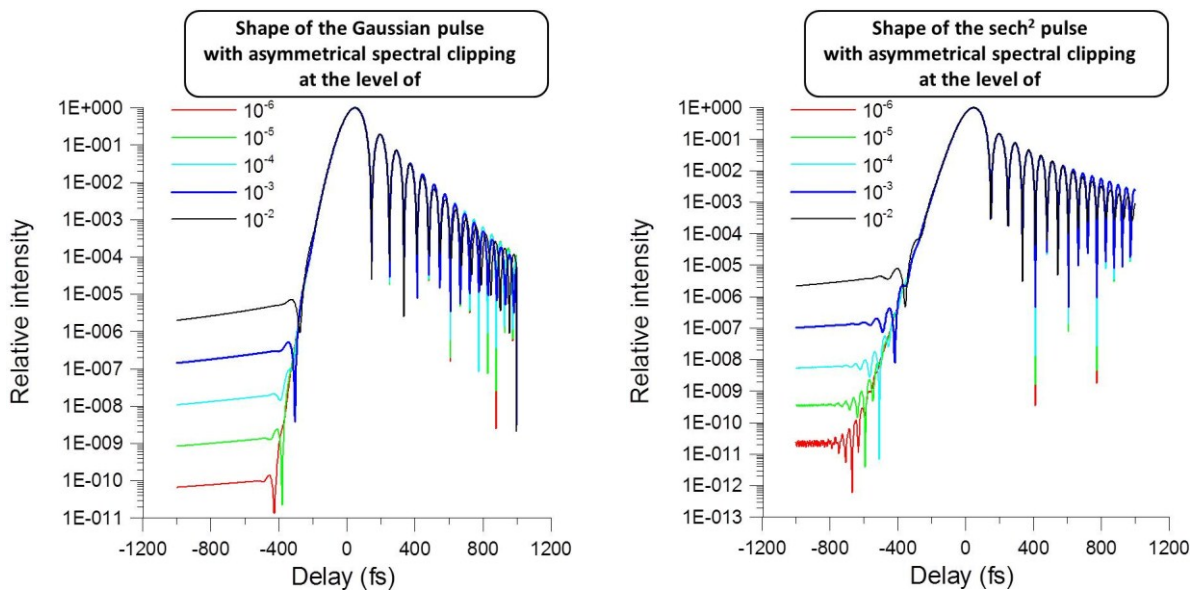
7. Ábra: A fáziskódoló rendszer vázrajza a mért veszteségekkel.

A pontos időbeli és amplitúdó beállítást frekvenciatartományban végzett mérésekkel értem el. A késleltetést 0,1 ps pontossággal, míg az amplitúdót 0,1% pontossággal állítottam be. Ennél jobb eredményt az oszcillátorból eredő gyors amplitúdó változások miatt nem lehetett elérni. A rendszer működését az elektronnyalábon végzett mérésekkel is ellenőriztem. A lézeren alapuló fáziskódolás nem okoz mellékimpulzusokat és az elektronnyaláb legfontosabb paramétereit – töltés, töltésszabályozás, az energia spektrum kiterjedése és az „emittance” – megőrzi.



8. Ábra: A fáziskódolt elektron nyalábkötegek a kapcsolási fázisban. Bal: Izzókátodos elektronágyúval és szubharmonikus kapcsolással elért kódolás. Jobb: Lézerrel meghajtott elektronágyú nyalábkötegei a lézeres kódolással.

5. Gyors és hasznos módszert dolgoztam ki nagy intenzitású impulzusok időbeli kontrasztjának becslésére. A számolások alapján azt találtam, hogy a maximálisan elérhető legjobb kontraszt megbecsülhető a spektrumból, sokkal alacsonyabb dinamikus tartományban történő mérések alapján is.



9. Ábra : A spektrális vágás hatása a kontraszton. A spektrum különböző dinamikus tartományokon van vágva.

Nagy időbeli kontrasztú impulzusokat előállító rendszerek toleranciáját is vizsgáltam a benne foglalt optikák spektrális átmeneti függvényére és a magasabb rendű diszperzió hatására vonatkozóan. Az ezekre a paraméterekre vonatkozó számítások kimutatták, hogy a gaussi impulzusok kevésbé érzékenyek a spektrális vágásra, mint a sech^2 impulzusok. Továbbá azt találtam, hogy a

spektrum éles vágásával ellentétben a valóságban gyakrabban előforduló lágy vágás kevésbé rontja az időbeli kontrasztot. Megmutattam, hogy a laboratóriumokban leggyakrabban elérhető autokorrelátorral a kontraszt nem becsülhető meg. Azok a mérések, amelyeket a RAL (Rutherford Appleton Laboratory) Ti:Saph lézerein zajlottak jó egyezést mutattak a mért és a számolt adatok között, ahol az időbeli alakot a spektrumból becsültem.

REFERENCES

- I.1. R.L. Sheffield et al. *Science* 274, 236 (1996)
- I.2. L.E.Hargrove, R.L.Fork, M.A.Pollock *Appl. Phys. Lett.* Vol.5. p.4 (1964)
- I.3. R.W.Hellwarth Adv. In Quant. Elec. (Columbia University Press, New York) p.34 (1961)
- I.4. J.C. Walling, H.P.Jenssen, R.C.Morris, E.W. O'Dell, O.G.Peterson *Opt. Lett.* Vol.4. p.182 (1979)
- I.5. P.F.Moulton *J.Opt.Soc.Am.B* Vol.3 p.125 (1986)
- I.6. J.A.Valdamis, R.L.Fork, J.P. *Opt. Lett.* Vol 10. p. 131 (1985)
- I.7. D. Strickland, G. Mourou *Opt. Commun.* Vol 56, p. 219 (1985)
- I.8. J.D.Kafka, M.L.Watts, J.J.Pieterse *IEEE J.Quant. Electr.*, Vol.28. No. 10, p 2151 (1992)
- I.9. D.E. Spence, P.N.Kean, W.Sibbett ,60-fsec pulse generation from self-mode-locked Ti:sapphire laser' *Opt.Lett.* Vol.16 p.42 (1991)
- I.10. D.E. Spence, J.M.Evans, W.E.Sleat, W, Sibbett 'Regeneratively initiated self-mode-locked Ti:sapphire laser' *Opt. Lett.* Vol.16. p. 1762 (1991)
- I.11. I.D.Jung,F.X. Kartner, N.Matuschek, D.H.Sutter, F.MorierGenoud, G.Zhang, U.Keller., V.Scheuer, M.Tilsch, T.Tschudi *Opt. Lett.* Vol. 22. p.1009 (1997)
- I.12. A. Baltuska, Z.Wie, M.S.Pshenichnikov, D.A. Wiersma, R. *Appl. Phys. B* Vol.65. p. 175. (1997)
- I.13. M. Nisoli, S.Stagira, S.De Silvestri, O. Svetlo, S.Sartania, Z.Cheng, M. Lenzner, C. Spielmann, F.Krausz *Appl.Phys.B* Vol. 65. p. 189. (1997)
- I.14. D. Strickland, G. Mourou, *Opt. Commun.* Vol 56, p. 219 (1985)
- I.15. D.Strickland, P.Bado, M.Pessot, G.Mourou, *IEEE J. Quant. Electr.* Vol. 24, p. 398 (1988)
- I.16. F. Krausz, M. Ivanov *Rev. Mod. Phys.* 81(1), 163-234
- I.17. M. Goeppert-Mayer *Ann. Physik* 9, 273 (1931)
- I.18. W. Kaiser, C.G.B. Garrett *Phys. Rev. Lett.* 7 (6), 229, (1961)
- I.19. P.Simon, H.Gerhardt, S. Szatmári, *Opt. Lett.* 14 (21),1207, (1989)
- I.20. I.N.Ross, W.T.Toner, C.J.Hooker, J.M.R. Barr, I Coffey *J. Mod. Opt.* 37 (4) 555 (1990)
- I.21. O. Kittelmann, J. Ringling *Opt. Lett.* 19 (24) 2053 (1994)
- I.22. V. Petrov, F. Rotermund, F. Noack, *Electron. Lett.* 34 1748 (1998)
- I.23. S. Wu, G. A. Blake, S. Sun, H.Yu, J. Ling *Opt. Comm.* 173, 371 (2000)
- I.24. K.J. Shaw et al. *J. Chem. Phys.* Vol.105, 1815 (1996)
- I.25. J. Hebling, J.Kuhl, *Opt. Lett*, Vol.14, 278 (1989)
- I.26. K.Osvay, G.Kurdi, J.Klebniczki, **M. Csatari**, I.N.Ross *Appl. Phys. Lett.* Vol. 80,1704 (2002)

- II.1. J. Liouville, *J. de Math.* Vol. 3, 349. (1838)
- II.2. F. Richard, J.R. Schneider, D. Trines, A. Wagner et al., TESLA Technical Design report, DESY- 2001-011, DESY, Hamburg (2001)
- II.3. S. Schreiber et al *Proc. of EPAC- 2002, Paris* (2002)

- II.4. J.S. Fraser et al. Proc. of Laser Acceleration of Particles AIP Malibu (1985)
- II.5. J. Smedley et al. Proc. PAC.03, Portland, May 2003.
- II.6. G. Suberlucq Proc. EPAC-2004, Lucerne, Switzerland (2004)
- II.7. Steven J. Russell 'Overview of High- Brightness, High- Average- Current Photoinjectors for FELs' talk (2002)
- II.8. O.Mete: EPFL PhD thesis 5020 (2011)
- II.9. W.E. Spicer, Phys. Rev. Vol.112,1,(1958)
- II.10. S.H. Kong et al. Nucl. Instr. and Meth. in Phys. Rev. A Vol. 358, 272-275 (1995)
- II.11. E. Chevallay, S. Hutchins, P.Legros, G. Suberlucq, H.Trautne CLIC Note 449, CERN/PS 2000-046
- II.12. R.W. Assmann, F. Becker, R. Bossart, H. Burkhardt, H. Braun, G. Carron, W. Coosemans, R. Corsini, E.T. D'Amico, J.-P. Delahaye, S. Doebert, S. Fartoukh, A. Ferrari, G. Geschonke, J.-C. Godot, L. Groening, G. Guignard (Editor), S. Hutchins, J.-B. Jeanneret, E. Jensen, J. Jowett, T. Kamitani, A. Millich, O. Napoly¹, P. Pearce, F. Perriollat, R. Pittin, J.-P. Potier, A. Riche, L. Rinolfi, T. Risselada, P. Royer, T. Raubenheimer², F. Ruggiero, R. Ruth², D. Schulte, G. Suberlucq, I. Syratchev, L. Thorndahl, H. Trautner, A. Verdier, I. Wilson, W. Wuensch, F. Zhou, F. Zimmermann, CERN-2000-008 (2000)
- II.13. S. Doebert et al., <http://project-clic-cdr.web.cern.ch/project-CLIC-CDR/>, Technical description of the accelerator components, Sources
- II.14. S. Hutchins, G. Suberlucq CTF3 Note 045 (Tech.) PS/PP/Note 2002-050 (2002)
- II.15. S. Hutchins CERN/PS CTF Note 96-14 (1996)
- II.16. C.P. Welsch, H.H. Braun, E. Bravin, R. Corsini, S. Döbert, T. Lefèvre, F.Tecker, P. Urschütz, B. Buonomo, O. Coiro, A. Ghigo, B. Preger, J. Instr. 1 P09002 (2006)
- II.17. Träger: Handbook of Lasers and Optics, Springer, Leipzig (2007)
- II.18. R. Paschotta: Filed Guide to Laser Pulse Generation, SPIE Press, USA (2008)
- II.19. A.E.Siegman: Lasers, University Science Books, Mill Valley, CA (1986)
- II.20. W. Koechner: Solid-State Laser Engineering, Springer-Verlag, Berlin Heidelberg (1999) Chapter 6.
- II.21. J.C. Diels, W. Rudolph: Ultrashort Laser Pulse Phenomena, Academic, San Diego (1996)
- II.22. A.Y. Cabezas, R.P. Treat J. Appl. Phys., Vol. 37, 3556 (1966)
- II.23. N.P.Barnes et al. IEEE JQE 26, 558 (1990)
- II.24. G. Mourou et al. Rev. Mod. Phys. Vol. 78, 2 p.310-370 (2006)
- II.25. D. Strickland, G. Mourou Opt. Comm. Vol. 56, 219 (1985)
- II.26. G. Cerullo, S. De Silvestri Rev. Sci. Instr. Vol. 74, 1, 1-18 (2003)
- II.27. A. Dubiets, R. Butkus, A.P. Piskarskas IEEE Sel. Top. Quant. Elec. Vol. 12, 2, 163-172 (2006)
- II.28. I. N. Ross CERN CLIC Note 462 (2000)
- II.29. R. Beach, P. Reichert, W. Benett, B. Freitas, S. Mitchell, A. Velsko, J. Davin, R. Solarz Opt. Lett.Vol. 18, 1326, (1993)

- II.30. S.Lee, S.K.Kim, M.Yun, H.S.Kim, B.H.Cha, H-J.Moon *App. Opt.* Vol. 41, 1089-1094, (2002)
- II.31. S.Konno, T.Kojima, S.Fujikawa, k.Yasui, *Opt. Lett.* 25, 105-107, (2000)
- II.32. Y.Hirano, T.Yanagisawa, S.Ueno, T.Tajime, O.Uchino, T.Nagai, C.Nagasawa *Opt. Lett.* 25, 1168-1170, (2000)
- II.33. K.Naito, M.Ohmi, K.Ishikawa, M.Akatsuka, M.Yamanaka, M.Nakatsuka, S.Nakai, *Appl. Phys. Lett.* 64, 1186-1188, (1994)
- II.34. D.R.Walker, C.J.Flood, H.M.van Driel, U.J.Greiner, H.H.Klingenberg, *Appl. Phys. Lett.* 65, 1992-1994, (1994)
- II.35. M.J.P.Dymott, K.J.Weingarten, *Appl. Opt.* 40, 3042-3045, (2001)
- II.36. I.Will, A.Liero, D.Mertins, W.Sandner *IEEE J.Q.E.* 34, 2020-2028, (1998)
- II.37. A.R.Fry, M.J.Fitch, A.C.Melissinos, B.D.Taylor, *Nucl. Instr. and Meth. in Phys. Res.* A430, 180-188, (1999)
- II.38. J. W. Bähr et al BIW10, TUPSM103 (2010)
- II.39. M. Krasilnikov et al., DESY-M-04-03U (2004)
- II.40. V. Le Flanchec, Bleses, S. Striby, *Appl. Opt.* Vol. 36, 33, 8541-8546 (1997)
- II.41. A.R. Fry et al *Proceedings of PAC 1997*, 4w022, Canada, (1997)
- II.42. M.Danailov et al. *Proceedings of the 2007 International FEL Conference*
- II.43. I. Will, G. Klemz *Opt. Exp.*; Vol. 16,19, 14922-14937 (2008)
- II.44. R. Scheps, *Introduction to Laser Diode-Pumped Solid State Lasers*, SPIE Press, USA (2002)
- II.45. J.E.Murray *IEEE J.Quant.Elec.* 19, 488-491, (1983)
- II.46. M. Doi, M. Sugiyama, K. Tanaka, M. Kawai, *IEEE J. Quant. Elec.*, Vol.12., 4. 745-750 (2006)
- II.47. J. D. Bull, N. A. F. Jaeger, H. Kato, M. Fairburn, A. Reid, and P. Ghanipour, *Proc. SPIE Photonics North 2004*, Vol. 5577 133–143 (2004)
- II.48. E. L. Wooten, K. M. Kissa, A. Yi-Yan, E. J. Murphy, D. A. Lafaw, P. F. Hallemeier, D. Maack, D. V. Attanasio, D. J. Fritz, G. J. McBrien, D. E. Bossi, *IEEE J. of Sel. Top. Quant. Elec.* Vol.6.,1. 69-82 (2000)
- II.49. F.J. Leonberger, *Opt. Lett.*, Vol.5., 7. 312-314 (1980)
- II.50. S. Zhang et al. *Proceedings of FEL 2006*, TUPPH061, BESSY, Berlin, Germany (2006)
- II.51. J. M. Byrd et al. *Proceedings of LINAC 2006*, THP007, Knoxville, Tennessee USA (2006)
- II.52. R. P. Scott, C. Langrock, and B. H. Kolner *Invited Paper. IEEE J. Sel. Topics in Quant. Electron.*, vol. 7, 4, pp. 641-655, (2001)
- II.53. D. Eliyahu, R; A. Salvatore, A. Yariv *J. Opt. Soc. Am. B* 13, 1619-1626 (1996)
- II.54. W. Koechner: *Solid-state Laser Engineering* 6th, rev. and updated ed., 2006, XVI, 748 p. 447 illus., Hardcover page 271-272
- II.55. R.L.Sutherland: *Handbook of nonlinear optics*, Marcel Dekker, 1996 Chapter 1
- II.56. https://www.as-photonics.com/snlo_files

- II.57. C.R.Guiliano, L.D.Hess Appl. Phys. Lett. 12 (9), 292 (1968)
- II.58. H.Cao, W.S. Warren J.Opt. Soc. Am. B 20 (3), 560 (2003)
- II.59. I. N. Ross, W. T. Toner, C. J. Hooker, J. R. M. Barr, I. Coffey, J. Mod. Opt., 37, 4, 555-573, (1990)
- II.60. A. Dubietis, G. Tamošauskas, A. Varanavičius, G. Valiulis, Appl. Opt. 39, 2437-2440 (2000).
- II.61. A. Dragomir, J. G. McInerney, D.N. Nikogosyan, Appl. Opt. 41, 4365-4376 (2002)
- II.62. R. DeSalvo, A. A. Said, D. J. Hagan, E. W. Van Stryland, M Sheik-Bahae, IEEE J. Quant. Electr. 32, 1324-1332 (1996)
- II.63. J. Reintjes, R.C. Eckardt, IEEE J. Quant. Electr. 13, 791-795 (1977)
- II.64. G. G. Gurzadyan, R. K. Ispiryan Appl. Phys. Lett. 59, 630-631 (1991)
- II.65. P. Liu, W. L. Smith, H. Lotem, J. H. Bechtel, N. Bloembergen, R. S. Adhav Phys. Rev. B. 17, 4620-4632 (1978)
- II.66. P. Kerkoc, S. Horinouchi, K. Sasaki, Y. Nagae, and D. Pugh, J. Opt. Soc. Am. B, 16, 1686-1691 (1999)
- II.67. S.Wu, Opt. Comm, Vol.173 , 371-376 (2000)
- II.68. Y.K.Yap Opt. Lett., Vol. 23. No. 13., p.1016 1998
- II.69. Auerbach UCRL-LR-105821-96-4 from Los Alamos, internal report p199.
- II.70. S.Seidel, G.Mann, SPIE, Vol. 2989 p.204
- II.71. L. Veisz InTech Chapter 14 305-330 (2010)
- II.72. K. L. Sala, G.A. Kenney-Wallace, G.E. Hall IEEE J. Quant. Elec. Vol. 16, 9, (1980)
- II.73. R.Trebino Frequency-Resolved Optical Gating: The measurement of Ultrashort Laser Pulses, Kluwer Academic Publishers, (2002)
- II.74. J.Collier et. al. STFC CLF Annual Report p 194-195 (1998/1999)
- II.75. M. Hentschel, S. Uemura, Z. Cheng, S. Sartania, G. Tempea, C. Spielmann and F. Krausz Applied Physics B: Lasers and Optics Vol. 68, 1, 145-148 (1999)
- II.76. T. Hirayama and M. Sheik-Bahae Opt. Lett., 27, 860 (2002)
- II.77. D.Kane, R. Trebino IEEE J. Quant. Elec. Vol 29. 2, 571 (1993)
- II.78. C. Iaconis, I.A. Walmsley Opt. Lett. Vol. 23. 10, 792 (1998)
- II.79. S.Basu et al. SPIE, Vol 2, 2989 (1997)
- II.80. E.Divall, I.Ross Opt. Lett. Vol. 29 (19) 2273-2275 (2004)
- II.81. M. D`Arco, **M. Csatari**, S. Gim, A. Masi. TBP as CERN technical note
- II.82. D.F.Hotz Appl. Opt., Vol. 4 (5), pp. 527-530 (1965)
- II.83. K.Varjú, A.P.Kovács,K.Osvay, G.Kurdi Opt.Lett., (2002) Vol. 27 2034-2036, (2002)
- II.84. K.Osvay, A.P.Kovács, Z.Heiner, G.Kurdi, J.Klebniczki, **M.Csatári** IEEE J.Sel.Top.Quant.Electr. 10 213-220 (2004)
- II.85. K.Osvay, A.P.Kovács, G.Kurdi, Z.Heiner, **M.Divall**, J.Klebniczki, I.E.Ferincz Opt.Comm. 248 201-209 (2005)
- II.86. A.P.Kovács, K.Osvay, G.Kurdi, M.Görbe,J.Klebniczki, Zs.Bor Appl.Phys.B 80 165-170 (2005)

- II.87. K.Osvay, **M.Csatári**, I.N.Ross, A.Persson, C.G.Wahlström Laser and Particle Beams 23 (2005)
- III.1. Y.Tang, **M. Divall**, I.N.Ross, E. Springate, G.J. Hirst, S. Hancock et al., CLF Annual Report 2004-2005, 248-250 (2005)
- III.2. I.N.Ross, E.J.Divall, J.M.D.Lister, *CLF Ann. Rep.*, RAL, TR-96-066, 101-103, (1996)
- III.3. **M.Csatari**, I.N.Ross CLF Ann Rep. 2002-2003 RAL, 196-197 (2003)
- III.4. I. N. Ross, **M. Csatári**, S. Hutchins, *Appl. Opt.*, Vol. 42 (6), 1040-1047 (2003)
- III.5. **M.Divall**, G.J.Hirst, I.N.Ross, H.Braun, R.Losito, L.Rinolfi, G.Suberlucq, CARE-Report-05026-PHIN (2005)
- III.6. M. Petrarca, M. Martyanov, **M. C. Divall**, G. Luchinin, J. Quant. Elec., Vol 47 (3) 306-313 (2011)
- III.7. **M. Divall** et al., CARE-Report-05026-PHIN (2005).
- III.8. I. N. Ross and **M.Csatari**, CLF Annual Report 2001/2002 202-205 (2002).
- III.9. G. Kurdi, I. O. Musgrave, **M. Divall**, E. Springate, W. Martin, G. J. Hirst, and I. N. Ross, STFC CLF Ann. Rep., 225-228 (2006/2007)
- III.10. **M.'Csatari' Divall**, A. Andersson, B. Bolzon, E. Bravin, E. Chevallay, S. Döbert, A. Drozdy, V. Fedosseev, C. Hessler, T. Lefevre, S. Livesley, R. Losito, Ö. Mete, M. Petrarca, A.N. Rabiller *Nucl. Instr. and Meth. in Physics Research Section A* Vol. 659, 1, p. 1-8 (2011)
- III.11. M. Petrarca, E. Chevallay, S. Doebert, A. Dabrowski, **M. Divall**, V. Fedosseev, N. Lebas, T. Lefevre, R. Losito, D. Egger, O. Mete, Proc. IPAC 2010, THPEC032 4122-4124 (2010)
- III.12. W. Farabolini, D. Bogard, A. Curtoni, P. Girardot, F. Peauger, C.S. Simon, E. Chevallay, **M. Divall Csatari**, N. Lebas, M. Petrarca, A. Palaia, R.J.M.Y. Ruber, V.G. Ziemann IPAC 2011 MOP001 (2011)
- III.13. S. Szatmári *Appl. Phys. B* 58, 211-219 (1994).
- III.14. **M. Divall**, K. Osvay, G. Kurdi, E.J. Divall, J. Klebniczki, J. Bohus, Á. Péter and K. Polgár *Appl. Phys. B: Lasers and Optics* Vol. 81, 8 (2005)
- III.15. **M.Csatári**, K.Osvay, J.Klebniczki, G.Kurdi, E.J.Divall, J.Bohus, Á.Péter 28th ECLIM, Rome, Italy, 2004, paper Mo/P/21
- III.16. **M. Csatári**, K. Osvay, J. Klebniczki, G. Kurdi, E.J. Divall FemtoMat 2002, Visegrád, Hungary, 2002
- III.17. Ö. Mete, E. Chevallay, A. Dabrowski, **M. Divall**, S. Döbert, D. Egger, K.Elsener, V. Fedosseev, T. Lefèvre, M. Petrarca, CLIC-Note-809, (2010)
- III.18. K.Osvay, **M.Csatári**, A.Gaál, I.N.Ross *J.Chin.Chem.Soc.* 47 855-857 (2000)
- III.19. **Csatári M.**, Osvay K. *Kvantumelektronika* 2000, Budapest, paper P6 (2000)
- III.20. K.Osvay, **M.Csatári**, I.N.Ross, A.Persson, C.-G.Wahlström On the temporal contrast of high intensity fs laser pulses 28th ECLIM, Rome, Italy, paper We/O2/4/O (2004)

III.21. K. Osvay, **M. Csatári**, I.N. Ross, A. Persson, C.-G. 2nd FemtoMat Conference, Bad Kleinkirchheim, Austria, paper We 2. (2004)

Acknowledgement

I would like to say thanks to all the people who have helped me along the way to produce this thesis. First of all to Dr. Hilbert Margit, who has allowed a bunch of secondary school students to come to Szeged University and made it possible for us to get our hands on equipment, which was not available at school. From then on there was no escape. She has also introduced me to my first laser experiment and supervised me for my diploma. Dr. Szabó Gábor professor introduced me to Dr. Károly Osvay, my PhD supervisor, who has quickly got me involved with the activities of the TeWaTi lab developed at the time. I also had the opportunity to use one of professor Szatmári Károly's Kr:F lasers. Thanks for all of them for teaching me how to approach research.

Through Károly's long lived contacts with Rutherford Appleton Laboratory in the UK, I could go there as a visiting scientist and had the fantastic opportunity to work there with Dr. Ian Ross. He has ever since been an example for me and cannot express how much I have learnt from him both on the scientific and on the personal side of my life. He truly could calculate on a back on an envelope and would get to the same result as me after a few pages.

Thanks to Roberto Losito and Dr. Valentin Fedosseev for giving me this opportunity to come to CERN to work on the Photo-injector at an exciting time, when the LHC first circulated its beam around the ring. Thanks Dr. Steffen Döbert, who tirelessly has answered my questions about the electron beam side of the injector and almost killed me by taking me along to one of his „casual“ jogs.

I thank my current supervisor, Dr. Christoph Hauri, who has allowed me to work part time to finish this work and brought me back to the world of Ti:Sapphire lasers.

I also thank all my close colleagues, who worked with me long hours in the lab and all the technicians, who have kept the machine working.

Lot of memories to treasure.

I would also like to thank my family, my children and husband, who have been so patient while „Mummy was writing a book“, „Mummy was making light“, „Mummy was going to school“. Without their help and support none of this would have been possible.